

2012

Experimental investigations in CO₂ sequestration and shale caprock integrity

Abiola Olukola Olabode

Louisiana State University and Agricultural and Mechanical College, olabode51@yahoo.com

Follow this and additional works at: https://digitalcommons.lsu.edu/gradschool_theses



Part of the [Petroleum Engineering Commons](#)

Recommended Citation

Olabode, Abiola Olukola, "Experimental investigations in CO₂ sequestration and shale caprock integrity" (2012). *LSU Master's Theses*. 2808.

https://digitalcommons.lsu.edu/gradschool_theses/2808

This Thesis is brought to you for free and open access by the Graduate School at LSU Digital Commons. It has been accepted for inclusion in LSU Master's Theses by an authorized graduate school editor of LSU Digital Commons. For more information, please contact gradetd@lsu.edu.

EXPERIMENTAL INVESTIGATIONS IN CO₂ SEQUESTRATION AND
SHALE CAPROCK INTEGRITY

A Thesis

Submitted to the Graduate Faculty of the
Louisiana State University and
Agricultural and Mechanical College
in partial fulfillment of the
requirements for the degree of
Master of Science in
Petroleum Engineering

in

The Craft and Hawkins Department of Petroleum Engineering

by

Abiola Olabode

B.Sc., Obafemi Awolowo University, Nigeria, 2008

December 2012

ACKNOWLEDGEMENTS

My sincere gratitude goes to the following; my advisor, Dr. Mileva Radonjic for the opportunity to work under her and for providing me with guidance and the resources that made this project a success; my committee members, Dr. Christopher White and Dr. Richard Hughes for their invaluable contributions and criticisms that have given shape to this work.

I want to thank the Craft and Hawkins department, the Chair and Faculty of Petroleum Engineering as well as the Society of Petroleum Engineers (SPE) for giving me the opportunity and financial aid to undertake my graduate studies. I thankfully acknowledge the useful contacts of Pamela Tomski of Research Experience in Carbon Sequestration, Andreas Busch of Shell and Dr. Peter Walsh of the University of Alabama at Birmingham. Many thanks to Dr. Jack Pashin of Alabama Geological Survey for providing the core samples of shale rock that were used in my experiments. I appreciate Wanda LeBlac, Syam Dodla, Donmei Cao and Rui Li for assisting with post experimental analysis. I also thank George Ohrberg for helping with computing needs in data acquisition and Fenelon Nunes for helping with laboratory ware purchases and maintenance. I am grateful to Dr. Kerry Dooley of the Chemical Engineering department, LSU for graciously allowing the use of his laboratory for the BET measurements.

I am appreciative of my friends and colleagues with whom I shared and gained useful ideas. They include Nnamdi Agbasimalo, Chukwudi Chukwudozie, Wei Wang, Gbolahan Afonja, Louise Smith and Paulina Mwangi.

Finally, I am immensely grateful to my biological father, Omoefe Kio and siblings for the love and moral support they have given to me throughout my academic sojourn.

TABLE OF CONTENTS

ACKNOWLEDGEMENTS.....	ii
LIST OF TABLES	v
LIST OF FIGURES	vii
NOMENCLATURE	xiii
ABSTRACT	xiv
CHAPTER 1. INTRODUCTION.....	1
1.1 Background of CO ₂ Sequestration	1
1.2 Objective	6
1.3 Methodology	7
CHAPTER 2. LITERATURE REVIEW	8
2.1 Shale Caprock in CO ₂ Sequestration	8
2.2 Geochemistry of Shale Caprock	11
2.3 Geomechanics of Shale Caprock.....	14
2.4 Hydrodynamics.....	17
2.5 Coupled Processes in Shale Caprock-CO ₂ Interaction	18
2.6 Dimensionless Numbers in Reactive Flow	19
2.6.1 Peclet Number.....	20
2.6.2 Damkohler Number	20
2.6.3 Peclet-Damkohler Number	21
2.7 Important Properties of Shale in CO ₂ Sequestration	21
2.8 Justification of Research Direction	22
CHAPTER 3. EXPERIMENTAL SETUP AND PROCEDURE.....	24
3.1 Experimental Methods and Sample Preparation	24
3.2 Experimental Setup.....	24
3.2.1 Pressure Cells	25
3.2.2 Syringe Pump.....	28
3.2.3 Data Acquisition System	28
3.2.4 Back Pressure Regulator (BPR).....	28
3.3 Experimental Process Parameters	29
3.4 Experimental Shale Caprock Geology	29
3.5 Experimental CO ₂ -brine Fluid	31
3.6 Techniques in Rock and Fluid Analysis	32
3.6.1 Inductively Coupled Plasma-Optical Emission Spectroscopy (ICP-OES)	32
3.6.2 X-Ray Diffraction (XRD) Analysis.....	33
3.6.3 Energy Dispersive Spectroscopy (EDS)	33
3.6.4 Optical and Scanning Electron Microscopy (SEM) Imaging	34
3.6.5 Brunauer, Emmet and Teller (BET) Technique	34

CHAPTER 4. RESULTS AND DISCUSSION.....	39
4.1 Selection of Shale Caprock Samples and Back Pressure Magnitude	39
4.2 Geochemical Analysis of Fluid and Rock	40
4.2.1 pH Profile	40
4.2.2 Inductively Coupled Plasma Optical Emission Spectrometry (ICP-OES)	42
4.2.3 XRD Analysis	43
4.3 Scanning Electron Microscopy (SEM) and Energy Dispersive Spectroscopy (EDS)	47
4.4 BET Nitrogen Adsorption Analysis	52
4.4.1 Pore Geometrical Properties in Bulk Shale Caprock	52
4.4.2 Pore Size Distribution	58
4.5 Permeability Implication	76
4.6 Dimensionless Numbers	79
4.6.1 Peclet Number	79
4.6.2 Peclet-Damkohler Number	79
4.7 General Discussion of Results	81
 CHAPTER 5. CONCLUSIONS AND RECOMMENDATIONS87
5.1 Conclusions87
5.2 Recommendations	88
 REFERENCES	 89
 APPENDIX	 96
A EXPERIMENTAL SETUP AND SAMPLE PREPARATION	96
 B COLLECTION OF POST-EXPERIMENTAL EFFLUENT AND SELECTION OF CO ₂ - BRINE REACTED SHALE ROCK FOR ANALYSIS.....	 104
 C pH DATASHEET	 106
 D ICP-OES DATASHEET	 107
 E SCANNING ELECTRON MICROSCOPY IMAGE OF SHALE CAPROCK SAMPLE....	 108
 F BET NITROGEN ADSORPTION DATASHEET	 110
 G CALCULATION OF PERMEABILITY RATIO AND DIMENSIONLESS NUMBERS...	 134
 VITA	 136

LIST OF TABLES

1.1: Worldwide potential CO ₂ sequestration capacities and risks	1
2.1: Typical mineralogy of shale samples as reported by Al-Bazali et al., 2005	9
2.2: Ductility ranking of different caprock lithologies	14
3.1: Experimental brine composition for Shale/CO ₂ -brine flooding experiment	32
4.1: Experimental shale caprock mineralogy in weight percents of its major components.....	39
4.2: Percentage (%) change in the mineralogical composition of Sample A after months of CO ₂ -flooding.....	44
4.3: Percentage (%) change in the mineralogical composition of Sample B after months of CO ₂ -flooding.....	44
4.4: Percentage (%) change in the mineralogical composition of Sample C after months of CO ₂ -flooding.....	44
A.1: Measured capillary entry pressure of Pierre, C1 and Arco-China shales using Oil-Based Mud, Decane, Crude Oil and Nitrogen Gas as reported by Al-Bazali et al., 2005.....	101
A.2: Estimated nano-porous shale capillary data using available values of IFT and contact angle for shale/CO ₂ -brine interaction reported by Daniel and Kaldi, 2009.....	102
C.1: pH datasheet (A)	106
C.2: pH datasheet (B)	106
C.3: pH datasheet (C)	106
D: ICP-OES datasheet for cations present in effluent solution	107
F.1: BET desorption pore size distribution for control specimen of sample A	111
F.2: BET desorption pore size distribution for 1 month CO ₂ -brine flooded specimen of sample A	113
F.3: BET desorption pore size distribution for 2 month CO ₂ -brine flooded specimen of sample A	115
F.4: BET desorption pore size distribution for 3 month CO ₂ -brine flooded specimen of sample A	117

F.5: BET desorption pore size distribution for control specimen of sample B	119
F.6: BET desorption pore size distribution for 1 month CO ₂ -brine flooded specimen of sample B	121
F.7: BET desorption pore size distribution for 2 month CO ₂ -brine flooded specimen of sample B	123
F.8: BET desorption pore size distribution for 3-month CO ₂ -brine flooded specimen of sample B	125
F.9: BET desorption pore size distribution for control specimen of sample C	127
F.10: BET desorption pore size distribution for 1-month CO ₂ -brine flooded specimen of sample C	129
F.11: BET desorption pore size distribution for 2-month CO ₂ -brine flooded specimen of sample C	131
F.12: BET desorption pore size distribution for 3-month CO ₂ -brine flooded specimen of sample C	133
G.1: Calculations of permeability ratio for shale caprock samples over 3 months of CO ₂ -brine flooding	134
G.2: Calculation of Peclet (Pe) and Peclet-Damkohler (PeDa) Numbers	135

LIST OF FIGURES

1.1: CO ₂ emission sources, potential utilization and sequestration sites (Courtesy of the Department of Energy).....	2
1.2: United States electric power generation by fuel over the next 25 years (Courtesy of the Department of Energy)	3
1.3: Schematic of CO ₂ diffusive loss and other leakages through shale caprock	6
2.1: Diagrammatic illustration of the effect of the largest pore throat size on sealing capacity of caprocks	10
2.4: Coupled processes in caprock-CO ₂ interaction showing critical parameters	18
2.5: Geochemical counterbalancing of geomechanical processes within shale caprock (Adapted from Johnson et al., 2005)	19
3.1: Schematics showing CO ₂ -brine flooding of comminuted shale caprock	25
3.2: Schematic of CO ₂ -brine streamline through the shale caprock packed into the experimental flow cell. The sketch shows that the crushed shale samples are adequately contacted by the injected fluid which penetrated deep into all the pore spaces of the rock.....	26
3.3: Schematics of experimental setup in shale-CO ₂ brine flooding	27
3.3: Stratigraphic profile of the Pottsville Formation showing shale sample location (Courtesy of the Department of Energy)	30
3.4: Physical shale caprock cores from the Pottsville Formation, Alabama	31
4.1: Ternary plot of shale caprock mineralogy showing the content of experimental cells	39
4.2: pH evolution chart for shale/CO ₂ -brine flooding effluents over the 3 months experimental period. Three distinct regions of pH change indicate the geochemical buffer strength of the shale caprock under continuous contact mode	41
4.3: ICP-OES cation identification in effluent collected from shale/CO ₂ -brine flooding over the 3 months experimental period. It showed Ca ²⁺ as having the highest part per million concentration out of the five alkaline earth metals analyzed in the effluent. The lower 5ppm portion of the graph is inserted to show the concentrations of Fe ²⁺ , Mn ²⁺ , Al ³⁺ and Si ²⁺	43
4.4: X-ray diffractograph for bulk mineralogical analysis of CO ₂ -brine contacted shale (sample A) before and after the three months experiment. It showed less noise in the CO ₂ -brine contacted sample indicating reduced amorphous content	45

4.5: X-ray diffractograph for bulk mineralogical analysis of CO ₂ -brine contacted shale (sample B) before and after the three months experiment. It showed less noise in the CO ₂ -brine contacted sample indicating reduced amorphous content	46
4.6: X-ray diffractograph for bulk mineralogical analysis of CO ₂ -brine contacted shale (sample C) before and after the three months experiment. It showed less noise in the CO ₂ -brine contacted sample indicating reduced amorphous content	46
4.7: X-ray diffractograph for bulk mineralogical analysis of precipitates obtained from CO ₂ -brine contacted shale samples' effluent after the three month experiment. It showed high pitch noise indication large amorphous content in the precipitates	47
4.8: 5µm resolution SEM image of control sample for specimen A showing mineral grains sizes of platelet structure and sub-micron pores at the site around EDS multi-spot analysis.....	49
4.9: Average EDS plot of surface mineralogy of control sample for specimen A showing the relative elemental composition of multiple spots on the corresponding SEM image	49
4.10:5µm resolution SEM image for specimen A showing mineral grains sizes of platelet structure and sub-micron pores at the site around EDS multi-spot analysis after 3 months of CO ₂ -brine flooding	49
4.11: Average EDS plot of surface mineralogy for specimen A showing the relative elemental composition of multiple spots on the corresponding SEM image after 3 months of CO ₂ -brine flooding	49
4.12: 5µm resolution SEM image of control sample for specimen B showing mineral grains sizes of platelet structure and sub-micron pores at the site around EDS multi-spot analysis	50
4.13: Average EDS plot of surface mineralogy of control sample for specimen B showing the relative elemental composition of multiple spots on the corresponding SEM image	50
4.14: 5µm resolution SEM image for specimen B showing mineral grains sizes of platelet structure and sub-micron pores at the site around EDS multi-spot analysis after 3 months of CO ₂ -brine flooding	50
4.15: Average EDS plot of surface mineralogy for specimen B showing the relative elemental composition of multiple spots on the corresponding SEM image after 3 months of CO ₂ -brine flooding	50
4.16: 5µm resolution SEM image of control sample for specimen C showing mineral grains sizes of platelet structure and sub-micron pores at the site around EDS multi-spot analysis	51
4.17: Average EDS plot of surface mineralogy of control sample for specimen C showing the relative elemental composition of multiple spots on the corresponding SEM image	51

4.18: 5 μ m resolution SEM image for specimen C showing mineral grains sizes of platelet structure and sub-micron pores at the site around EDS multi-spot analysis after 3 months of CO₂-brine flooding 51

4.19: Average EDS plot of surface mineralogy for specimen C showing the relative elemental composition of multiple spots on the corresponding SEM image after 3 months of CO₂-brine flooding 51

4.20: 1 μ m resolution SEM image of the effluent precipitate with no crystalline micro-structure visible. The surface appears amorphous 52

4.21: Average EDS plot of surface elemental mineralogy of effluent precipitate showing high Fe, O and Si concentration after 3 months of CO₂-brine flooding 52

4.22: Bulk specific surface area of the shale caprock samples over 3 months of CO₂-brine flooding depicting an overall increase in measured surface area available for adsorption with the exception of sample C that initially decreased after the first month of flooding..... 54

4.23: Bulk specific pore volume of the shale caprock samples over the 3 months of CO₂-brine flooding depicting an overall increase in measured pore volume available for adsorption with the exception of sample C that initially decreased after the first month of flooding 55

4.24: Bulk average pore sizes of the shale caprock samples over the 3 months of CO₂-brine flooding. It shows haphazard changes that indicated sample B has the lowest average pore size magnitude in contrast to observed specific surface area and pore volume evolution trend 56

4.25: Bulk modal pore sizes for the shale caprock samples over the 3 months of CO₂-brine flooding. It shows haphazard changes that indicated sample B has the lowest modal pore size magnitude in contrast to observed specific surface area and pore volume evolution trend 57

4.26: Pore size distribution for sample A over the 3 month experimental period of shale caprock/CO₂-brine flooding. It shows four regions of changes in specific pore volume with only region 3 having a net decrease in pore volume by the end of the third month of experiment 59

4.27: Pore size distribution for sample B over the 3 month experimental period of shale caprock/CO₂-brine flooding. It shows four regions of changes in specific pore volume with only region 3 having a net decrease in pore volume by the end of the third month of experiment 60

4.28: Pore size distribution for sample A over the 3 month experimental period of shale caprock/CO₂-brine flooding. It shows four regions of changes in specific pore volume with no region having a net decrease in pore volume by the end of the third month of experiment61

4.29: Cumulative specific surface area for sample A with less than 5.5nm pores over the 3 months of CO₂-brine flooding. It shows that significant surface area changes occur in pore sizes that are less than 3.5nm with the surface area converging back to the control sample initial value 62

4.30: Cumulative specific surface area for sample B with less than 5.5nm pores over the 3 months of CO₂-brine flooding. It shows that significant surface area changes occur in pore sizes that are less than 3.5nm with net overall increase at the end of the third month 63

4.31: Cumulative specific surface area for sample C with less than 5.5nm pores over the 3 months of CO₂-brine flooding. It shows that significant surface area changes occur in pore sizes that are less than 3.5nm with net overall increase at the end of the third month 64

4.32: Cumulative specific pore volume for sample A with less than 5.5nm pores over the 3 months of CO₂-brine flooding. It shows that modest pore volume changes occur in pore sizes that are less than 3.5nm with net overall increase at the end of the third month 66

4.33: Cumulative pore volume for sample B with less than 5.5nm pores over the 3 months of CO₂-brine flooding. It shows that modest pore volume changes occur in pore sizes that are less than 3.5nm with net overall increase at the end of the third month 67

4.34: Cumulative pore volume for sample C with less than 5.5nm pores over the 3 months of CO₂-brine flooding. It shows that modest pore volume changes occur in pore sizes that are less than 3.5nm with net overall increase at the end of the third month 68

4.35: Cumulative specific surface area for sample A with greater than 5.5nm pores over the 3 months of CO₂-brine flooding. It shows a modest net increase in surface area at the end of the 3rd month 69

4.36: Cumulative specific surface area for sample B with greater than 5.5nm pores over the 3 months of CO₂-brine flooding. It shows a significant net increase in surface area at the end of the 3rd month 70

4.37: Cumulative specific surface area for sample B with greater than 5.5nm pores over the 3 months of CO₂-brine flooding. . It shows an insignificant net increase in surface area at the end of the 3rd month 72

4.38: Cumulative pore volume for sample A with greater than 5.5nm pores over the 3 months of CO₂-brine flooding. It shows a significant net increase in pore volume for pore sizes greater than 30nm 73

4.39: Cumulative pore volume for sample B with greater than 5.5nm pores over the 3 months of CO₂-brine flooding. . It shows a significant net increase in pore volume for pore sizes greater than 30nm 74

4.40: Cumulative pore volume for sample C with greater than 5.5nm pores over the 3 months of CO ₂ -brine flooding. It shows a significant net increase in pore volume for pore sizes greater than 30nm	75
4.41: Plot of permeability ratio of the shale caprock samples over the 3- month experimental period. Sample B consistently had the lowest ratio indicating a strong resistance to flow within connected rock matrix pores	78
4.42: Peclet Number variation over the 3-month experimental period. It indicates a uniform diffusion process into the shale caprocks with sample B having the lowest Peclet values	80
4.43: Peclet-Damkohler Number variation over the three month experimental period. The reactive components of PeDa indicate a direct relationship between geochemical interactions and pore size distribution	81
A.1: Physical arrangement of experimental apparatus in shale caprock/CO ₂ -brine flooding	96
A.2: Crushed shale caprock samples showing particle dimension	96
A.3: Crushed shale caprock sample packed into a pressure cell	96
A.4: Syringe pump used as backup pump in shale caprock/CO ₂ -brine flooding	97
A.5: Crushed shale caprock control sample re-saturation under vacuum condition	97
A.6: CO ₂ -brine preparation setup showing CO ₂ cylinder and mixing tank	97
A.7: Nitrogen cylinders used in operating back-pressure regulator	97
A.8: Back pressure regulator and piston pump connected during experiment	98
A.9: XRD instrument at LSU Geology department	98
A.10: BET instrument showing liquid nitrogen dewar and sample holder bulbs	98
A.11: CO ₂ -brine flooded crushed shale after three months	98
A.12: Pressure evolution plot as captured by National Instrument Labview data acquisition device showing the approximate capillary entry pressure for the shale caprock (sample A)	100
E.1: SEM image for sample A after 1 month of CO ₂ -brine flooding	107
E.2: SEM image for sample B after 1 month of CO ₂ -brine flooding	107
E.3: SEM image for sample C after 1 month of CO ₂ -brine flooding	107

E.4: SEM image for sample A after 2 month of CO ₂ -brine flooding	107
E.5: SEM image for sample B after 2 month of CO ₂ -brine flooding	108
E.6: SEM image for sample B after 2 month of CO ₂ -brine flooding	108
E.7: SEM image for sample C after 2 months of CO ₂ -brine flooding	108
E.8: Optical Microscopy image of thin section cut for control sample A showing pore networks	108

NOMENCLATURE

m = Molality; number of moles per 1 kg of aqueous solution

k = Permeability, D

ϕ = Porosity, %

P = Pressure, psi or MPa

T = Temperature, °C or °F

q = Flow rate, ml/min

D = Diffusion coefficient, m²/s

k_r = reaction rate, m/s

v = velocity, m/s

Pe = Peclet Number

Da = Damkohler Number

PeDa = Peclet-Damkohler Number

Å = Amstrong, 10⁻¹⁰m

BET = Brunauer-Emmett-Teller

ABSTRACT

More than sixty percent (60%) of conventional hydrocarbon reservoirs which are potential CO₂ repositories are sealed by tight shale caprock. The geochemical reactivity of shale caprock during CO₂ diffusive transport needs to be included in the reservoir characterization of potential CO₂ sequestration sites as slow reactive transport processes can either strengthen or degrade seal integrity over the long term. Several simulation results had predicted that influx-induced mineral dissolution/precipitation reactions within shale caprocks can continuously reduce micro-fracture networks, while pressure and effective-stress transformation first rapidly increase then progressively constrict them. This experimental work applied specific analytical techniques in investigating changes in surface/near-surface properties of crushed shale rocks after exposure (by flooding) to CO₂-brine for a time frame ranging between 30 days to 92 days at elevated pressure and fractional flow rate. Initial capillary entry parameters for the shale were estimated from digitally acquired pressure data evolution. Flooding of the shale samples with CO₂-brine was followed by geochemical characterization of the effluent fluid and bulk shale rock through ICP-OES, XRD, EDS and pH measurements. Nano-scale measurement of changes in internal specific surface area, pore volume and linear/cumulative pore size distribution (using the BET Technique) showed that changes in the shale caprock due to geochemical interaction with aqueous CO₂ can affect petrophysical properties. The intrinsically low permeability in shale may be altered by changes in surface properties as the effective permeability of any porous medium is largely a function of its global pore geometry. Diffusive transport of CO₂ as well as carbon accounting could be significantly affected over the long term. The estimation of dimensionless quantities such as Peclet (Pe) and Peclet-Damkohler (PeDa) Numbers that are associated with geochemical reactivity of rocks and acidic fluid transport through porous media gave insight into the impact of diffusion and reaction rate on shale caprock in CO₂ sequestration.

CHAPTER 1 INTRODUCTION

1.1 Background on CO₂ Sequestration

Sequestration of anthropogenic carbon dioxide (CO₂) into geologic subsurface sinks has gained much attention from the science and engineering community in recent years. As fossil fuel is expected to continue to play a significant role in meeting worldwide energy demand, environmental considerations require some form of mitigation for the CO₂ being emitted- a prominent greenhouse gas [1, 2].

Considerable amount of experimental and simulation studies in carbon dioxide sequestration have been carried out in investigating the geochemical and geomechanical stability of porous subsurface storage reservoirs such as saline aquifers, depleted oil and gas reservoirs, and coal bed seams for this purpose [3]. Table 1.1 below shows some estimates of the capacities available for each of these repositories worldwide.

Table 1.1: Worldwide potential CO₂ sequestration capacities and risks [4]

Storage option	Capacity (Gt-CO₂)	Storage integrity	Environmental risk
Depleted oil and gas reservoirs	25–30	High	Low
Unmineable coal seams	5–10	Average	Average
Deep saline aquifers	1–150	Average	Average
Ocean (global)	1000–10,000	Medium	High

More recently geothermal utilization of CO₂ is gaining attention in addition to its high potential for enhanced hydrocarbon recovery projects serving as both a sweeping and swelling fluid [5]. Saline aquifers are considered to be one of the best options for CO₂ sequestration due

to their large storage capacity, high injectivity and nearness to CO₂ sources [6]. Depleted oil and gas reservoirs, unmineable coal seams and ocean sinks are the other subsurface repositories that can be used for sequestering CO₂. Conventional sandstone reservoirs and possibly carbonates reservoirs are the most favored depleted oil and gas reservoirs considered in CO₂ sequestration. Experiments reacting supercritical CO₂ in synthetic and natural brines in the presence and absence of limestone and plagioclase-rich arkosic sandstone reveal that there are significant compositional, mineralogical and porosity changes in aquifer fluid and rock properties [7].

Figure 1.1 shows the network of potential sequestration sites and the CO₂ emitting industries that could be involved.

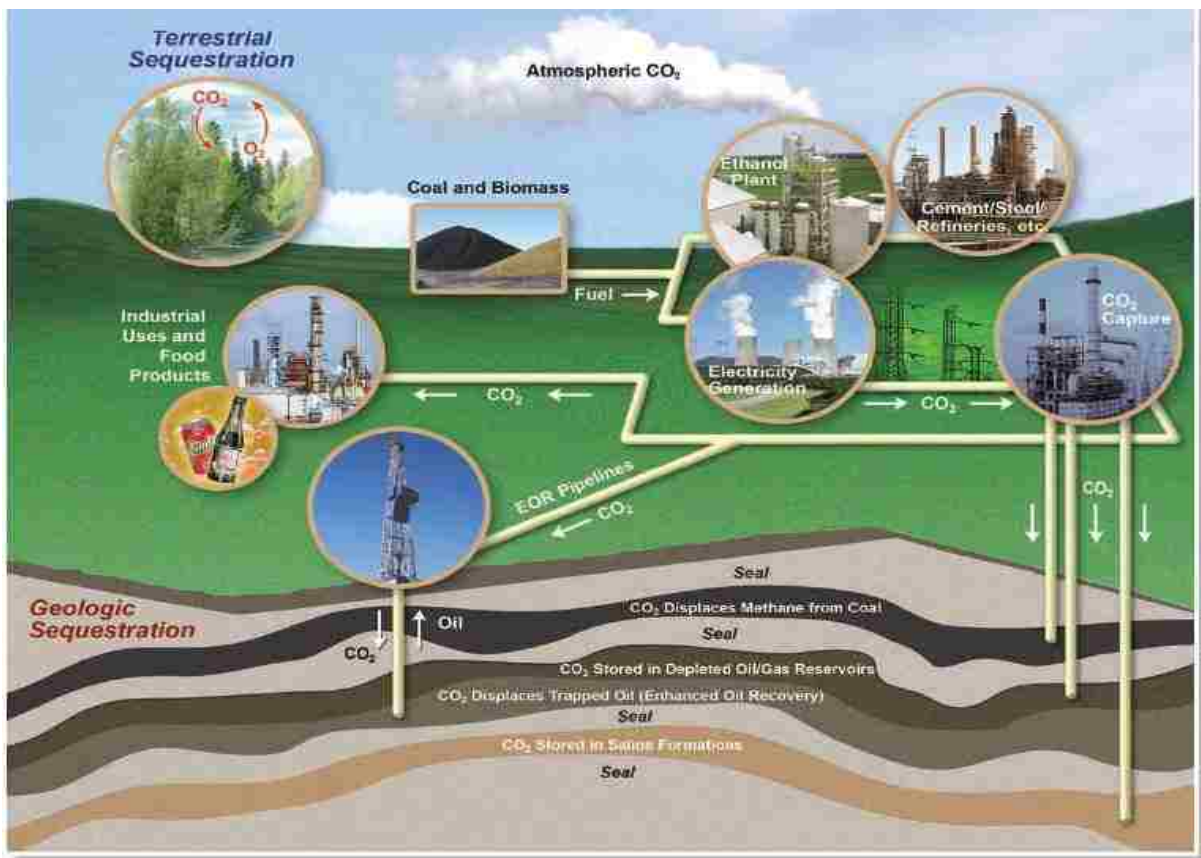


Figure 1.1: CO₂ emission sources, potential utilization and sequestration sites (Courtesy of the Department of Energy) [1]

Meanwhile the emission of anthropogenic CO₂ is expected to continue into the future at an increasing volumetric rate. Figure 1.2 depicts the trend in CO₂ emissions in the United States by fuel type over the next 25 years and beyond.

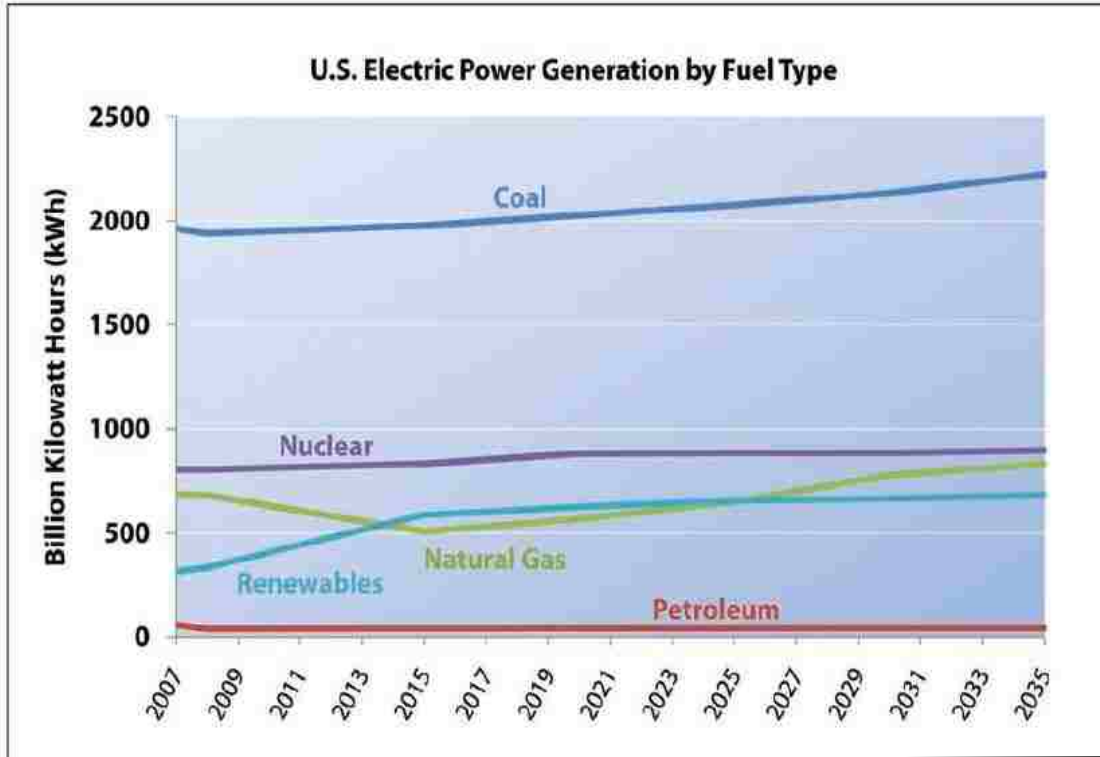


Figure 1.2: United States electric power generation by fuel over the next 25 years (Courtesy of the Department of Energy) [1]

Geological storage of CO₂ depends on the contribution of multiple CO₂ trapping mechanisms that includes: 1) physical trapping of CO₂ in a gaseous, liquid, or super critical state, 2) solubility trapping through dissolution of CO₂ within brine, 3) hydrodynamic trapping as a result of residual saturation of disconnected CO₂ within individual pore spaces and 4) mineral trappings- an insitu process of interstitial carbonate minerals formation from CO₂, the host rock and formation waters [8].

The process of carbon capture and sequestration include monitoring, verification, accounting and risk assessment of emission units and storage sites [1, 9]. At Sleipner in Norway,

seismic monitoring combined with seabed gravimetric technologies have been used to constrain reservoir simulation models and to acquire insight into the flow behavior of CO₂ plumes in the Utsira sandstone reservoir [10]. Extensive economic and cost analysis are required for projects that involve commercial entities and government appropriations [9].

Successful implementation of geological CO₂ sequestration depends on many factors including the ability to predict the extent of underground CO₂ movement and storage as a function of specific target formation that will enable the identification of optimal sites and evaluate their long term isolation performance [11] while asserting the results through experimentation. Geomechanical, geochemical and hydrological impact of engineered CO₂ storage into these geological storage options have been well researched with the conclusion that accurate estimation of maximum sustainable injection pressure plays a significant role on wellbore stability, wettability parameters, possible dormant fault reactivation among other concerns [12-15]. The presence of impurities in the CO₂ stream raises the question of possible underground water and aquatic life contamination. This requires factoring the effects of trace impurities from large emission sources into CO₂ transport, injection and storage modeling [16].

While appreciable efforts have been expended in the scientific evaluation of CO₂ storage feasibility in the above repositories, significant experimental research efforts are yet to be devoted to the seal rocks that cap most of these reservoirs. The reason might be their complexity, not just in terms of mineralogy and fluid flow behavior but also due to the lengthy laboratory measurements required for meaningful investigation [17]. The rock-fluid interaction processes that are observed in most conventional CO₂ repositories with high permeability and porosity are to a limited extent applicable to sedimentary caprocks [18]. Most effective caprock lithologies are fine-grained siliciclastics (clay-based rocks) and evaporites (anhydrites, gypsum, halites) [1,

19]. An effective caprock usually has capillary entry pressure that exceeds the upward buoyancy pressure exerted by an underlying hydrocarbon or CO₂ column. The capillary pressure of the caprock is largely a function of its pore sizes and this may be laterally variable. The buoyancy pressure is determined by the density of the reservoir fluid and column height. A caprock of extremely small pore size, in the order of nanometers, is required to prevent the buoyant rise of an underlying gas column [19].

Geochemistry and geomechanics affect caprock effectiveness and loss of gas through caprock may take place if the integrity of the caprock is breached, although transport processes are usually not rapid and may be in the nano-darcy permeability range. Recent field tests such as in Sleipner (Norway), showed that experience on in-situ caprock integrity characteristics can only be obtained in decades [17]. CO₂ plume development and the required geophysical monitoring methods (seismic, gravity, and satellite data) can only yield valuable geological information in years as evident from the 15 years of operating the Sleipner project [20]. Existing geologic discontinuities, fractures and faults also add to the uncertainty that may compromise seal effectiveness.

The quantitative assessment of leakage risks and leakage rates is a basic requirement for site approval, public acceptance and the awarding of potential credits for sequestered CO₂ quantities. Leakage through caprocks may occur in three different ways [17]:

- i.) rapid leakage by seal-breaching or wellbore failure (corrosion of pipes and cements), resulting in gas flow through a micro-fracture network.
- ii.) long-term leakage controlled by the capillary sealing efficiency and permeability (after capillary breakthrough pressure is exceeded).
- iii.) diffusive loss of dissolved gas through the water-saturated pore spaces.

Figure 1.3 depicts 1) Wellbore failure 2) Capillary breakthrough 3) Diffusive loss phenomena that can aid CO₂ leakage through the caprock.

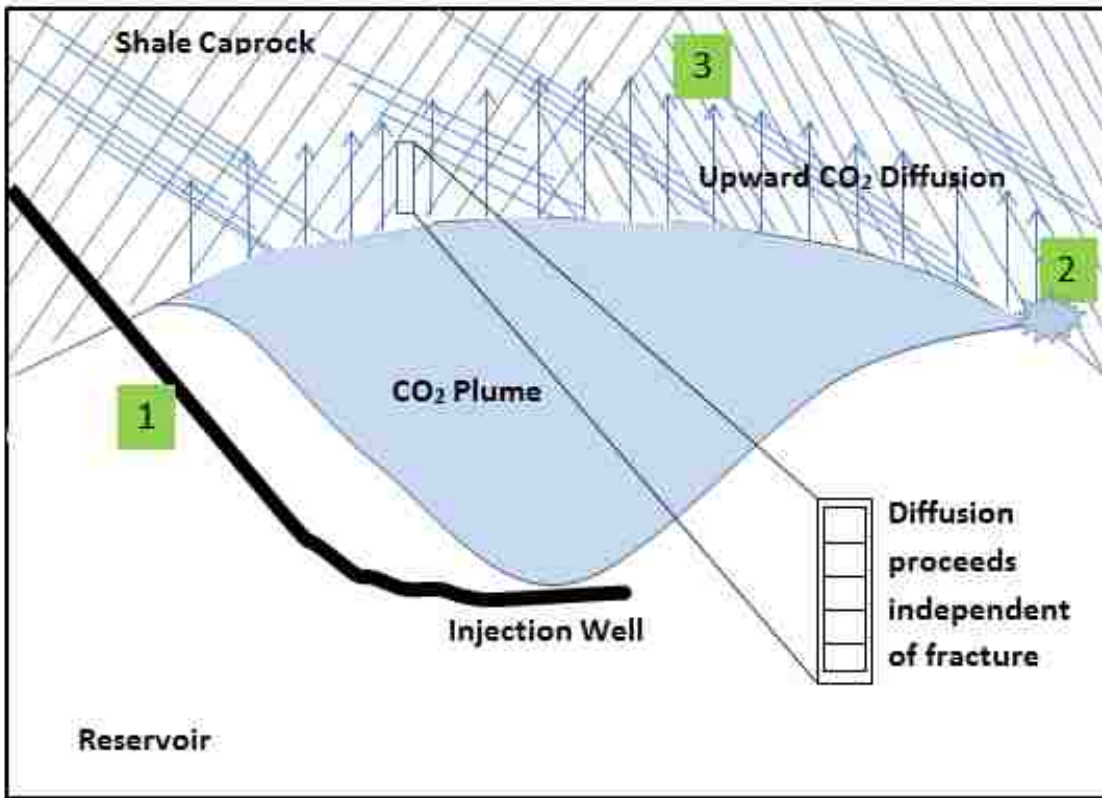


Figure 1.3: Schematic of CO₂ diffusive loss and other leakages through shale caprock [21]

1.2 Objective

This thesis research project is intended to achieve the following objectives:

1. Investigate experimentally the ex-situ relationship between geochemical and petrophysical changes in suitable shale caprock when contacted with CO₂-rich fluids continuously. Previous research has attempted to measure quantitatively the results of the geochemical changes that can significantly affect shale caprock's geomechanical, geochemical and hydrological stability by conducting batch rock-fluid interaction experiments [22-24].

2. Make engineering inferences from the application of analytical techniques to measuring geochemical and petrophysical parameters of the shale before and after the experiment.
3. Deduce meaningful conclusions from inferential data analysis about the integrity of shale caprock in CO₂ sequestration.

1.3 Methodology

To reach the stated objectives, flow-through experiments were conducted using three pressure cells and crushed shale samples prepared from 4-in cores of shale caprock from the Pottsville Formation of the Black Warrior Basin, Alabama. Carbon dioxide saturated brine was prepared by bubbling CO₂ through a brine reservoir at 25 psi over a period of 80 minutes. The experiment ran for 92 days and samples were taken out each month for analysis; both rock and effluent fluid. Quantitative and qualitative material characterization techniques were employed to have an understanding about the resultant effect of chemical reactions between the shale caprock and CO₂-brine system as well as changes in the petrophysical properties of the rock. Effluent brine samples were primarily analyzed to support findings from the petrophysical characterization techniques.

CHAPTER 2 LITERATURE REVIEW

2.1 Shale Caprock in CO₂ Sequestration

A regional caprock or topseal is one of the most critical features of subsurface geological repositories. The physical characteristics of caprocks determine the efficiency of subsurface trapping systems and migration paths. Continuity is important in regional caprocks as it determines whether a basin has laterally or vertically focused migration systems. Clay-rich caprocks such as shale should be investigated experimentally for their petrophysical and geochemical behavior when in contact with aqueous CO₂ over a long period of time. Shale caprock constitutes more than 60% of effective seals for geologic hydrocarbon bearing formations and are therefore of considerable interest in underground CO₂ storage into depleted oil and gas formations [19]. Experimental studies of wettability, contact angle and interfacial tension on shale using CO₂-rich fluid have not been widely reported [25]. Porosity, permeability, fractures and other petrophysical properties of the seal rock are of importance in seal integrity analysis and could be experimentally determined. Organic-rich shale is considered to have limited potential as membrane seals in CO₂ containment [25]. Previous experimental work on shale interaction with aqueous CO₂ made use of crushed fragments or pulverized samples- this is to provide large surface area for rock-fluid interaction [17]. Kaszuba *et al* and Kohler *et al* in separate studies concluded that the chemical reactivity of shale caprock needs to be included in reservoir characterization of potential CO₂ sequestration sites as slow reactive transport processes can impact seal integrity in the long term [22, 26].

Shale rocks are predominantly composed of clay. They might also have other silica and carbonate based minerals that contribute to their geomechanical strength [27]. Geochemical changes are dominated by rock-water interaction and mixing with reservoir fluids [19].

The mineralogical components of some shale samples are shown in table 2. It shows the predominant minerals of clay, quartz, feldspar and dolomite.

Table 2.1: Typical mineralogy of shale samples as reported by Al-Bazali et al., 2005 [28]

	Pierre Shale	Arco-China Shale	C1-Shale
X-Ray Diffraction	Weight, %	Weight, %	Weight, %
Quartz	19.0	51.0	14.0
Feldspar	4.0	12.0	2.0
Calcite	3.0	3.0	0.0
Dolomite	7.0	1.0	0.0
Pyrite	2.0	2.0	0.5
Siderite	1.0	0.0	0.0
*Total Clay	64.0	31.0	76.0
Chlorite	4.0	10.0	-----
Kaolinite	11.0	14.0	39.0
Illite	19.0	44.0	-----
Smectite	17.0	13.0	-----
Mixed Clay	49.0	20.0	-----

The rudimentary physical principles or forces governing the effectiveness of shale caprocks are the same as those controlling secondary migration. The major driving force is buoyancy caused by reservoir fluids which are mostly less dense than formation connate waters. The restricting force to the movement of subsurface fluid through caprocks is its capillary pressure which as mentioned earlier is dependent on the size of the pore throats. Due to subsurface density difference of fluids, shale caprock can support much larger liquid columns than gas columns, all other things being equal. Figure 2.1 shows the relationship between these two mechanisms with A and B having smaller pore throats than C, hence pore C has a much lower seal efficiency.

Depositional settings of transgressive marine shales on gently sloping siliciclastic shelves and evaporitic deposits on regressive supratidal sabkhas in interior basins can affect the lithology

of stratigraphic units that could ultimately determine petrophysical properties such as grain and pore sizes that characterizes tight rocks.

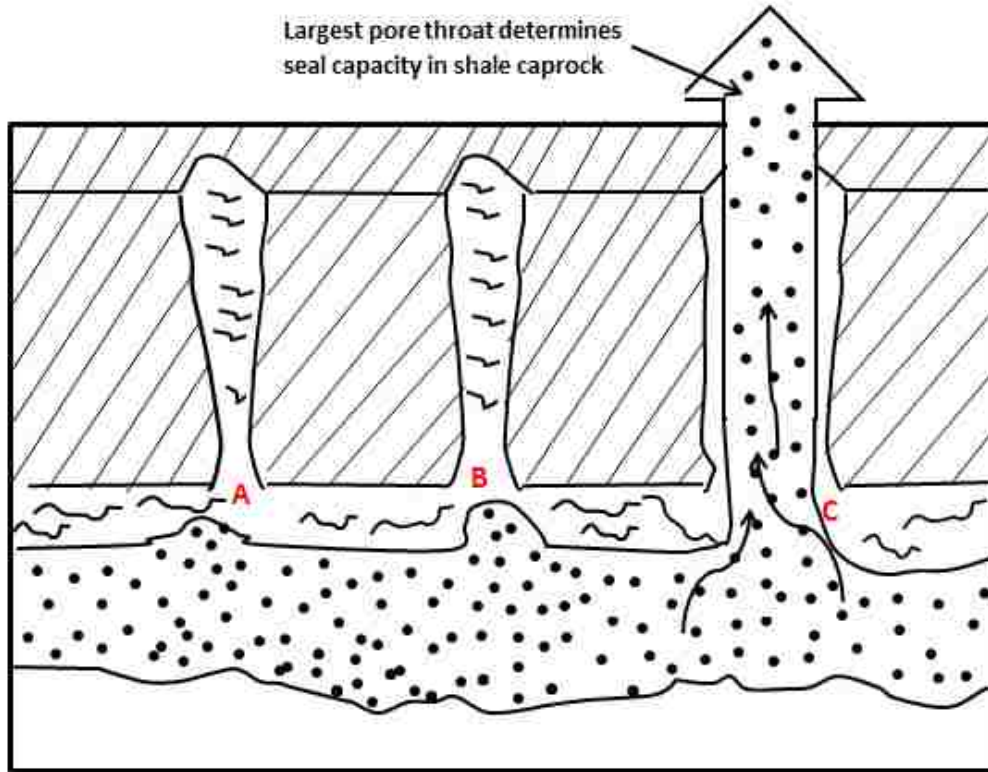


Figure 2.1: Diagrammatic illustration of the effect of the largest pore throat size on sealing capacity of caprocks [19]

However, under CO₂ sequestration conditions, the interaction between geochemical activity of the shale caprock and its geomechanics can result in distinct petrophysical properties. This can affect storage capacity and seal effectiveness. Several simulation results have predicted that influx-triggered mineral dissolution/precipitation reactions within typical shale cap rocks can continuously reduce microfracture apertures, while pressure and effective-stress evolution first rapidly increase then slowly constrict them [29-32]. The extent of geochemical alteration is considered to be nearly independent of the injection rate while that of geomechanical deformation is thought to be more pronounced during engineered storage [33]. There have been suggestions that ultimate restoration of pre-influx hydrodynamic seal integrity -in both EOR-

EGR/storage and natural accumulation settings- depends on ultimate geochemical counterbalancing of the resultant geomechanical effect [21, 22, 29, 33]. Natural helium has been suggested as a screening tool for assessing caprock imperfection but its large scale application has not been demonstrated [34]. Some of these imperfections can manifest as a variety of processes or features including but not limited to low hydraulic conductivity (permeability), preferential flow paths in the form of fractures and faults, isotopic compositional changes as well as the tendency for capillary breakthrough which may occur at localized spots within the caprock [34, 35]. Shale caprock ductility, thickness, lateral continuity and depth of burial play major roles in providing effective seals for subsurface fluids. The main geochemical, geomechanical and hydrological processes/features that can be observed in shale caprock are discussed further.

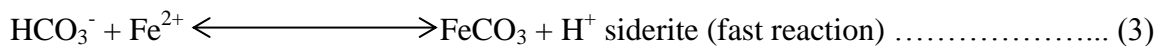
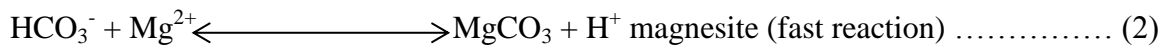
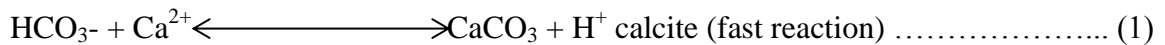
2.2 Geochemistry of Shale Caprock

The geochemical composition of shale caprock plays a significant role in its ability to perform effectively as a regional seal. The chemical reactivity of shale has been shown by several researchers to affect its petrophysical characteristics though the multiple reaction mechanisms and kinetic rates are not clearly defined and still needs to be investigated. Different mineral compositions ranging from quartz, calcite, anorthites, feldspar to muscovite, chlorite, illite, kaolinite and smectite have been reported for shale [36]. Mineral dissolution, re-precipitation and redistribution could affect transport properties of shale. Post experimental fluid analysis in a shale/water/CO₂ batch mixing experiment showed that the aqueous concentration of major elements such as Ca, Mg, Fe, Al and K increased and that the release rate of Fe and SiO₂ were more pronounced in solutions reacted with CO₂-brine when compared to reactions with CO₂-free brine [23]. The use of isotopic species have been suggested in tracing diagenetic

changes in shale caprock due to CO₂ sequestration [37]. But the cost implication of monitoring the isotope partition coefficients effectively as a control tool is yet to be determined.

The quality of shale caprock for the Krechba field in Algeria is reported to be controlled by the primary quantities of illite-muscovite and localized extent of chlorite-quartz cementation. This affirms the importance of mineralogy in seal effectiveness [38]. Diagenetic processes involving a host of sedimentary siliciclastic minerals can play significant role in enhancing or degrading caprock integrity over the long term. Temperature and pressure play an enormous extrinsic control on these subsurface processes. The following states the extent of geochemical reactivity that may be observed in shale/CO₂ interactive diagenesis [21] and the order in which they could occur, all other things being equal:

1. Carbonate reactions dominate in the short-term depending on material availability
2. Magnesite and siderite have fast reactions kinetics and rates depending on mineral concentration, pH, temperature and salinity as shown by equations (1), (2) and (3)



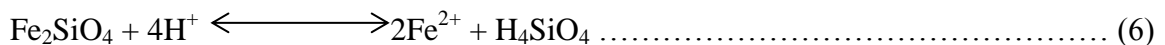
3. Feldspars, clays and other reactions follow and dominate over the long term as represented by equations (4) to (7)



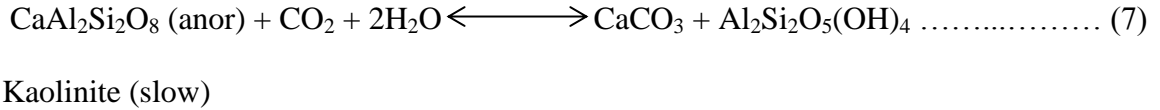
Wollastonite (slow) (neutralizes acidity)



Forsterite (slow) (neutralizes acidity)

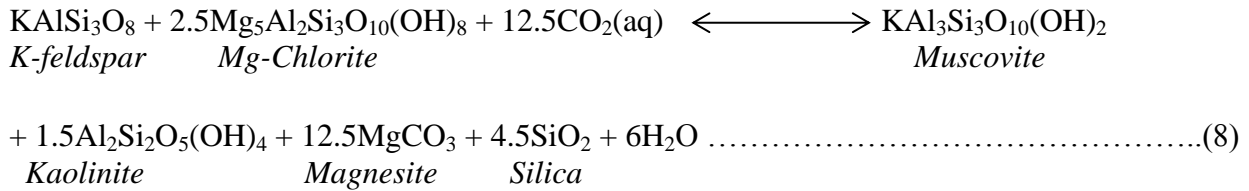


Fayalite (slow) (neutralizes acidity)



4. Concentration of pore-water due to CO₂ dissolution will change reactivity with time.
5. Desiccation of clay minerals may occur, causing caprock degradation through cracking.
6. The extent of alterations in caprock will depend on competing diffusion, advection and reaction rates.

A predicted overall reaction of interest in possible coupled chemo-geomechanical models is given below; the potential conversion of clay to other minerals [29]:



The chemical transformation of iron-bearing minerals to form iron carbonates could impact the geochemistry of carbon sequestration and the presence of carbonate adsorbates does not impede the reduction of ferric iron to ferrous forming siderite [39, 40]. Through leaching, the chemical constituent of shale can cause a slight increase in porosity that may be available for sequestering CO₂.

This has been demonstrated by modeling studies using TOUGHREACT and studies involving experimental models of cement-shale caprock interface fluid flow phenomenon [41, 42]. The possibility of this type of transformation was also observed during the course of this research project.


The clay content of shale typically defines its characteristic physical appearance and behavior- plasticity, hydration, anisotropy, layering and acoustic properties [43, 44]. The

presence of organic matter in shale caprock can significantly affect its sealing efficiency through wettability parameter alteration [45].

2.3 Geomechanics of Shale Caprock

The geomechanical properties of stress, strain, fracture and pore geometry, ductility, thickness and material homogeneity play important roles in shale caprock integrity in CO₂ sequestration. Table 2.2 shows the ductility position of shale as a caprock compared to others.

Table 2.2: Ductility ranking of different caprock lithologies [19]

Caprock lithology	Ductility
Salt	Most ductile
Anhydrite	
Organic-rich shales	
Shales	
Silty shales	
Calcareous mudstones	
Cherts	

In reservoir characterization for CO₂ sequestration projects, site screening and selection, risk assessment, monitoring, verification and account as well as simulation of CO₂ plume front depend heavily on the availability of data on the geomechanics of target formations. The same procedures apply to shale caprock evaluation for CO₂ containment over the long term.

Current and ongoing research into the behavior of various formations and shale caprock in particular suggests real but less catastrophic changes in the geomechanics of shale caprock when in contact with CO₂ over the long term. The major concerns are at the interface between the target repository and the top seal. Natural and induced fractures may act as leakage pathway in CO₂ sequestration, as flow through experiments showed the possibility of fracture aperture

evolution at low pH which are significantly affected by the clay content of the rock and may impede their growth [24]. Fault junctions also can serve as a source of concern in that they can be reactivated under adverse pressure perturbation that usually accompany engineered storage, though several probabilistic simulation have downplayed such plume encounter with faults [46, 47]. Most natural leakages of gas and oil from geologic reservoir have been through fault and the rest through permeable zones of poorly compacted rocks [48]. The concept of capillary pressure limit is not applicable as the subsurface fluid moves through the path of least resistance. The loss of drilling fluid may indicate fault reactivation as a result of large scale gas injection program [49, 50]. However the interaction of water with clay is suggested as capable of healing fractures. Long-term hydrotesting where a decrease in the transmissivity of the fracture network was observed, demonstrated this possibility [27].

Seepage modeling from outcrops and coal bed seams showed that geomechanical properties of shale caprock are more prominent in the short term when compared with geochemistry and hydrodynamics of formation water [51]. However this varies from formation to formation and each basin will need to be treated on its own merit. Database compilations are ongoing on natural analogues of subsurface leakage of gas such as in the Harlingen gas field in Holland, St Johns Dome in the USA and the dormant volcanoes of Cameroun [19, 35].

Crystal structure of constituent minerals in shale affects the measurement of geomechanical properties of interest in CO₂ sequestration. The determination of elastic modulus and hardness of a muscovite rich shale using nano-indentation showed that time is a critical factor in obtaining the appropriate results even at maximum load [12, 52-54]. The relationship between CO₂ gas transmissivity, fracture pore pressure and fracture volume stress is given by the following empirical formula, equation (9) for seepage of gases through fractures in coal [4]:

$$K_{fg} = K_{f0} \exp \left\{ -b \left[\frac{\sigma_1 - \beta_p}{K_n} \right] - c \left[\frac{1 - V_r}{E_r} (\sigma_2 + \sigma_3) - \frac{2V_r}{E_r} \sigma_1 \right] \right\} \dots \dots \dots (9)$$

where, σ_1 = maximum principal stress, σ_2 = intermediate principal stress, σ_3 = minimum principal stress, β_p = Biot Coefficient, b = coefficient reflecting the influence of normal deformation, c = coefficient reflecting the influence of tangential deformation, K_{fg} = coefficient of permeability of gas, K_{f0} = initial permeability of fracture, K_n = normal stiffness of fracture, V_r = Poisson's ratio of the rock sample, E_r = bulk modulus of the rock sample.

Poromechanical simulation results using empirical boundary conditions have shown that local shear or tensile failures can occur in shale caprock with a potential for plastic deformations particularly in depleted gas fields [55, 56]. Initial stress pattern is suggested to control plastic strain propagation and the lowering of horizontal stress may cause thorough plastic strain propagation through the entire caprock thickness while increasing the tendency for capillary breakthrough [57].

Several simulation workflow of the inter-relationship of geomechanical and petrophysical properties have been prepared from limited data available in other to visualize possible changes in shale over many decades [30, 58, 59].

These relationships are useful when optimizing the recovery of oil from a formation while simultaneously injecting CO₂ beneath it with interbedded shale rocks acting as either baffles or seal. Fluid densities can be expressed as functions of localized pressure and temperature that are prevailing in the reservoir [60, 61]. Large scale geotechnical sampling of shale caprock indicates that triaxial testing techniques can estimate rate dependent behaviors in caprock including nonlinear viscous properties and stress induced deformation rate [62, 63]. Data for short term geomechanical simulation of shale is provided under sequestration conditions.

2.4 Hydrodynamics

The driving forces for migration and leakage are modified under hydrodynamic conditions. Hydrodynamics in shale caprock refers to the sub-surface movement of water that affects the net force vectors acting on rocks and fluid as well as their geochemical interaction. Hydrodynamic flow has the tendency to either decrease or increase the driving pressure against seals and can thus modify the CO₂ column heights the seal can support. It supports buoyancy when a hydrodynamic upward force vector is exerted and vice versa. The hydrology of a regional seal can be ignored for all practical purposes except in basins with clear evidence of hydrodynamic activities such as in the Powder River Basin of Wyoming [19]. Simulation experiments similar to burial of high-level radioactive waste in shale rocks usually account for the hydrology of the formation particularly for ground water protection and radioactive cooling processes [64].

In addition, the occurrence of overpressure in a shale caprock may establish a local pore pressure gradient that can shore up the sealing capacity of adjacent normally pressured reservoirs such as in the Niger Delta region of West Africa. The parameters of interest in these type of shale hydrology are water-table depth, total dissolved solids (TDS), aquifer thickness and hydraulic connectivity [49]. The slow movement of sub-surface water makes estimation of its chemical transport impact on shale caprock hydrodynamics somewhat difficult though most rock-fluid interactions take place in the presence of water.

The hydrological behavior of most subsurface reservoirs particularly depleted oil and gas reservoirs, and saline aquifers are poorly understood demanding greater research focus such that the inter-relationship among geochemistry, geomechanics and hydrology can be established by making use of computational fluid dynamics techniques in geological models.

2.5 Coupled Processes in Shale Caprock-CO₂ Interaction

In general, multiple geological processes are taking place in shale caprock during CO₂ sequestration and this can be more pronounced due to diffusive and advection loss of CO₂ into the overlying seal. Geochemical, geomechanical and hydrological processes are expected to interact over time to define the integrity of a seal rock during CO₂ sequestration.

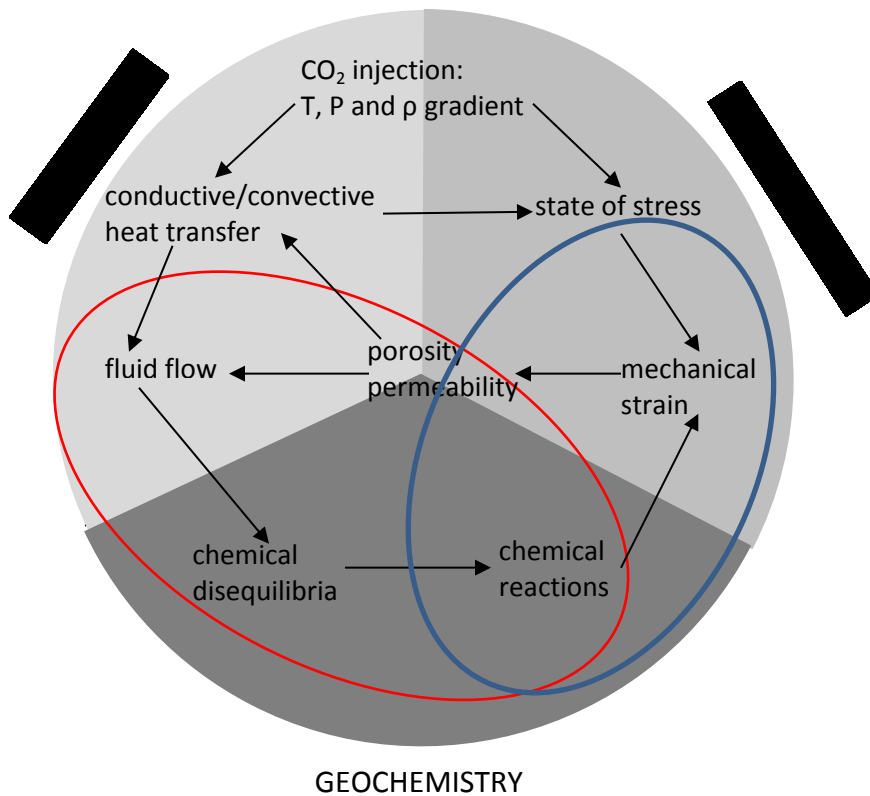


Figure 2.4: Coupled processes in caprock-CO₂ interaction showing critical parameters [48].

Modeling and experimental work in the past have attempted to capture the resultant effects of the coupled interaction of these processes requiring finer details about reaction kinetics, poro-elasticity of clay minerals and the precise role of water in the subsurface [65, 66].

Figure 2.4 and figure 2.5 depict some of the processes that are involved in geochemical and geomechanical interactions of seal rock and CO₂. Figure 2.5 particularly hints at the possibility

of geochemical changes in shale closing geomechanical apertures that originate as a result of large scale high pressure injection into the reservoir pore spaces. This research attempts to experiment with this possibility by examining petrophysical property changes.

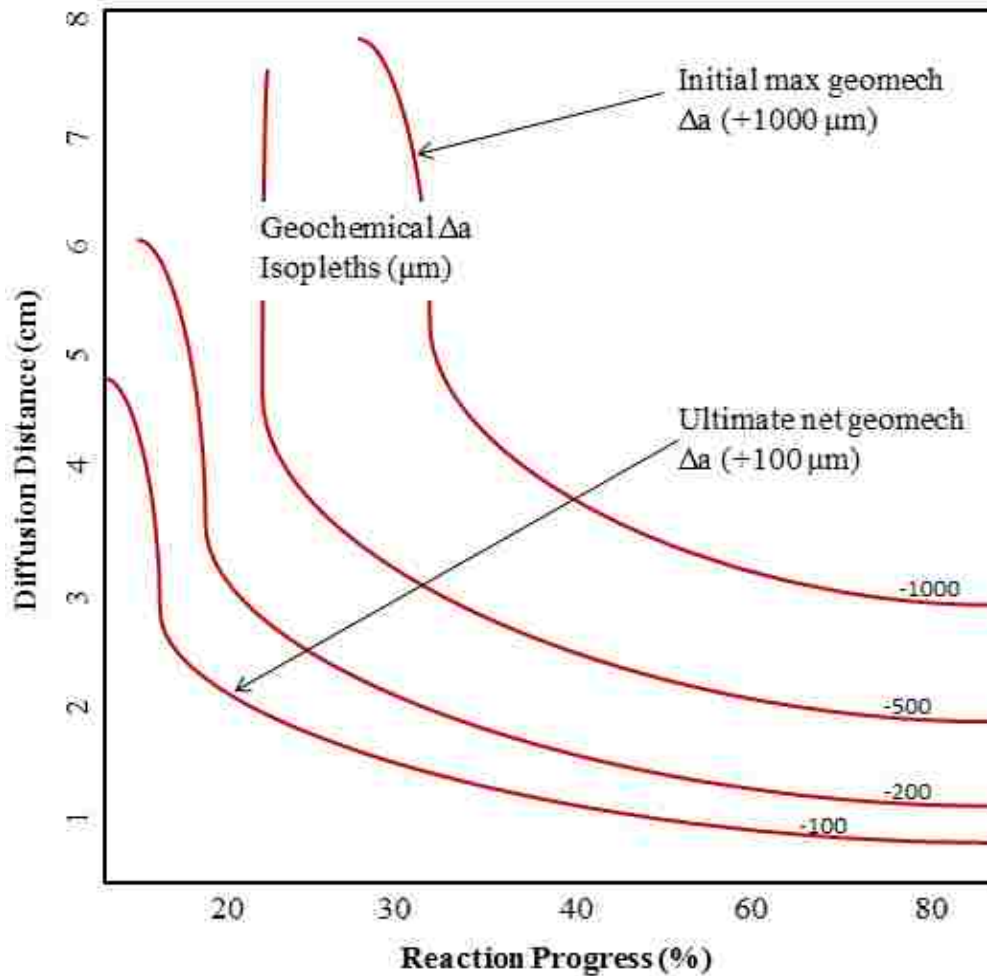


Figure 2.5: Geochemical counterbalancing of geomechanical processes within shale caprock (Adapted from Johnson et al., 2005) [29].

2.6 Dimensionless Numbers in Reactive Flow

Reactive flow is a crucial component of rock-fluid interaction research and studies have proved that the long term suitability of caprock in CO₂ sequestration might depend on the geochemical strength and weakness of the caprock [29, 67, 68]. The application and estimation of relevant dimensionless numbers can help in simplifying the magnitude as well as the extent of

reactive transport impact in shale caprock. At the macroscopic scale, reactive transport phenomenon is governed by the convection-diffusion equation; this is stated in equation (10):

$$\frac{\partial c}{\partial t} + \nabla \cdot (v^* * c - D^* * \nabla c) - \gamma^* * c = 0 \dots \dots \dots (10)$$

where c is the average concentration in the pore space, v^* is the mean velocity vector, D^* is the dispersive tensor and γ^* is the apparent reactivity coefficient. The characteristic time of the reaction is assumed to be small compared to the time needed for a full velocity field to develop [69].

The following dimensionless numbers which were used in previous research are considered relevant in CO₂ sequestration and shale caprock integrity.

2.6.1 Peclet Number

The Peclet Number (Pe) describes the effect of advection relative to that of molecular diffusion on solute transport [70]. It is essentially the ratio between convective and diffusive fluxes [69]. Equation (11) below defines Peclet Number mathematically:

$$Pe = \frac{vl}{D} \dots \dots \dots (11)$$

where v = fluid velocity (m/s), l = modal pore diameter (m), D = molecular diffusion coefficient (m²/s). These parameters and units are also applicable to Da and $PeDa$ numbers.

2.6.2 Damkohler Number

The Damkohler Number (Da) describes the effect of reaction relative to that of convection. It is the dimensionless factor that brings reactive flow into Peclet-Damkohler Number. The mathematical expression for Damkohler Number is given below in equation (12):

$$Da = \frac{\gamma_r}{v} \dots \dots \dots (12)$$

where γ_r = intrinsic kinetic rate(m/s) and v = characteristic fluid flow velocity (m/s).

2.6.3 Peclet-Damkohler Number

The Peclet-Damkohler Number ($PeDa$) describes the effect of reactive fluxes relative to diffusion and it is used frequently because convective effects diminish at the interface between two media [70, 71]. Pore geometry and specific properties play significant role in estimating this dimensionless number. Peclet-Damkohler Number is expressed as in equation (13) below:

$$PeDa = \frac{k_r l}{D} \dots \dots \dots (13)$$

where k_r =intrinsic kinetic rate(m/s), l =modal pore diameter (m), D =molecular diffusion coefficient (m²/s)

These dimensionless numbers capture the extent of dissolution/precipitation process in reactive transport through pore networks.

Accurate measurement of the key parameters that indicate reactive flow is required. Literature values that were obtained from some repeated experimental data were used in this research work.

2.7 Important Properties of Shale in CO₂ Sequestration

- 1) Shale has anisotropy (directional) properties. This is linked to the manner in which the sediments were deposited and the foliated nature of clay. Most physical properties of clay

are therefore anisotropic. Kinetics of fluid, ion transfer and general transport properties in shale are also dependent on anisotropy [27].

- 2) The hydraulic conductivity of effective shale cap rocks is in the order of 10^{-12} ms^{-1} and consequently their permeability are intrinsically low [27].
- 3) Poroelasticity: the low permeability of shales combined with a high anisotropy and a strong dependence on water content makes it a complex task to estimate the mechanical properties and poroelastic parameters of shales [27].
- 4) Geochemical composition of shale varies widely, having considerable influence on the mechanical and chemical stability of a lithology when considered as seal for underground CO_2 storage. In depleted hydrocarbon reservoirs, the storage of alien fluid such as CO_2 may cause some significant changes in the rock mineralogy over the long term [19].
- 5) The presence of quartz and carbonates in shale gives a reasonably high mechanical strength whereas clays and especially the swelling properties of smectite make shale deformable with a potential to creep [19].
- 6) The capillary entry pressure for shale is dependent on interfacial tension, permeability, cation exchange capacity among other factors [28].

2.8 Justification of Research Direction

The study of shale caprock in CO_2 sequestration entails researching into the effectiveness of the sealing mechanism involved. This mechanism is a function of the mineralogical composition of the shale caprock and its intrinsic petrophysical properties such as porosity and permeability. Geomechanical defects in the rock can also play a significant role in its sealing efficiency as faults slip and insitu stress alterations can aid the creation of potential pathways for

CO₂ leakage through existing natural fractures in the rock. This is of particular concerns in naturally fractured rocks where underground fluid flow influences CO₂ migration pattern.

Meanwhile most researchers have focused on the geochemical behavior of shale caprock and to a limited extent, the geomechanical effects that might be involved during large scale injection of CO₂. Most of these investigations were done using batch reactors in which a known mass of shale caprock was reacted in disproportionately large but fixed volume of CO₂-brine solution. This only mimics a static condition in which the concentration of CO₂ in the brine is depleted overtime. Conducting these experiments under a continuous contact mode of fresh CO₂-brine flooding and a known mass of shale caprock might yield different results.

This experimental research attempted to reactively interact shale caprock with CO₂-brine under continuous injection mode to investigate sub-surface behavior of caprock/aqueous CO₂ interaction.

CHAPTER 3 EXPERIMENTAL SETUP AND PROCEDURE

3.1 Experimental Methods and Sample Preparation

This experimental work applied specific analytical techniques in investigating changes in surface/near-surface properties of the shale rock after exposure (by flooding) to CO₂-brine, for a time frame ranging between 30 days to 92 days. The shale rock was comminuted (crushed) to predetermined dimensions that are suitable for use in analytical instrument [17, 22]. See figures A.2, A.3 and A.11 in appendix A. Particle sizes were of the order of 2mm – 3mm in length. Three flow cells were used with designs similar to a plug packed-bed. Each cell holds an average of 265g of shale caprock samples with similar mineralogy but distinctly different mineralogical ratio. This exposed as much surface area of the crushed shale as possible to CO₂-brine (figures 3.1 and 3.2). Multiple representative samples were analyzed and compared to corresponding control samples. An average of 26g from each cell was analyzed using the Brunauer-Emmett-Teller (BET) method, representing about 10% of each mineralogical ratio. All instrument and process devices are of stainless steel and PEEK (polyether ether ketone) material. This ensured that metallic corrosion processes do not interfere with critical measurements during the experiment. PEEK and stainless steel materials are generally resistant to CO₂-brine induced corrosion. Appendices A, B and C document the details of the experimental process with respect to CO₂-brine flooded sample selection, experimental procedures and selection of CO₂-brine reacted samples for analysis.

3.2 Experimental Setup

The experimental set-up consisted of three stainless steel pressure cells, a syringe pump (and a piston pump for backup), a back pressure regulator (BPR), accumulators (glass beaker), six pressure transducers, three pressure gauges, PEEK and stainless steel tubings, National

Instruments data acquisition device, a ceramic filter to prevent solid particles (larger than 50 μm) from flowing into the cells and a computer system. Schematics of the CO_2 -brine flooding of shale caprock are shown in Figures 3.1 and 3.2. The pressure cells were mounted vertically on a metal-wooden frame with aqueous CO_2 flowing from the top to the bottom of the experimental fixture. This is to prevent particle fluidization were it to be the other way round i.e bottom to top. Also the effect of gravity is assumed to be negligible. A schematic of the experimental setup is shown in figure 3.3. Figure A.1 in Appendix A has a picture of the experimental setup.

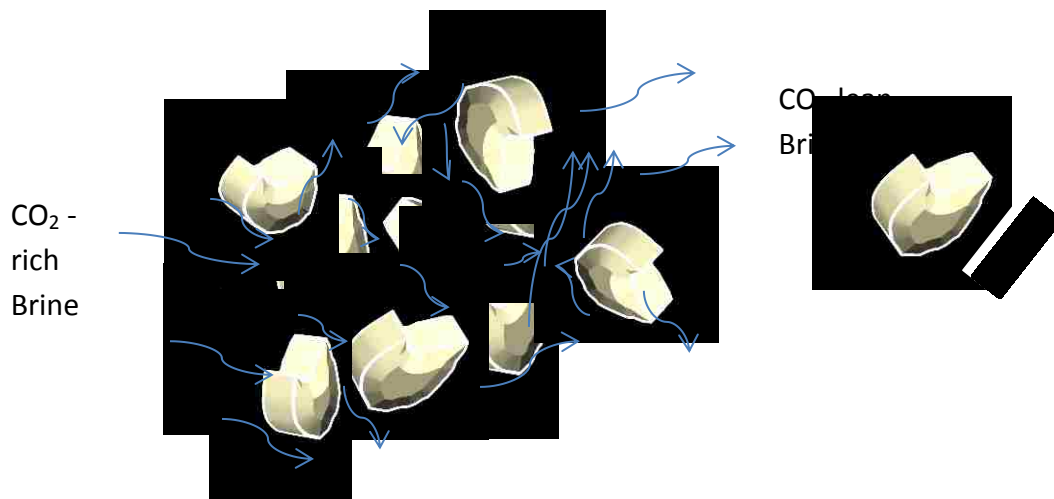


Figure 3.1: Schematics showing CO_2 -brine flooding of comminuted shale caprock

A picture of the experimental setup and all associated equipment as well as crushed shale rock preparation and sample size(s) are shown in Appendix A.

3.2.1 Pressure Cells

The pressure cells used in this experiment were stainless steel made with maximum pressure rating of 4000psi. The diameter and length of the cells were approximately 3in x 11in respectively and were water tight when assembled properly. There were four outlets for instrument connection and fluid injection/ejection. A metal/wooden fixture was used to anchor the cells vertically during the experiment. The thickness of the pressure cells provided the shield

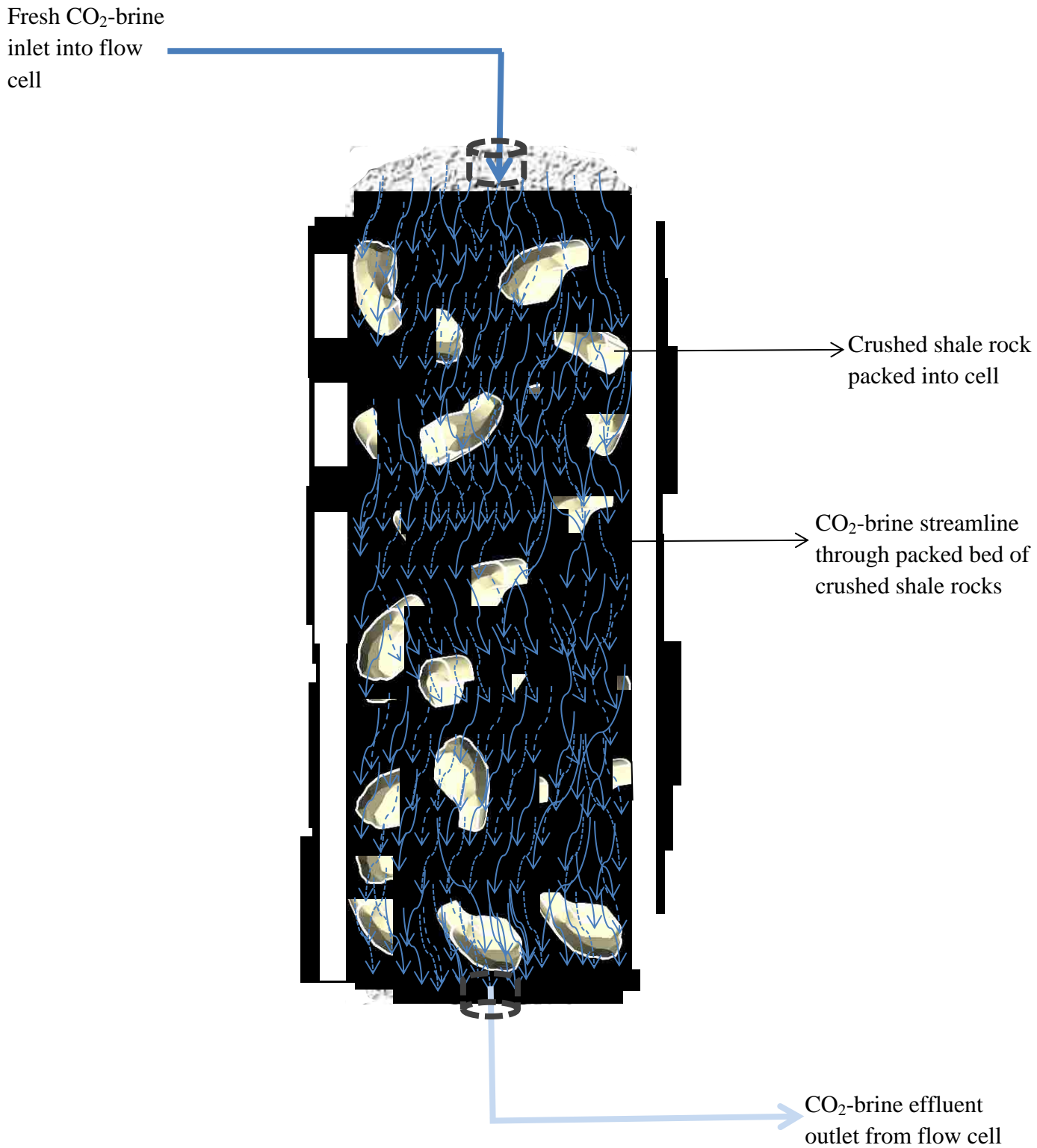


Figure 3.2: Schematic of CO₂-brine streamline through the shale caprock packed into the experimental flow cell. The sketch shows that the crushed shale samples are adequately contacted by the injected fluid which penetrated deep into all the pore spaces of the rock.

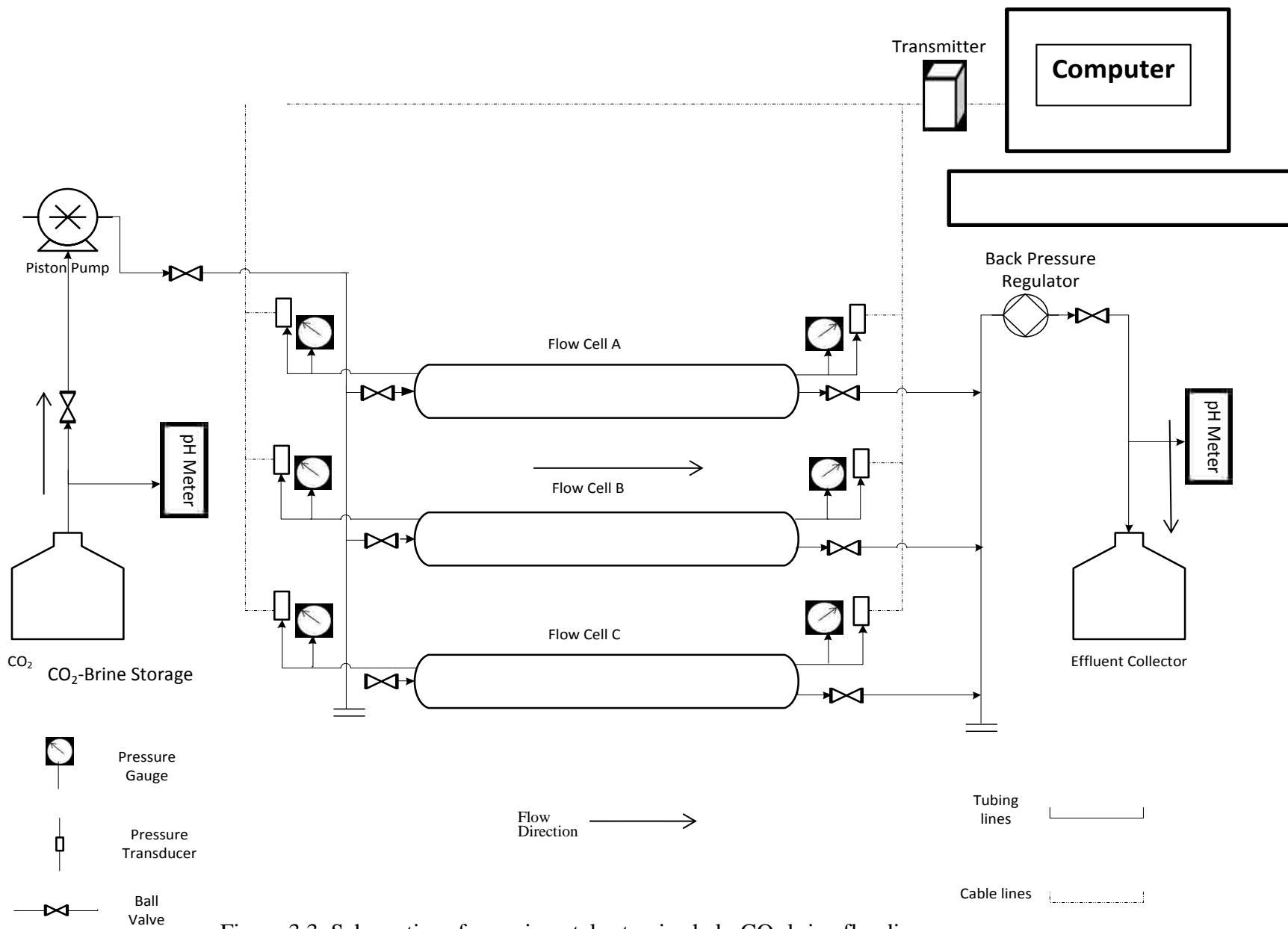


Figure 3.3: Schematics of experimental setup in shale-CO₂ brine flooding

for high pressure operations and the experimental procedure included pressures that were well below the maximum design pressure rating for the cells. A picture of the pressure cells are shown in figure A.1 in Appendix A.

3.2.2 Syringe Pump

A Teledyne Isco E500 model syringe pump system capable of providing flow rates from 0.001 ml/min to 207 ml/min was used in this study. The pump can produce pressures up to 3,750 psi. It consists of two individual pumps (pump A and B), with 507 ml capacity each, which can be operated in independent pump mode as well as in continuous flow mode by the electronic controller. Both pumps A and B were used during the experiments in auto refill mode to provide continuous flow. It requires approximately 2.5minutes to be refilled at a refill rate of 200 ml/min. Hence, CO₂ saturated brine was continuously pumped during the experiment. The pump is shown in figure A.4 in appendix A.

3.2.3 Data Acquisition System

Omega pressure transducers were used to record the pressure evolution data along the pressure cells with two transducers on each cell. The range of the transducers is 0 – 5000 psi with stated accuracy of 0.5% of the full pressure. The pressure transducers were connected to a National Instruments (NI) data acquisition device with insulated electrical wiring that was factory calibrated with the manufacturer's pump. Data was stored on a computer using National Instruments' proprietary software Labview. The device can be seen in figure A.1 in Appendix A.

3.2.4 Back Pressure Regulator (BPR)

A back pressure regulator (BPR), manufactured by Temco Inc.,Tulsa, OK, was used to achieve higher injection pressures. The BPR can accommodate flow rates up to 10 ml/min.

Dome pressure was applied using Nitrogen (N₂). The upstream pressure (the pressure in the outlet) was adjusted to a value very close to the applied dome pressure (one to one ratio). Nitrogen supply cylinder and the BPR device can be seen in figures A.7 and A.8 respectively in appendix A.

3.3 Experimental Process Parameters

The following experimental conditions were used during the shale/CO₂-brine flooding study:

- a. Global flow rate: 0.9ml/min or 0.3ml/min/cell
- b. Flow cell back pressure: 970 psi. Appendix A details the justification of this value.
- c. Operating temperature: ambient
- d. CO₂ – brine pH: 3.70 - 4.01

3.4 Experimental Shale Caprock Geology

The shale caprock of the Pottsville Formation (Pennsylvanian Age) in Alabama was used in this experiment. Whole core samples of the shale caprock were obtained from three monitoring wells for the CO₂ Enhanced Coal Bed Methane (ECBM) Project of the Southeast Regional Carbon Sequestration Partnership (SECARB) in the Black Warrior Basin, Alabama.

The Black Warrior basin is a late Paleozoic foreland basin that formed in response to converging thrusts and sediment loads in the Ouachita and Appalachian orogenic belts. Regional dip is toward the southwest, and broad Alleghanian folds and numerous northwest-striking normal faults occur in the eastern part of the basin. The Pottsville Formation is exposed at the surface in the eastern part of the basin and is overlain with angular unconformity in the western two-thirds of the area by poorly consolidated Mesozoic and Cenozoic strata of the Gulf coastal plain and Mississippi Embayment. Burial depths of the upper part of the Pottsville Formation in

coal bed methane fields of the Black Warrior basin range from 0 to about 4925 ft. In the Early Permian, the formation was buried at maximum depths of approximately 2–3 km. Fracture systems in the Black Warrior basin are diverse and consist of joints, cleats, and faults [72].

Figure 3.3 below shows the stratigraphic layers at the geologic site:

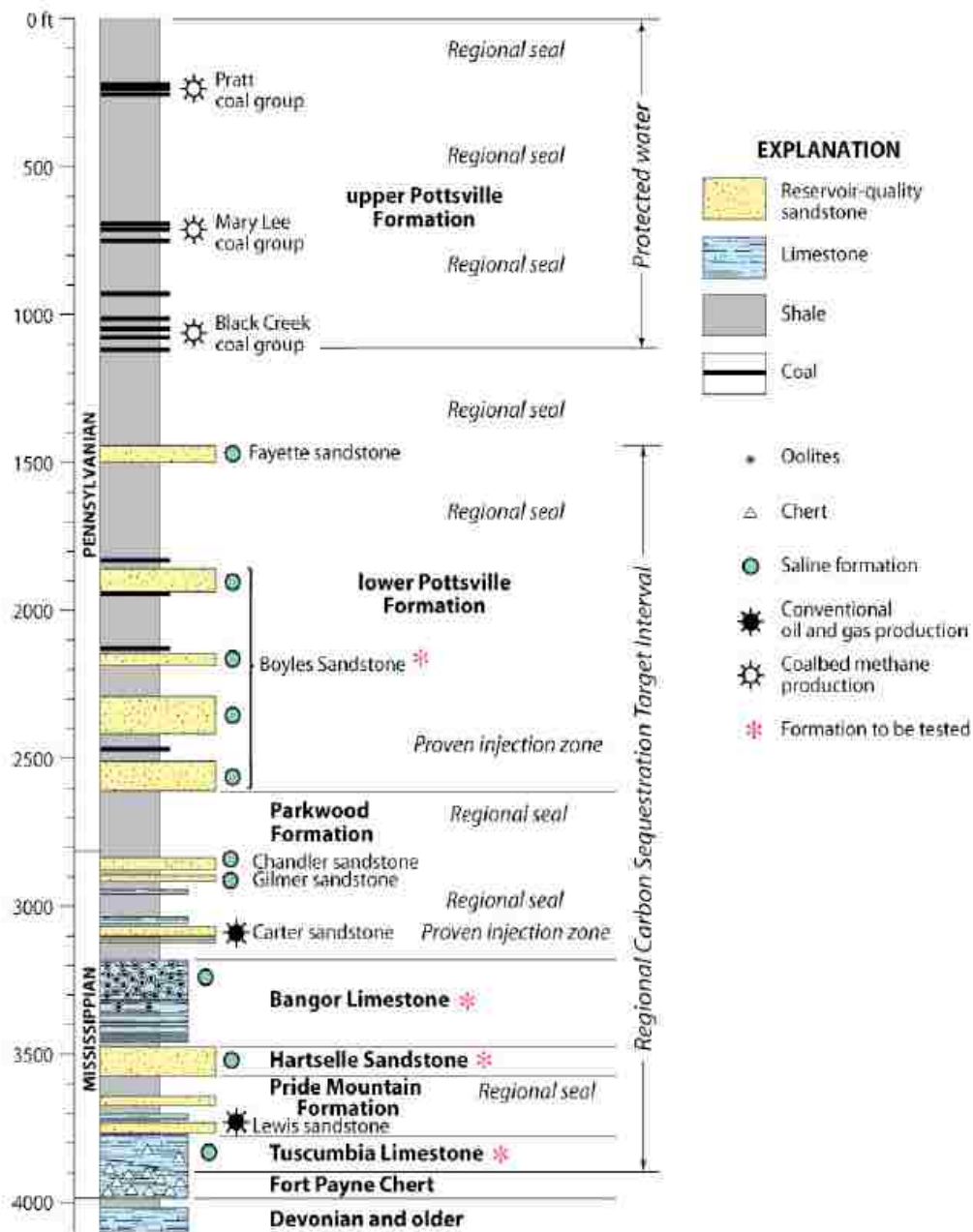


Figure 3.3: Stratigraphic profile of the Pottsville Formation showing shale sample location (Courtesy of the Department of Energy) [73].

Figure 3.4 showed the shale caprock samples with codes corresponding to the monitoring wells from which the cores were drilled and the red points for crushed sample locations. Final selection of samples based on mineralogy uses a ternary plot of percentage composition of major minerals in the shale caprock. This is discussed further in the results and discussion chapter.



Figure 3.4: Physical shale caprock cores from the Pottsville Formation, Alabama

3.5 Experimental CO₂-brine Fluid

Carbon dioxide saturated brine solution was used for all experiments. Brine was prepared with distilled water to ensure that unknown species were not present in the solution. The brine composition was originally designed to simulate West Texas formation fluids. This original brine contained Mg and CaCO₃ in minor amounts. The composition was then simplified to include only NaCl and KCl. As seen in the Table 3.1, the brine solution contained ~ 2% dissolved solids. After mixing water and salts, the brine was filtered using filter paper to eliminate undissolved

solid particles that can plug the flow lines in the experimental set-up. A filter was also installed upstream of injection to reduce the risk of plugging the flow lines. An accumulator (volume ~25 liters) was used to hold the brine solution as CO₂ was bubbled through at 25 psi for approximately 80 mins resulting in average pH value of 3.9 over the course of the experiment. This method was selected because of ease of preparation. A digital pH meter was used to record pH measurements every morning and calibration was done with standard buffer solutions (pH= 4, 7, 10) each week. Figure A.6 in Appendix A shows the setup for CO₂-brine preparation.

Table 3.1: Experimental brine composition for Shale/CO₂-brine flooding experiment

Chemical Reagents	Molecular Weight	Amount added to 1 l of Distilled Water	Molality (mol/kg)
Sodium Chloride (NaCl)	58.45g/mol	20.196g	0.3455m
Pottassium Chloride (KCl)	74.6g/mol	0.345g	0.0046m

3.6 Techniques in Rock and Fluid Analysis

Prior to and after the experiments, various material characterization techniques were employed to assess the internal and external mineralogical and petrophysical alterations of the shale caprock. The following discusses the specific analytical tools used for fluid and shale caprock analysis.

3.6.1 Inductively Coupled Plasma-Optical Emission Spectroscopy (ICP-OES)

Analysis of influent/effluent fluid included metallic mineral evaluation of the influent and the effluent which established the expected geochemical alterations in the rock with CO₂-brine depletion [74]. ICP-OES is a method which was conducted to determine metallic cation contents in the fluid. The fundamental characteristic of this process is that each element emits energy at specific wavelengths peculiar to its atomic character. By determining which wavelengths are

emitted by a sample and their intensities, the analyst can determine the elements from the given sample relative to a reference standard qualitatively and quantitatively. The samples were analyzed in the LSU Department of School of Plant, Environmental and Soil Sciences. During the experiments, effluent brine samples were monitored for pH and collected daily while samples were selected for ICP-OES analysis depending on pH values.

3.6.2 X-Ray Diffraction (XRD) Analysis

X-Ray Diffraction was used in the mineralogical analysis of the shale caprock- the inorganic mineral composition [28, 75]. XRD is a bulk analysis technique, used to determine the mineralogical content of a core sample, in which the section of interest is powdered and placed inside the X-Ray diffractometer. X-rays are emitted and rotated from 2 to 70 degrees at a step of 0.02 degree increments with Cu K α 1 (copper) radiation. The X-ray source sends the signal and receives a response. Each mineral has a characteristic response. Computer software determines the type of mineral and outputs peak versus intensity plots for the minerals present in the core sample. Since XRD can only determine crystalline substances, amorphous materials present cannot be identified by XRD. XRD analyses were conducted on the control sample and the CO₂-brine contacted samples in the LSU Geology Department using a Siemens Kristalloflex D5000 X-Ray diffractometer shown in Figure A.9 in appendix A.

3.6.3 Energy Dispersive Spectroscopy (EDS)

EDS is a spot elemental analysis that can be used while imaging surfaces with Scanning Electron Microscopy. It detects the chemicals that are present in the section of interest. When it is used on a low magnification image, it also detects chemicals surrounding the section being analyzed. This technique is a powerful tool to detect an increase or reduction in elemental

components that may indicate precipitation and dissolution. Samples can be in solid chip form or grounded into powder for effective elemental analysis. Single or multiple point surface impact and capture is obtainable from this technique.

3.6.4 Optical and Scanning Electron Microscopy (SEM) Imaging

SEM is a technique that was used to examine physical changes on the surface of the shale particles providing useful information at high magnification and resolution. Portions of CO₂-brine contacted and uncontacted crushed shale caprock samples were imaged using SEM for microstructural characterization. SEM was deployed to further investigate the nature of altered surfaces at a much finer scale and under low vacuum conditions in order to obtain clearer images during the analysis. Micro-porous spaces can be identified from the captured images. The SEM images were obtained using an EDAX model electron microscope at the Center for Material Characterization, in the LSU Mechanical Engineering Department. Light microscopy images were obtained using a Leica microscope at the LSU Sustainable Energy and Environmental Laboratory.

3.6.5 Brunauer, Emmet and Teller (BET) Technique

This is a nitrogen adsorption technique used as an indicator of petrophysical changes in the comminuted (crushed) shale caprock as a result of geochemical alterations [76, 77].

a) Surface Area

The Brunauer-Emmett-Teller (BET) method is the most widely used procedure for the determination of the surface area of solid materials. It involves the use of the BET equation (14).

$$\frac{1}{W((P_o/P) - 1)} = \frac{1}{W_m C} + \frac{C - 1}{W_m C} (P/P_o) \dots \dots \dots (14)$$

in which W is the weight of gas adsorbed at a relative pressure, P/P_0 (P = equilibrium pressure, P_0 = saturation pressure) and W_m is the weight of adsorbate constituting a monolayer of surface coverage. The term C , the BET constant, is related to the energy of adsorption in the first adsorbed layer and consequently its value is an indication of the magnitude of the adsorbent/adsorbate interactions [36, 78].

b) Multipoint BET Method

The BET equation (14) requires a linear plot of $1/[W(P_0/P)-1]$ vs P/P_0 which for most solids, using nitrogen as the adsorbate, is restricted to a limited region of the adsorption isotherm, usually in the P/P_0 range of 0.05 to 0.35. This linear region is shifted to lower relative pressures for microporous materials [79].

The standard multipoint BET procedure requires a minimum of three points in the appropriate relative pressure range. The weight of a monolayer of adsorbate W_m can then be obtained from the slope s and intercept I of the BET plot. From equation (14), (15), (16) and (17)

$$s = \frac{C - 1}{W_m C} \dots \dots \dots (15)$$

$$s = \frac{1}{W_m C} \dots \dots \dots (16)$$

$$W_m = \frac{1}{s + i} \dots \dots \dots (17)$$

The second step in the application of the BET method is the calculation of the surface area. This requires knowledge of the molecular cross-sectional area A_{cs} of the adsorbate molecule. The total surface area S_t of the sample can be expressed as in equation (18):

$$S_t = \frac{W_m N A_{cs}}{M} \dots \dots \dots (18)$$

where N is Avogadro's number (6.023×10^{23} molecules/mol) and M is the molecular weight of the adsorbate. Nitrogen is the most widely used gas for surface area determinations since it exhibits intermediate values for the C constant (50-250) on most solid surfaces, precluding either localized adsorption or behavior as a two dimensional gas. For the hexagonal close-packed nitrogen monolayer at 77 K, the cross-sectional area A_{cs} for nitrogen is 16.2 \AA^2 .

The specific surface area S of the solid can be calculated from the total surface area S_t and the sample weight w, according to equation (19):

$$S = \frac{S_t}{w} \dots \dots \dots (19)$$

Cumulative properties of specific surface area and pore volume are obtained by adding their values for measured pore diameters up to the largest detected pore size. Figure A.10 in Appendix A shows the LSU Chemical Engineering Quantachrome Autosorb equipment used for the BET analysis.

c) Total Pore Volume and Average Pore

The total pore volume is derived from the amount of vapor adsorbed at a relative pressure close to unity, by assuming that the pores are then filled with liquid adsorbate. If the solid contains no macropores the isotherm will remain nearly horizontal over a range of P/P_0 approaching unity and the pore volume is well defined. However, in the presence of macropores the isotherm rises rapidly near $P/P_0 = 1$ and in the limit of large macropores may exhibit an essentially vertical rise. In this case the limiting adsorption can be identified reliably with the

total pore volume assuming careful temperature control of the sample. The volume of nitrogen adsorbed (V_{ads}) can be converted to the volume of liquid nitrogen (V_{liq}) contained in the pores using equation (20).

That is,

$$V_{liq} = \frac{P_a V_{ads} V_m}{RT} \dots \dots \dots (20)$$

in which P_a and T are ambient pressure and temperature, respectively, and V_m is the molar volume of the liquid adsorbate (34.7 cm³/mol for nitrogen).

Since pores which would not be filled below a relative pressure of 1 have a negligible contribution to the total pore volume and the surface area of the sample, the average pore size can be estimated from the pore volume. For example, assuming cylindrical pore geometry (type A hysteresis), the average pore radius r_p can be expressed as in equation (21);

$$r_p = \frac{2V_{liq}}{S} \dots \dots \dots (21)$$

where V_{liq} is obtained from previous equation and S is the BET surface area. For other pore geometries a knowledge of the shape of the hysteresis in the adsorption/desorption isotherm is required.

d) Pore Size Distributions

The distribution of pore volume with respect to pore size is called a pore size distribution. It is generally accepted that the desorption isotherm is more appropriate than the adsorption isotherm for evaluating the pore size distribution of an adsorbent [79]. The desorption branch of

the isotherm, for the same volume of gas, exhibits a lower relative pressure, resulting in a lower free energy state. Thus, the desorption isotherm is closer to true thermodynamic stability. Since nitrogen has been used extensively in gas adsorption studies, it has been well-characterized and serves as the most common adsorbate for pore size distribution measurements. The distribution of pore sizes can be expressed with respect to the specific pore volume and area of the sample being analyzed. Mesopore size calculations are made assuming cylindrical pore geometry using the Kelvin equation (22) in the form of reversed ratio:

$$r_k = \frac{-2\gamma V_m}{RT \ln(P/P_0)} \dots \dots \dots (22)$$

where

γ = the surface tension of nitrogen at its boiling point (8.85 ergs/cm² at 77 K).

V_m = the molar volume of liquid nitrogen (34.7 cm³/mol).

R = gas constant (8.314x10⁷ ergs/deg/mol).

T = boiling point of nitrogen (77 K).

P/P_0 = relative pressure of nitrogen.

r_k = the Kelvin radius of the pore.

The working fluids used in this BET technique application were nitrogen and helium.

The various techniques discussed above were used to correlate mineralogy, pore geometry and time of exposure to the geochemical strength of the shale caprock.

CHAPTER 4 RESULTS AND DISCUSSION

4.1 Selection of Shale Caprock Samples and Back Pressure Magnitude

The selection process for the experimental samples involved the use of a ternary diagram (figure 4.1) which compared the weight percent of the samples' bulk clay, quartz and feldspar. These minerals are the most significant (by percentage) in the shale caprock samples

Table 4.1: Experimental shale caprock mineralogy in weight percents of its major components

S/N	Samples	Wt %			
		Bulk Clay -Muscovite -Chlorite -Kaolinite	Quartz	Feldspar -Orthoclase -Albite	
1	2EBC1	47.45	47.51	5.04	} Cell C
2	ENML3	56.6	40.62	2.78	
3	2EPR1	65.05	32.54	2.41	} Cell B
3	2EPR4	64.99	33.73	1.28	
4	CEBC5	76.98	21.53	1.49	} Cell A
5	CEML5	73.26	24.85	1.89	

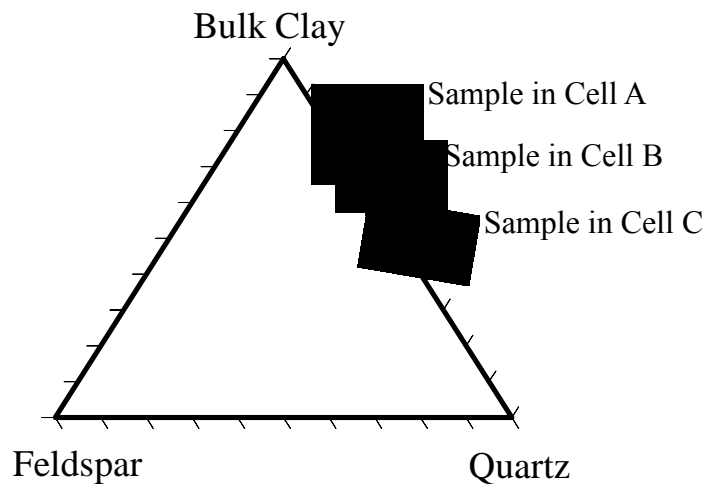


Figure 4.1: Ternary plot of shale caprock mineralogy showing the content of experimental cells

Figure 4.1 (constructed from table 4.1) above captures the mineralogical content of Cell A (sample A), Cell B (sample B) and Cell C (sample C) which consist of mixtures of rock samples CEBC5 and CEML5, 2EPR1 and 2EPR4, and 2EBC1 (shown in figure 3.4) respectively. This grouping was based primarily on the closeness of the percentages of the bulk clay and the quartz contents for samples A and B, while that of sample C considered the relatively higher percentage of feldspar in it (5.04%) as well as the 1:1 ratio of bulk clay and quartz. The ratio of bulk clay to quartz in samples A and B are approximately 3:1 and 2:1 respectively. Appendix A has the details of the procedures that were followed in sample collection and preparation for XRD analysis.

4.2 Geochemical Analysis of Fluid and Rock

4.2.1 pH Profile

Geochemical activity of the shale caprock was reflected in the pH evolution chart as shown in figure 4.2. The experimental samples were flooded at a flow rate of 0.3ml/min/cell at a back pressure of 970psi. This back pressure value was arrived at based on literature values of capillary entry pressure for shale rocks as reported by Al-Bazali et al., in 2005 using Oil-Based Mud, Decane, Crude Oil and Nitrogen Gas. Appendix A details the justification for this back pressure value.

The initial 20 days of the experiment produced effluents that suggest alkaline buffering capability of the rock. The pH climbed to a maximum of 8.6 within the first 3 days of the experiment before gradually decreasing at a negative slope of 1.29. The next 50 days of the experiment resulted in a nearly flat pH value (approximate slope of zero) with a sustained ability for keeping the pH to between 6 and 6.5 for a larger part of the experiment. This indicates some resilience in the geochemical pH alteration of the connate water that may be present in the rock.

The final 20 days saw a less steep decrease (a negative slope of 0.89) in the pH of the effluent with a tendency towards equilibrating with the influent pH. This suggests a waning buffering strength of the shale rock as it continued to be flooded with fresh CO₂-brine solution. It should be noted that mixed effluent of the fluids from all the three samples were tested for pH. This was because of limitations in experimental setup that would have required three different back pressure regulators. One back pressure regulator was used to impose the 970psi pressure required for the three cells and a larger header leading into the inlet tubings of the pressure cells was used to minimize flow constriction. Procedure for collection of effluent sample for pH measurements is documented in Appendix A and data points for the pH profile can be found in Appendix B.

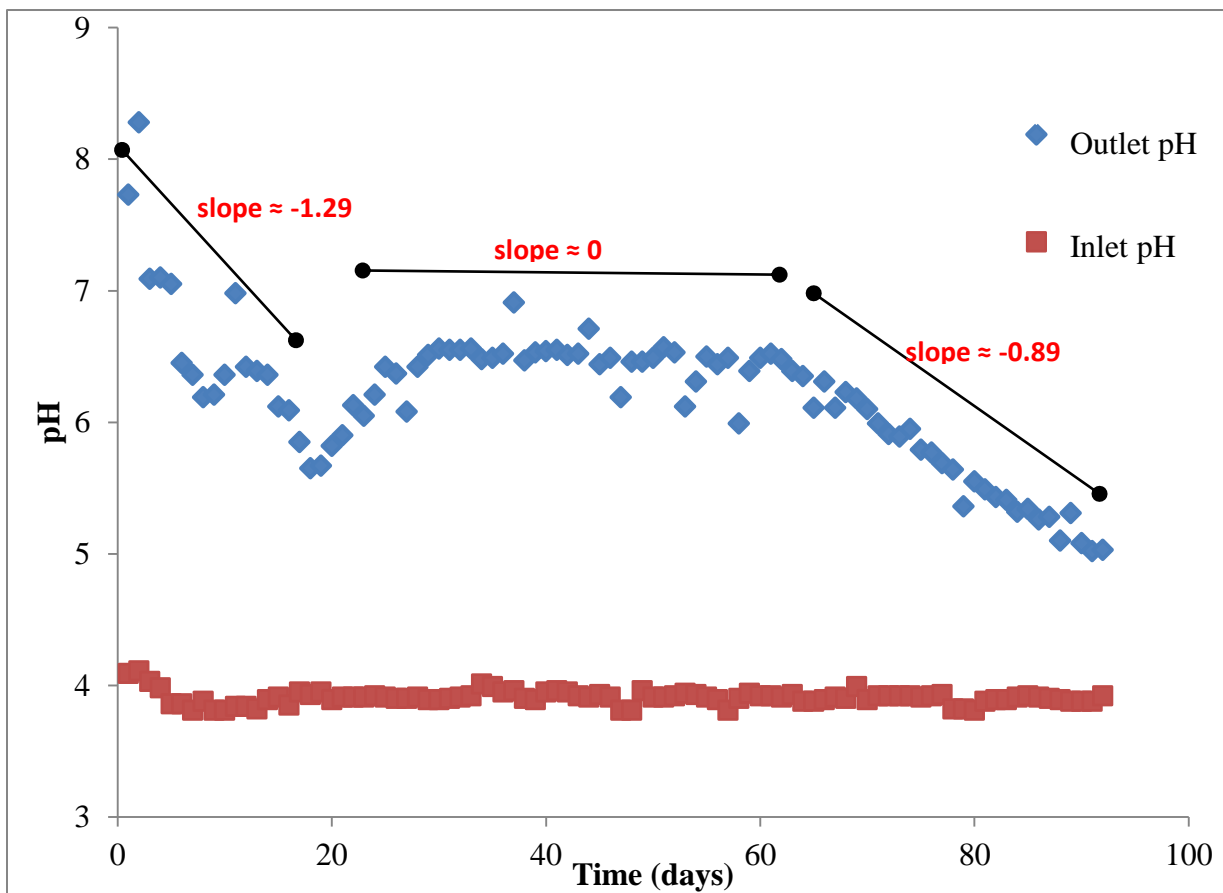


Figure 4.2: pH evolution chart for shale/CO₂-brine flooding effluents over the 3 months experimental period. Three distinct regions of pH change indicate the geochemical buffer strength of the shale caprock under continuous contact mode

4.2.2 Inductively Coupled Plasma Optical Emission Spectrometry (ICP-OES)

Figure 4.3 presents a plot of the analysis of the effluent solution for common metallic ions (cations) that are present in the rock sample with the exception of the cations that are already present in large amount within the influent fluid i.e Sodium (Na^+) and Potassium (K^+) within the CO_2 -brine. Calcium (Ca^{2+}), Magnesium (Mg^{2+}), Iron (Fe^{2+}), Manganese (Mn^{2+}), Aluminum (Al^{3+}) and Silicon (Si^{2+}) were identified in parts per million (ppm) values ranging between 0 and 60. Na^+ and K^+ were excluded because of their high concentration in the CO_2 -brine injected. The measured values for Na^+ and K^+ are included in the data section of Appendix B. The plot showed an unexpectedly high concentration of Calcium ions which are probably leached out of the rock, followed by Mg^{2+} , Si^{2+} , Al^{3+} , Mn^{2+} and $\text{Fe}^{2+/3+}$ in that order of concentration. The inserted graph shows the concentration distributions of the cations that are less than 5ppm in the effluent. The minerals that are suspected of releasing these cations as identified by X-Ray Diffraction (XRD) analysis include magnesium-rich Muscovite $[(\text{K},\text{Na})(\text{Al},\text{Mg},\text{Fe})_2(\text{Si}_3\text{Al})\text{O}_{10}(\text{OH})_2]$, Iron-rich Chlorite $[(\text{Mg},\text{Fe})_6(\text{Si},\text{Al})_4\text{O}_{10}(\text{OH})_8]$, Kaolinite $[\text{Al}_2\text{Si}_2\text{O}_5(\text{OH})_4]$, Orthoclase $[(\text{KAlSi}_3\text{O}_8)]$ and Albite $[(\text{NaAlSi}_3\text{O}_8)]$.

These alkaline earth metals-rich minerals are the constituents of the bulk clay and feldspar which are present in the samples flooded. The presence of these minerals may also be the reason for their alkaline buffering strength reflected in the pH measurements. The ability of these minerals to exchange the alkaline earth metals in form of cations with carbonate anions under oxygen deprived conditions may be able to produce precipitates capable of plugging nan-scale defects that may exist in a shale caprock. Formation of complexes with water may aid reaction progress. Procedure for collection of effluent sample for ICP-OES analysis is documented in Appendix A and the data points for the ICP profile can be found in Appendix C.

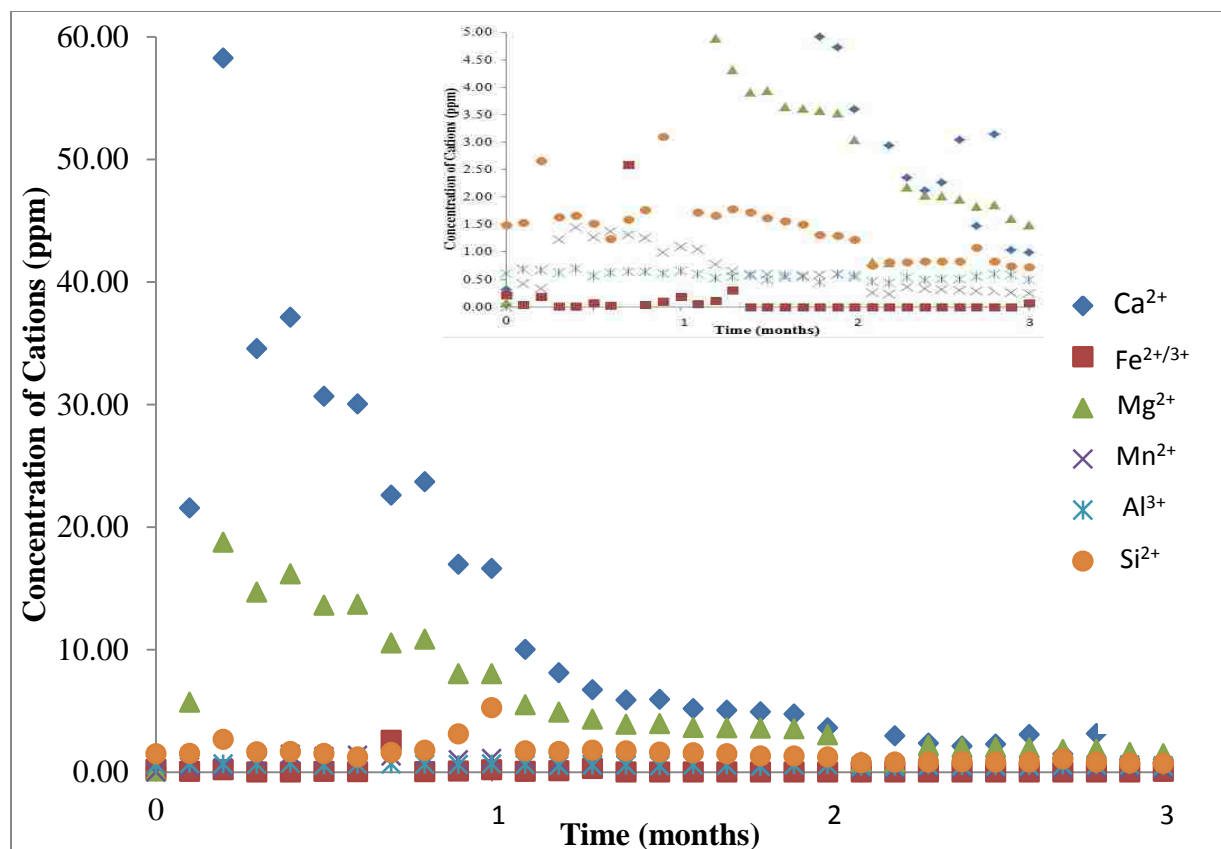


Figure 4.3: ICP-OES cation identification in effluent collected from shale/CO₂-brine flooding over the 3 months experimental period. It showed Ca²⁺ as having the highest part per million concentration out of the five alkaline earth metals analyzed in the effluent. The lower 5ppm portion of the graph is inserted to show the concentrations of Fe²⁺, Mn²⁺, Al³⁺ and Si²⁺

4.2.3 XRD Analysis

X-ray diffraction (XRD) analysis was used to analyze the geochemical properties of the bulk caprock over 92 day, once each month. The results as presented in figures 4.4, 4.5 and 4.6 showed that mineralogical alterations within the shale caprock are such that the relative amount of the clays particularly muscovite and chlorite are altered. These alterations are reflected in the variations of the heights of these minerals on the XRD diffractogram. Tables 4.2, 4.3 and 4.4 show the approximate percentage change in the mineralogy of the rock samples after three months of flooding with CO₂-brine. The quantitative percentage change in these samples are low as can be expected from the part per million concentration levels of critical cations that are in the

Table 4.2: Percentage (%) change in the mineralogical composition of Sample A after months of CO₂-flooding

	Muscovite	Chlorite	K-Feldspar	Quartz	Albite	Kaolinite
1st month	-1.45	-2.20	-0.33	1.67	1.38	2.92
2nd month	-1.45	-1.71	-1.33	1.67	2.41	2.5
3rd month	1.23	-1.22	-1.33	1.75	3.10	3.33

Table 4.3: Percentage (%) change in the mineralogical composition of Sample B after months of CO₂-flooding

	Muscovite	Chlorite	K-Feldspar	Quartz	Albite	Kaolinite
1st month	-2.8	-1.88	-0.37	1.31	-3.68	-0.28
2nd month	-0.6	-0.94	-1.48	1.39	-2.11	-1.39
3rd month	-0.8	-0.94	-0.74	1.64	-2.89	1.11

Table 4.4: Percentage (%) change in the mineralogical composition of Sample C after months of CO₂-flooding

	Muscovite	Chlorite	K-Feldspar	Quartz	Albite	Kaolinite
1st month	-0.53	-1.25	0.91	1.48	-1.2	1.19
2nd month	-2.11	0.63	-0.91	1.48	-0.8	0.48
3rd month	0.26	1.25	0.45	1.56	-0.6	0.24

ICP effluent analysis. This suggests that the changes are occurring at the micropore to nanopore levels. The percentage change showed an increase in Kaolinite for samples A and C while sample B had an overall decrease in percentage over the flooding period. Muscovite and chlorite decreased in the first two months of the experiment with the third month having stable values for all the three samples. Feldspar also exhibited a noticeable change in percentage weight decreasing mainly for samples A and B. These minerals are predicted by Johnson et al., to play active role in geochemical interaction of shale and aqueous CO₂ as depicted by equation (8). The reversible reaction shows that k-feldspar and chlorite are critical reactants that are necessary for increased content of kaolinite and muscovite in the rock samples.

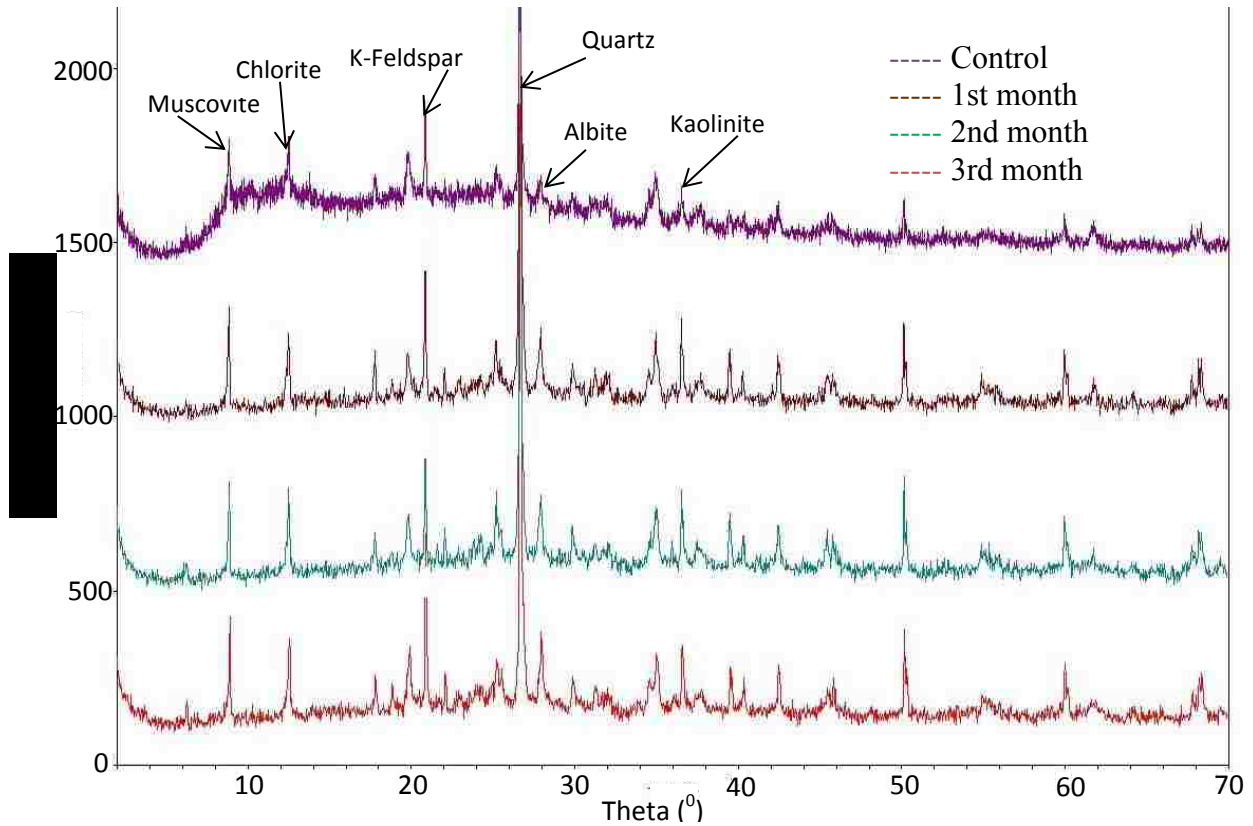
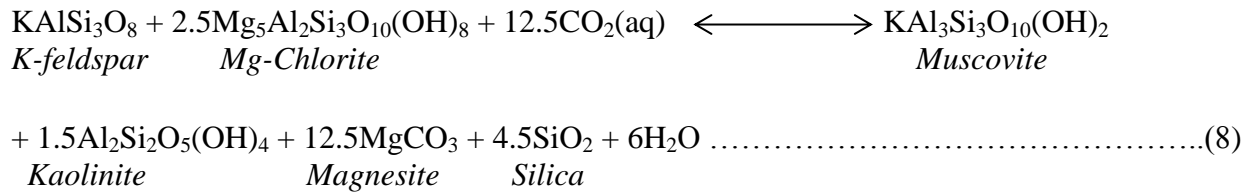


Figure 4.4: X-ray diffractogram for bulk mineralogical analysis of CO₂-brine contacted shale (sample A) before and after the three months experiment. It showed less noise in the CO₂-brine contacted sample indicating reduced amorphous content



Moreover, the XRD analysis of precipitates (Figure 4.7) that were formed from the effluent stored in a repository showed an amorphous material with some quartz content.

The reduction in noise level of figures 4.4, 4.5 and 4.6 indicates that a geochemical cleaning out of amorphous content in the caprock have occurred, leading to the trend in figure 4.7. Procedure for collection of rock samples for XRD analysis is documented in Appendix A.

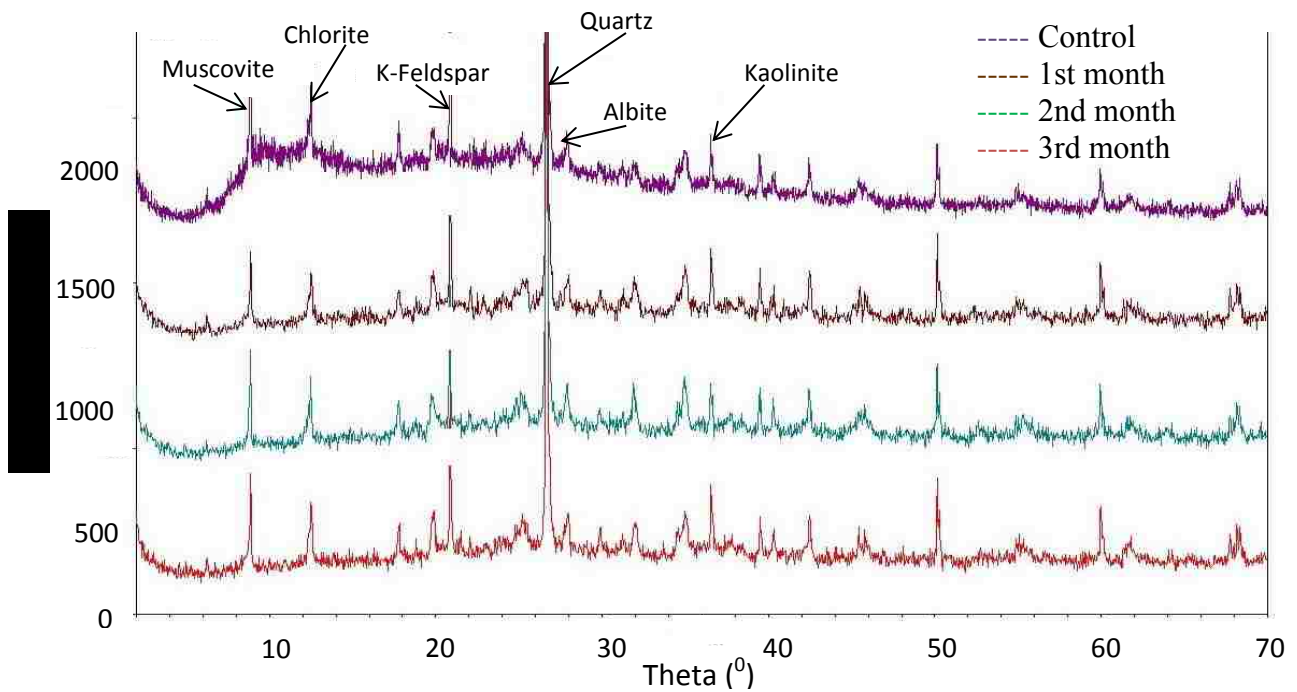


Figure 4.5: X-ray diffractogram for bulk mineralogical analysis of CO₂-brine contacted shale (sample B) before and after the three months experiment. It showed less noise in the CO₂-brine contacted sample indicating reduced amorphous content

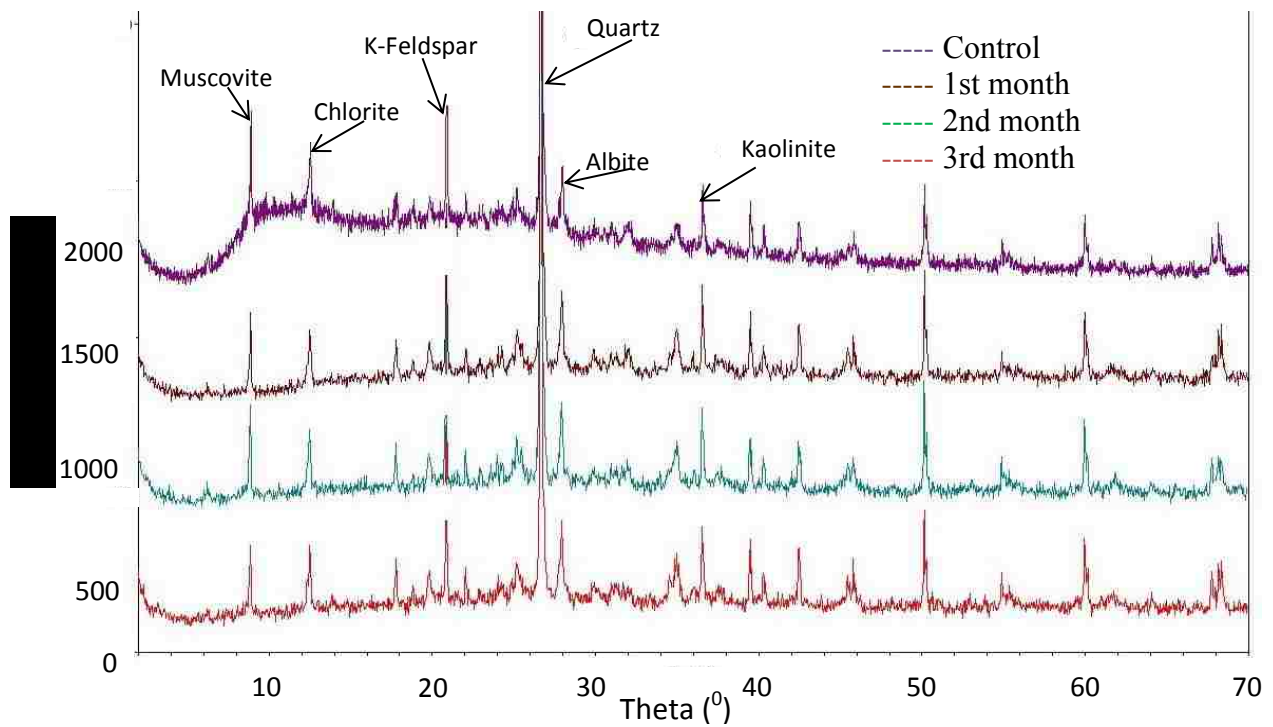


Figure 4.6: X-ray diffractogram for bulk mineralogical analysis of CO₂-brine contacted shale (sample C) before and after the three months experiment. It showed less noise in the CO₂-brine contacted sample indicating reduced amorphous content

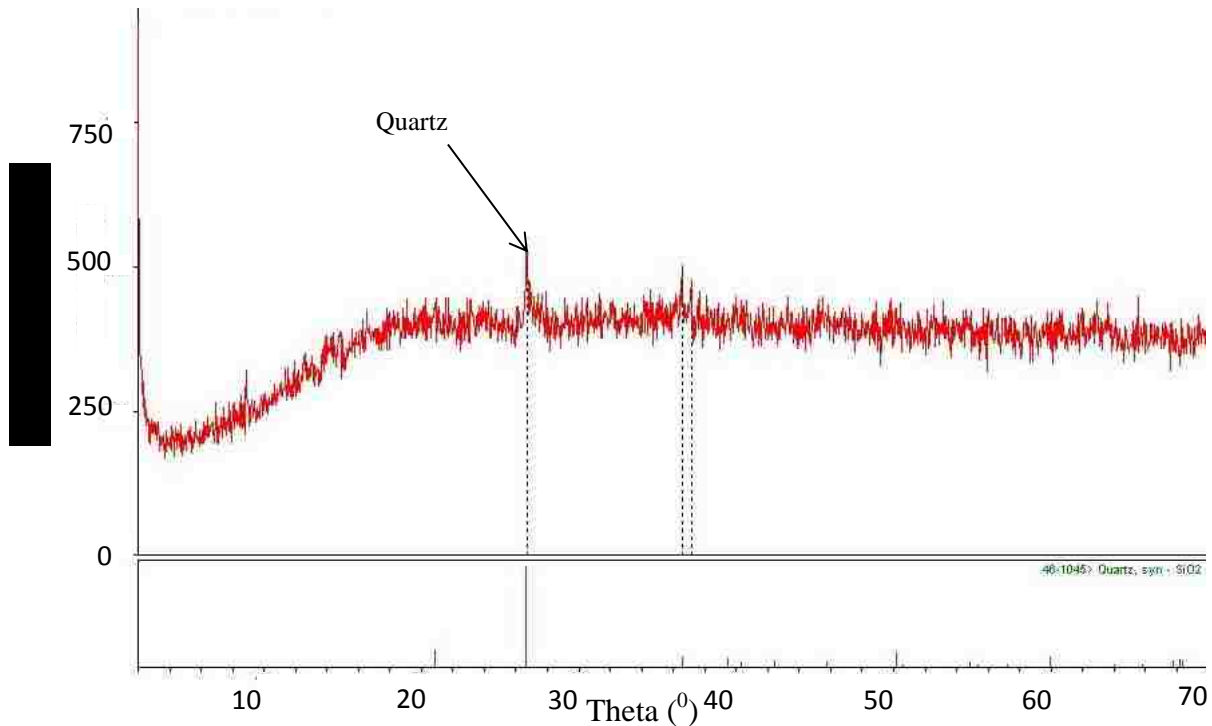


Figure 4.7: X-ray diffractogram for bulk mineralogical analysis of precipitates obtained from CO₂-brine contacted shale samples' effluent after the three month experiment. It showed high pitch noise indication large amorphous content in the precipitates

4.3 Scanning Electron Microscopy (SEM) and Energy Dispersive Spectroscopy (EDS)

The surface imaging of the shale caprocks and the effluent's precipitate using SEM revealed the nature of the microscopic pores and the possible growth of new secondary features. This was combined with the average spot and areal EDS analysis (location shown by the red dotted points and lines) of the imaged surfaces. The EDS analysis was performed on the original shale caprock samples, the CO₂-brine contacted samples and the effluent precipitates. The results presented below showed the presence of Iron (Fe), Sodium (Na), Potassium (K), Silicon (Si), Carbon (C), Oxygen (O), Chromium (Cr), Manganese (Mn), Calcium (Ca), Magnesium (Mg) and Aluminum (Al). They are present in rock minerals capable of exchanging ions with carbonic acid. The relative ratio of the metals confirms that Calcium-based minerals (like anhydrite and carbonates) are susceptible to carbonic acid attack. The elemental concentration of Ca in samples

B and C were low as shown in figures 4.13 and 4.19. This is in addition to alkali metals (e.g Na and K) whose compounds are generally soluble in acidic or alkaline fluids. This implies that compounds of Na, K, Ca, Mg, Al and Mn which were identified in the shale caprock samples would be reactively soluble (with slow kinetics) in aqueous CO₂ with the possibility of re-precipitation to form new minerals. The ratio of the elements identified at the surface of the samples over the 3 months of CO₂-brine flooding showed mixed variations which could be partially attributed to mineral dissolution/precipitation and sample heterogeneity.

Figure 4.8 represent the control specimen for sample A and it showed that there are fewer pore spaces in the CO₂-brine flooded sample (Figure 4.10) after 3 months. The pair figures (4.12 and 4.14) and (4.16 and 4.18) which are the control samples and CO₂-brine flooded samples for specimen B and C respectively suggest the opposite for the two other samples which are leaner in clay content. These SEM images for all the three samples showed that pore spaces in the shale caprock are of the sub-micron level as can be seen in figures 4.8, 4.10, 4.12, 4.14, 4.16 and 4.18.

Figure 4.20 shows the SEM image of the amorphous precipitate with no crystalline particle visible at the 1µm resolution. Figure 4.21 shows the elements that are preponderance in the effluents precipitate that XRD analysis indicated as amorphous in characteristics. Fe and Si are the two prominent mineral forming elements which confirm the presence of Quartz (SiO₂) and most-likely amorphous Iron Oxide that resulted from the oxidation of leached Fe²⁺ to Fe³⁺ giving the brown-like coloration of the effluent after exposure to the atmosphere over time.

Procedure for collection of rock samples for SEM/EDS analysis is documented in Appendix A. Multiple SEM and EDS analysis were used to examine the surface chemistry of the caprocks and the samples that were imaged are documented in Appendix D.

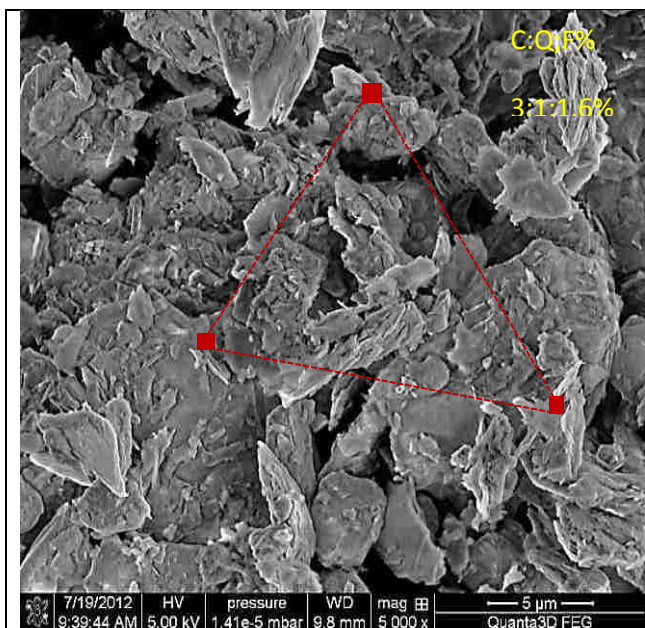


Figure 4.8: 5 μm resolution SEM image of control sample for specimen A showing mineral grains sizes of platelet structure and sub-micron pores at the site around EDS multi-spot analysis

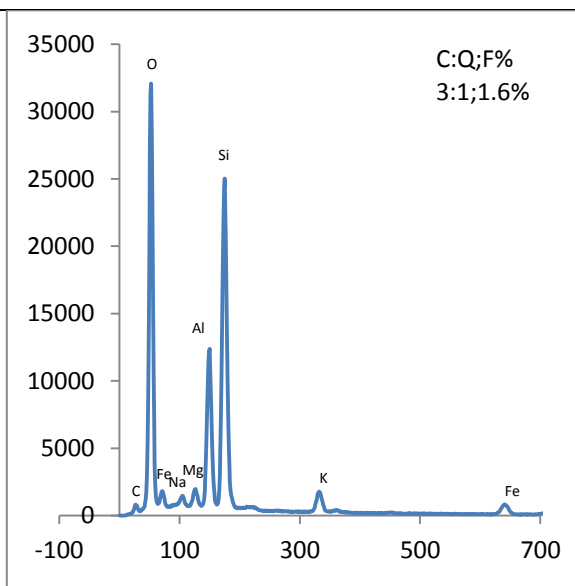


Figure 4.9: Average EDS plot of surface mineralogy of control sample for specimen A showing the relative elemental composition of multiple spots on the corresponding SEM image

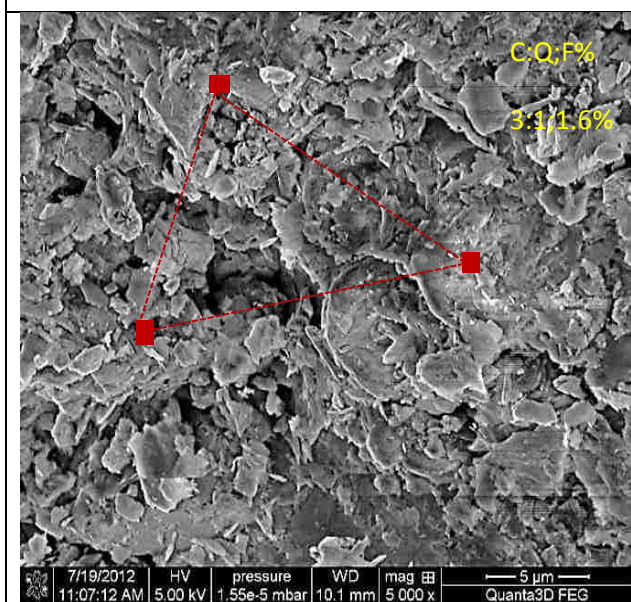


Figure 4.10: 5 μm resolution SEM image for specimen A showing mineral grains sizes of platelet structure and sub-micron pores at the site around EDS multi-spot analysis after 3 months of CO₂-brine flooding

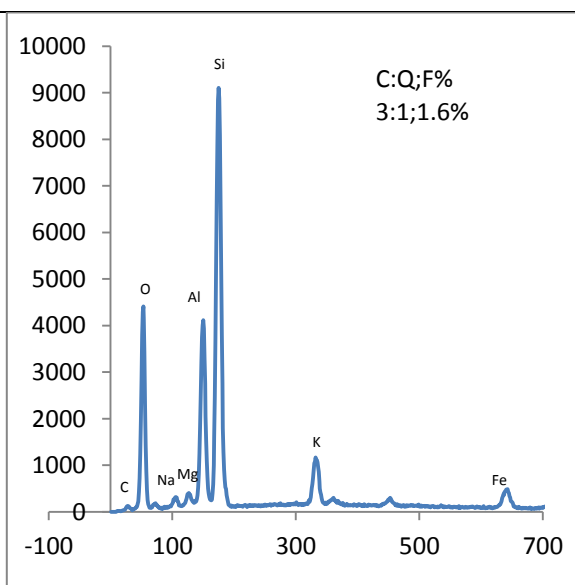


Figure 4.11: Average EDS plot of surface mineralogy for specimen A showing the relative elemental composition of multiple spots on the corresponding SEM image after 3 months of CO₂-brine flooding

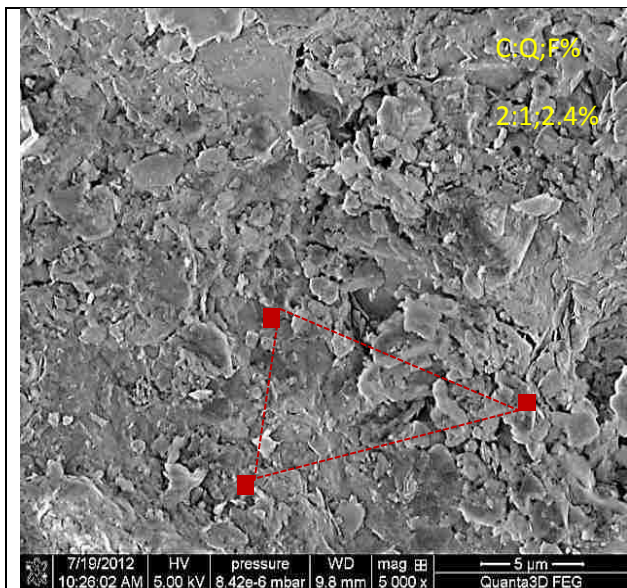


Figure 4.12: 5 μ m resolution SEM image of control sample for specimen B showing mineral grains sizes of platelet structure and sub-micron pores at the site around EDS multi-spot analysis

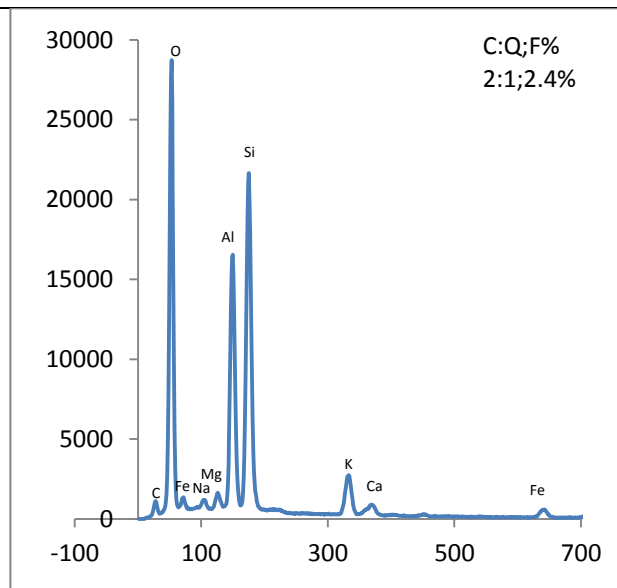


Figure 4.13: Average EDS plot of surface mineralogy of control sample for specimen B showing the relative elemental composition of multiple spots on the corresponding SEM image

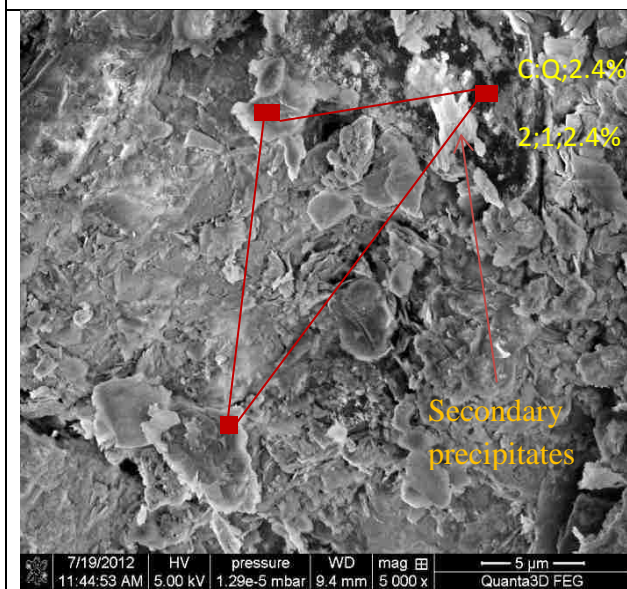


Figure 4.14: 5 μ m resolution SEM image for specimen B showing mineral grains sizes of platelet structure and sub-micron pores at the site around EDS multi-spot analysis after 3 months of CO₂-brine flooding

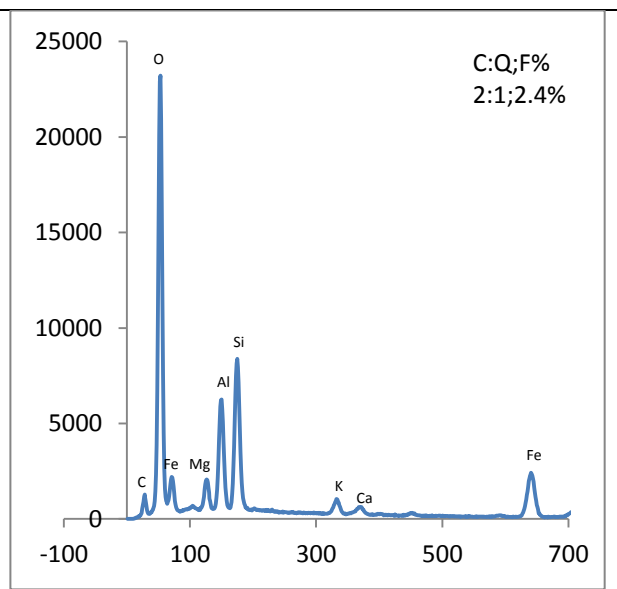


Figure 4.15: Average EDS plot of surface mineralogy for specimen B showing the relative elemental composition of multiple spots on the corresponding SEM image after 3 months of CO₂-brine flooding

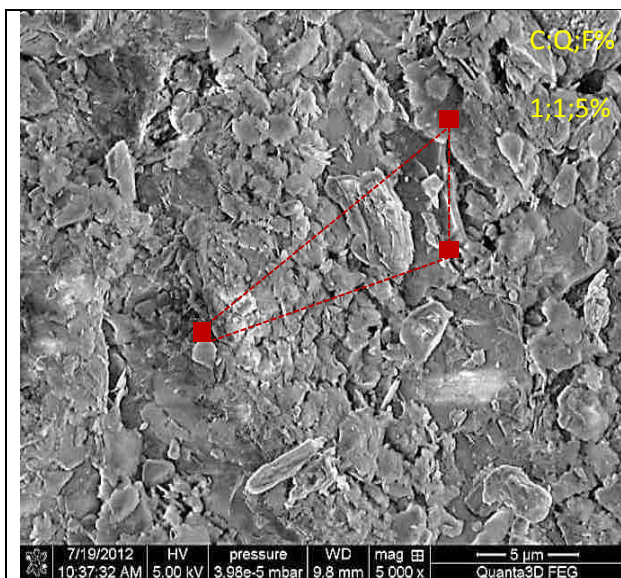


Figure 4.16: 5 μ m resolution SEM image of control sample for specimen C showing mineral grains sizes of platelet structure and sub-micron pores at the site around EDS multi-spot analysis

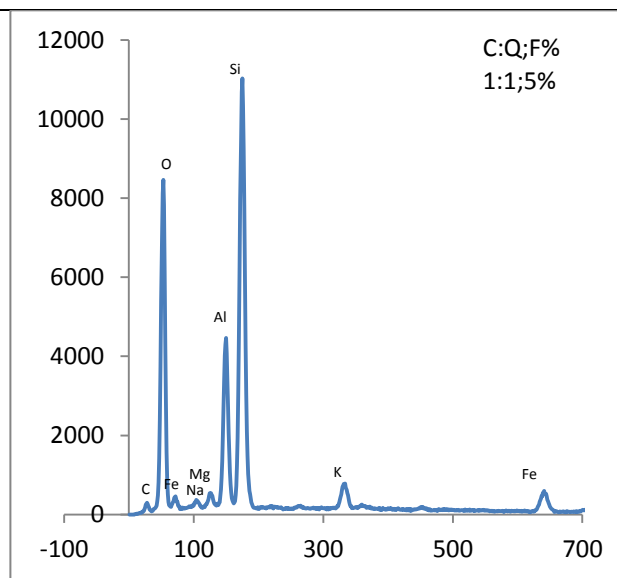


Figure 4.17: Average EDS plot of surface mineralogy of control sample for specimen C showing the relative elemental composition of multiple spots on the corresponding SEM image

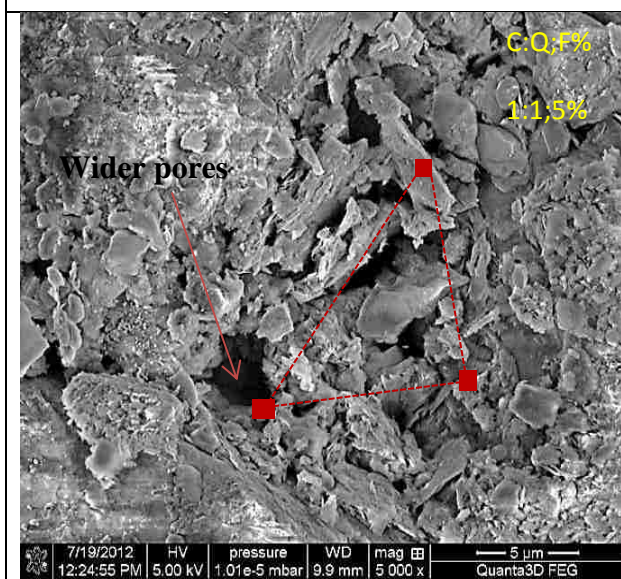


Figure 4.18: 5 μ m resolution SEM image for specimen C showing mineral grains sizes of platelet structure and sub-micron pores at the site around EDS multi-spot analysis after 3 months of CO₂-brine flooding

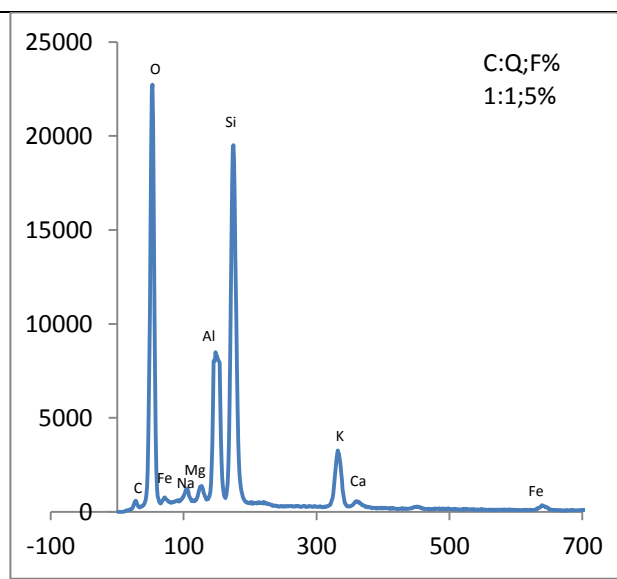


Figure 4.19: Average EDS plot of surface mineralogy for specimen C showing the relative elemental composition of multiple spots on the corresponding SEM image after 3 months of CO₂-brine flooding

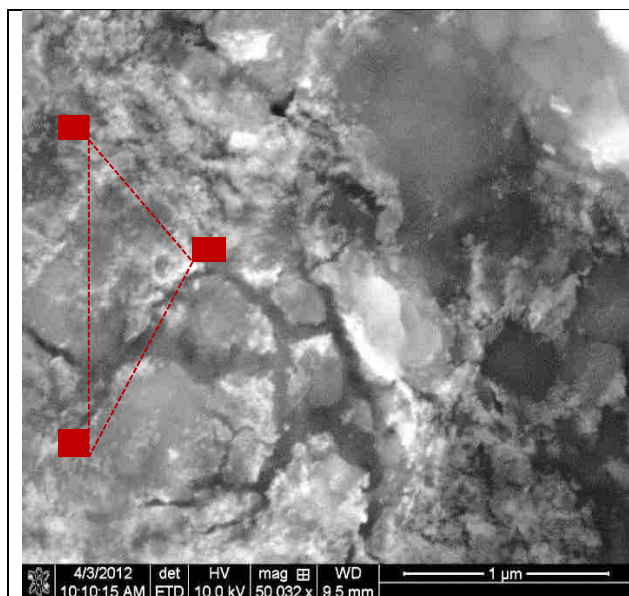


Figure 4.20: 1 μ m resolution SEM image of the effluent precipitate with no crystalline microstructure visible. The surface appears amorphous

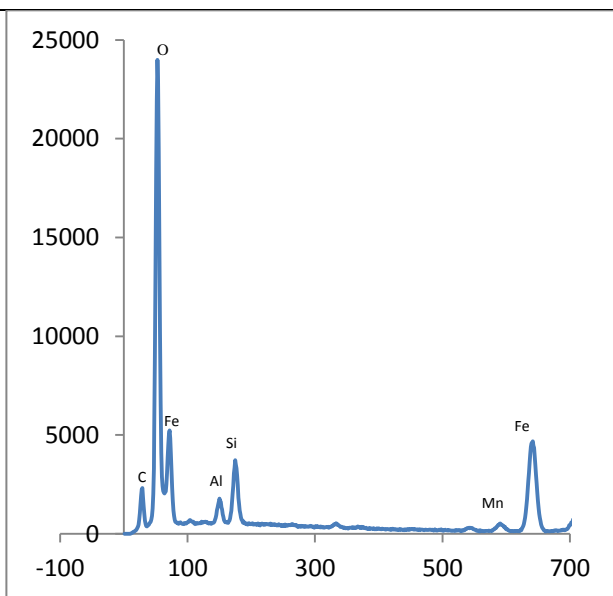


Figure 4.21: Average EDS plot of surface elemental mineralogy of effluent precipitate showing high Fe, O and Si concentration after 3 months of CO₂-brine flooding

The varying appearances of physical features (grain shape, size, depositional orientation, pores etc) suggest that active mineral alteration might have affected the microscopic structure of the shale caprock as seen from the SEM images above.

The tendency of the clay minerals present to swell is not significant as smectite and other montmorillonite that are responsible for clay swelling on contact with aqueous fluid were not identified in the bulk sample, hence no visible bridging of pore throat in all the images analyzed.

4.4 BET Nitrogen Adsorption Analysis

4.4.1 Pore Geometrical Properties in Bulk Shale Caprock

The Brunauer-Emmett-Teller (BET) Technique was used to obtain pore geometrical properties that can be affected by mineral dissolution/precipitation as a result of CO₂-brine geochemical interaction with shale caprock. These geometrical properties include specific

surface area, specific pore volume and pore sizes. Surface area and pore volume are estimated per gram of sample and hence the “specific” prefixes for the two parameters. Data points were based on measurements carried out on brine re-saturated samples and the three CO₂-brine contacted samples, giving four data points each per sample. These pore geometrical parameters and the noticeable changes in them are fully discussed in the next sections of this chapter. All BET data points presented graphically in this thesis are documented in Appendix E.

i) Bulk Specific Surface Area

The bulk specific surface areas (in m²/g) for the three shale caprock samples are shown in figure 4.22. There is a tendency for the surface area to increase as CO₂-brine flooding continues over the 3-month experimental period. There appears to be a slowdown in the increases particularly between the 2nd and the 3rd months. However Sample C showed a distinctly different feature as there was an initial decrease in the bulk surface area in 1st month of the experiment which may reflect some form of mineral precipitation reducing the available surfaces for adsorption. Mineral dissolution seems to be the cause of surface area increases that dominated over the three month period as reflected in the ICP-OES analysis. Also the starting point of each sample showed that rocks with the highest percentage of clay had the highest specific surface area and vice versa. It is an indication that these shale rocks with high clay content may have few and tighter connected pores, the surface area available for reactive flow is significantly high.

ii) Bulk Specific Pore Volume

The specific pore volume (in cc/g) showed similar trend as in the surface area. It is a measure of the connected pore volume available within the samples that may be affected by

geochemical changes. Figure 4.23 depicts the approximate changes in pore volume of the rock samples with slight increases in value over the three month experimental period. The initial decrease in pore volume for sample C was less prominent in slope compared to the specific surface area.

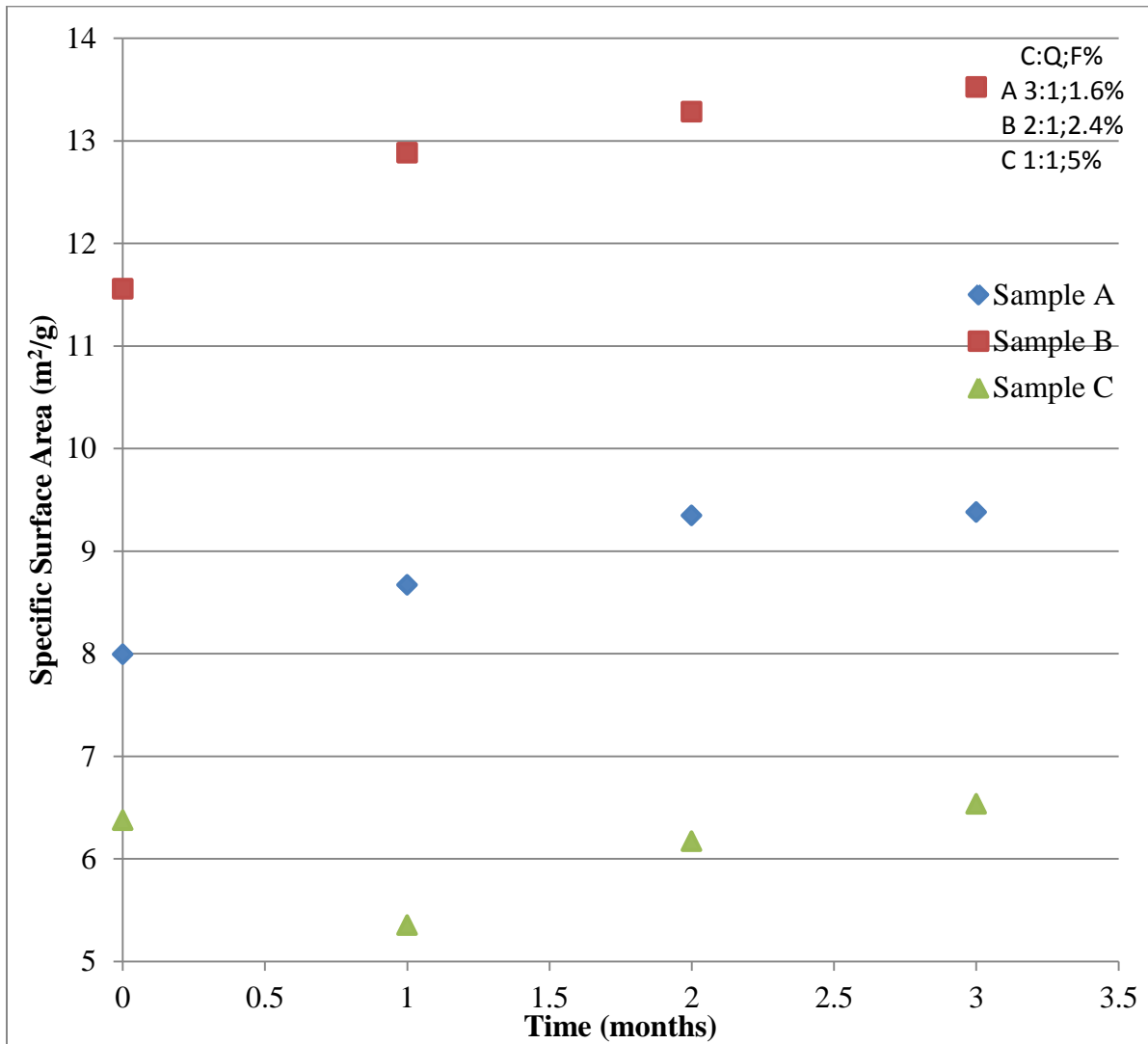


Figure 4.22: Bulk specific surface area of the shale caprock samples over 3 months of CO₂-brine flooding depicting an overall increase in measured surface area available for adsorption with the exception of sample C that initially decreased after the first month of flooding

Sample C which has the lowest clay content reflected the lowest pore volume both at the initial value and throughout the measured values of the CO₂-brine contacted samples. The results

suggest small but noticeable changes in overall pore volumes that may impact both permeability and storage spaces that are available for CO₂. A reduction in the rate of pore volume increases can be seen in all the three samples between the 2nd and 3rd months suggesting lowered geochemical reactivity.

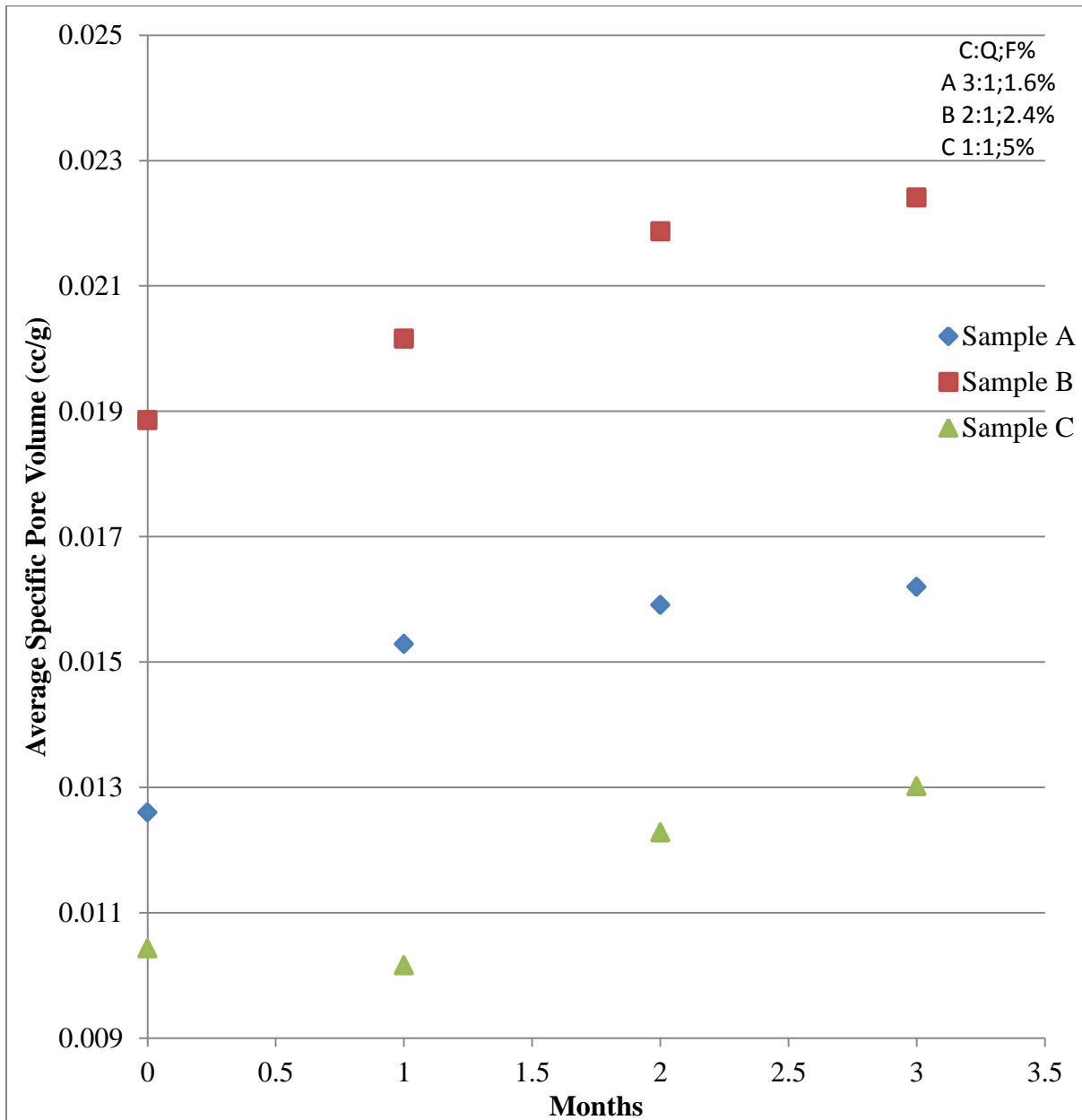


Figure 4.23: Bulk specific pore volume of the shale caprock samples over the 3 months of CO₂-brine flooding depicting an overall increase in measured pore volume available for adsorption with the exception of sample C that initially decreased after the first month of flooding

iii) Bulk Average Pore Size

The bulk average pore size (in nm) shown in figure 4.24 reflects an opposite trend to that of the specific surface area and pore volume. Sample C seems to have the highest pore size on the average, with sample B having the lowest and Sample A maintaining the middle position. There appears to be no correlation between the pore size and the other two pore geometrical properties discussed above. Also the data points for the pore size trend appear to be haphazard over time.

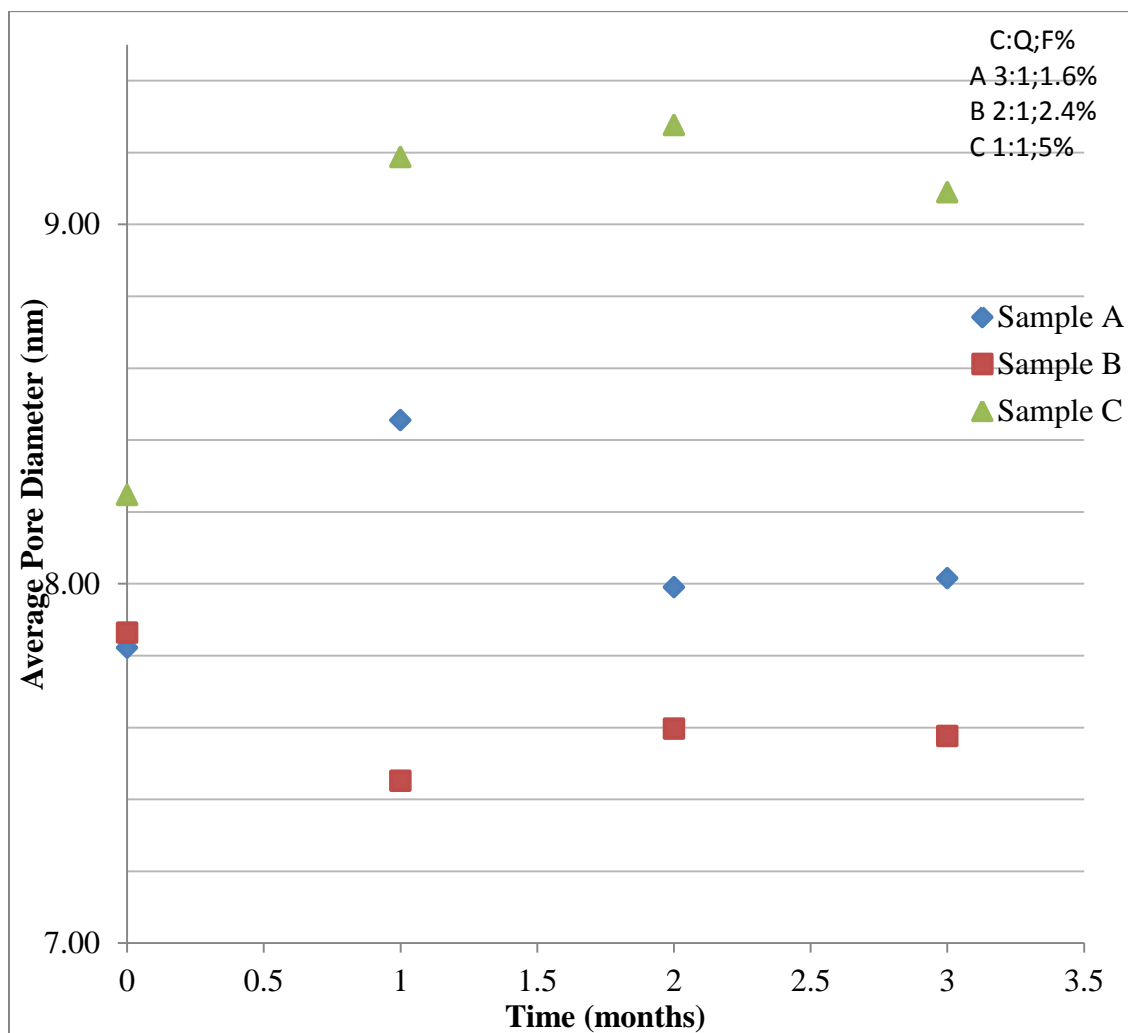


Figure 4.24: Bulk average pore sizes of the shale caprock samples over the 3 months of CO₂-brine flooding. It shows haphazard changes that indicated sample B has the lowest average pore size magnitude in contrast to observed specific surface area and pore volume evolution trend

It is an evidence of the undefined geometrical shape of the pore spaces whose connectivity is heavily influenced by pore sizes. It is also an indication of the inherent heterogeneity that may be present in the rocks. However, it is clear that the pore sizes are changing and these can impact capillary entry pressure into the shale caprock.

iv) Bulk Modal Pore Size

The bulk modal pore sizes (in nm) refer to the highest occurring pore diameters in the shale rock samples .Figure 4.25 shows that sample B has the lowest values of modal pore diameters while

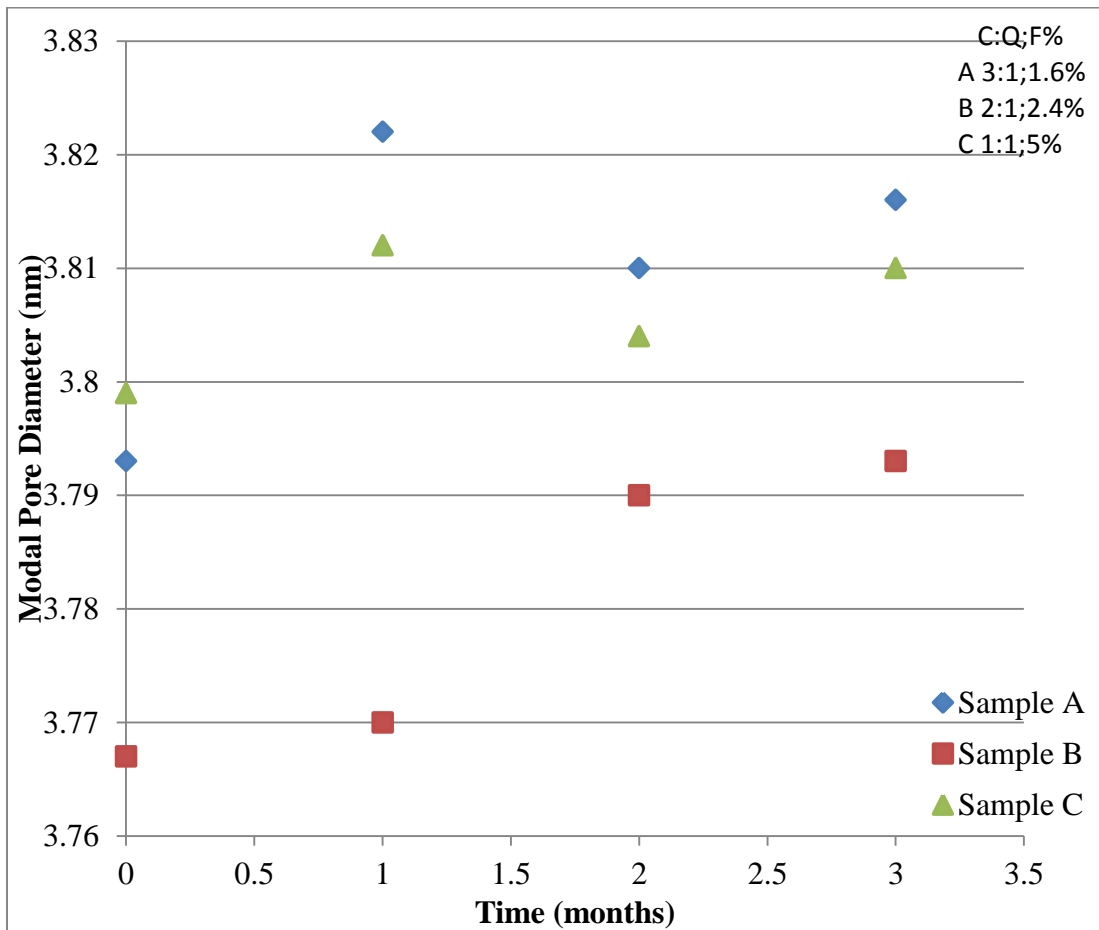


Figure 4.25: Bulk modal pore sizes for the shale caprock samples over the 3 months of CO₂-brine flooding. It shows haphazard changes that indicated sample B has the lowest modal pore size magnitude in contrast to observed specific surface area and pore volume evolution trend

samples A and C tend to follow the same trend in the changes that are noticeable over the experimental period. This is in contrast to the average pore diameter values and these modal pore sizes are expected to produce the most significant changes that can be noticed as indicated by the pore size distribution data.

4.4.2 Pore Size Distribution

This section highlights the results from pore size distribution data measurements obtained from running 40-point adsorption experiments that lasted for an average of 8 hours to 11 hours per sample. Figures 4.26 to 4.40 present the results of the measurements. Bulk pore size distribution, cumulative specific surface area and cumulative specific pore volume are examined with respect to the pore sizes making significant fractional contributions to these parameters.

i) Bulk Pore Size Distribution

This entails the measurement of the variations in pore sizes and pore volume for all the 3 samples over the experimental period. It is a plot of pore diameter (nm) versus pore volume (cc/nm/g). It reflects the individual contributions of the pore sizes to the bulk pore volume of the rock samples and the changes in those contributions are presented below.

1) Sample A

The changes in the pore size distribution for sample A were concentrated at four major points on the plot as indicated in figure 4.26. Point 1 shows a net increase in the pore volume for the same pore diameter range while point 2 reflects a modest increase in pore volume at the modal diameter. Point 3 shows a net decrease in pore volume but later gave way to an increase over the few but more significant pore sizes at the extreme right of the plot. This trend probably

contributed to the overall increases in the pore geometrical parameters of the bulk samples. The bulk of the pore volume in this sample is in the pore diameter range 1.5nm – 30nm.

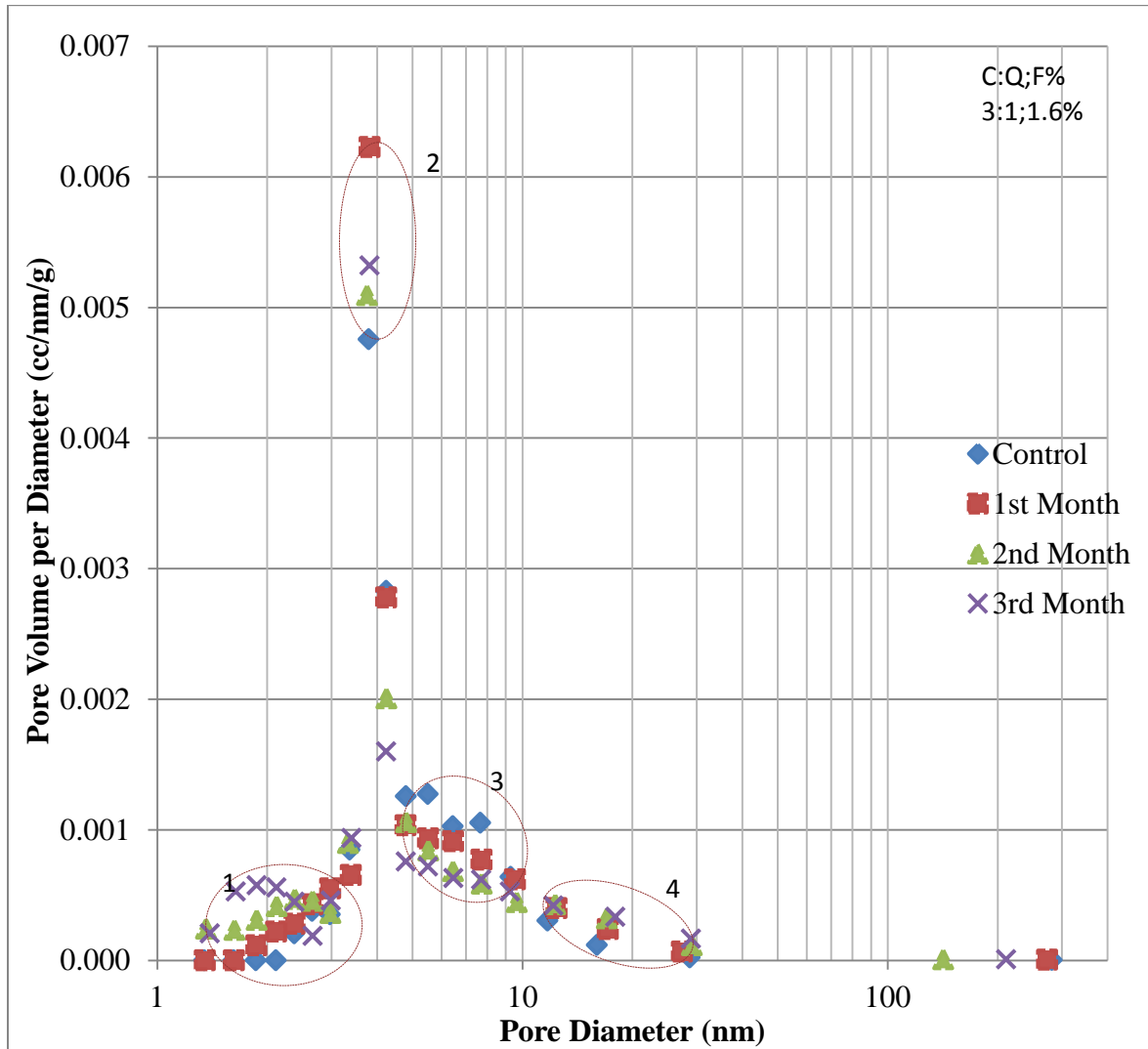


Figure 4.26: Pore size distribution for sample A over the 3 month experimental period of shale caprock/CO₂-brine flooding. It shows four regions of changes in specific pore volume with only region 3 having a net decrease in pore volume by the end of the third month of experiment

2) Sample B

The pore size distribution for sample B, shown in figure 4.27, reflects major pore volume changes at three points (the 4th point is not as clear, as all the data points appear close). Points 1 shows an increase in pore volume for the range of pore sizes considered while points 2 and 3

reflects a net decrease in pore volume for the modal diameter and the pore size range considered respectively. The distribution suggests that the bulk of the pore volume in this shale caprock resides in the pore size range 1.5nm to 30nm.

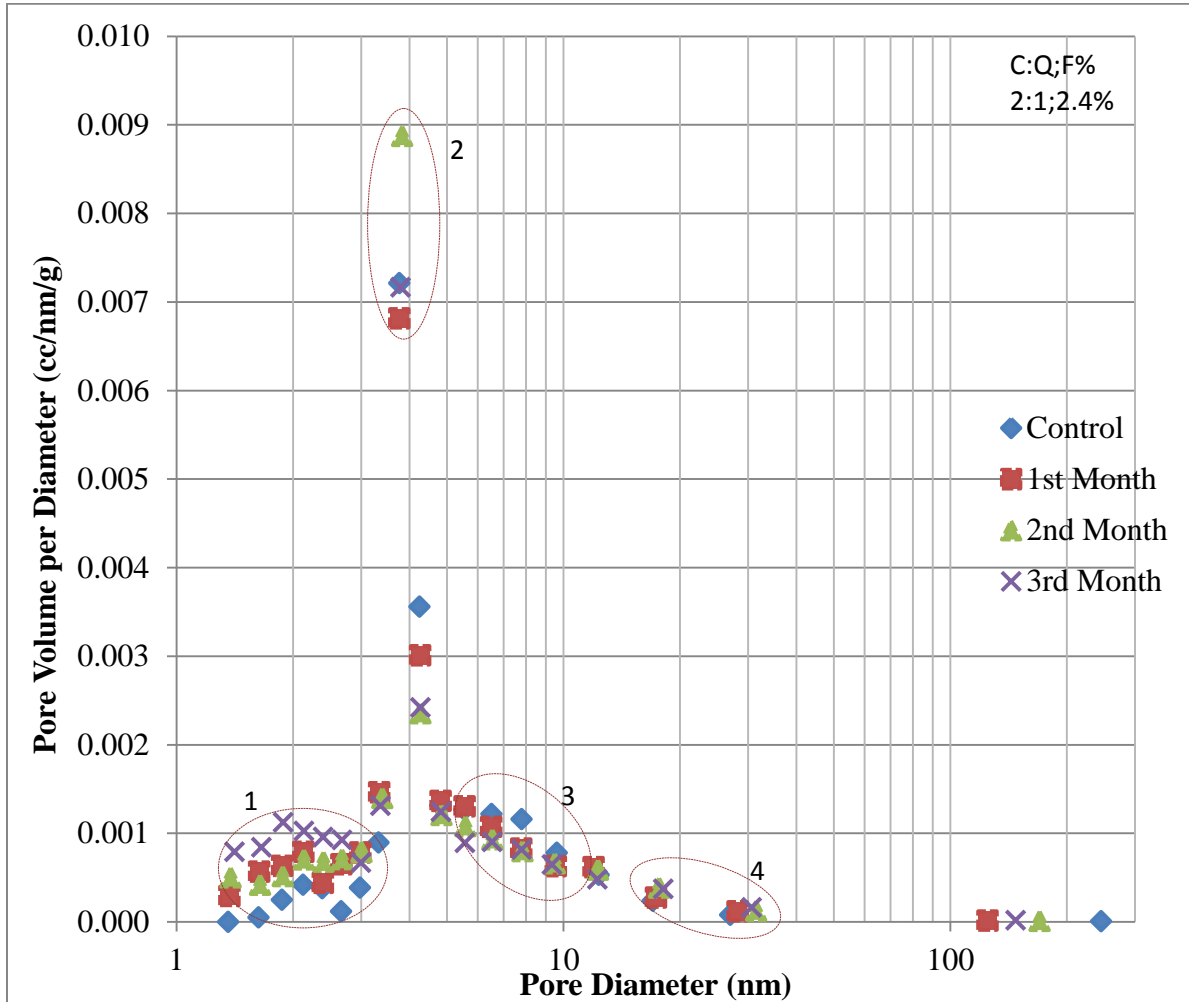


Figure 4.27: Pore size distribution for sample B over the 3 month experimental period of shale caprock/CO₂-brine flooding. It shows four regions of changes in specific pore volume with only region 3 having a net decrease in pore volume by the end of the third month of experiment

3) Sample C

Sample C has three major points on the pore size distribution reflecting changes. Point 1 on figure 4.28 shows a net increase in pore volume while points 2 and 3 showed significant decreases in the pore volume for the range of pore diameters considered. Point 4 reflects a less

significant increase in the pore volume for the range considered. The bulk of the pore volume is concentrated in the pore diameter range 1.5nm – 30nm.

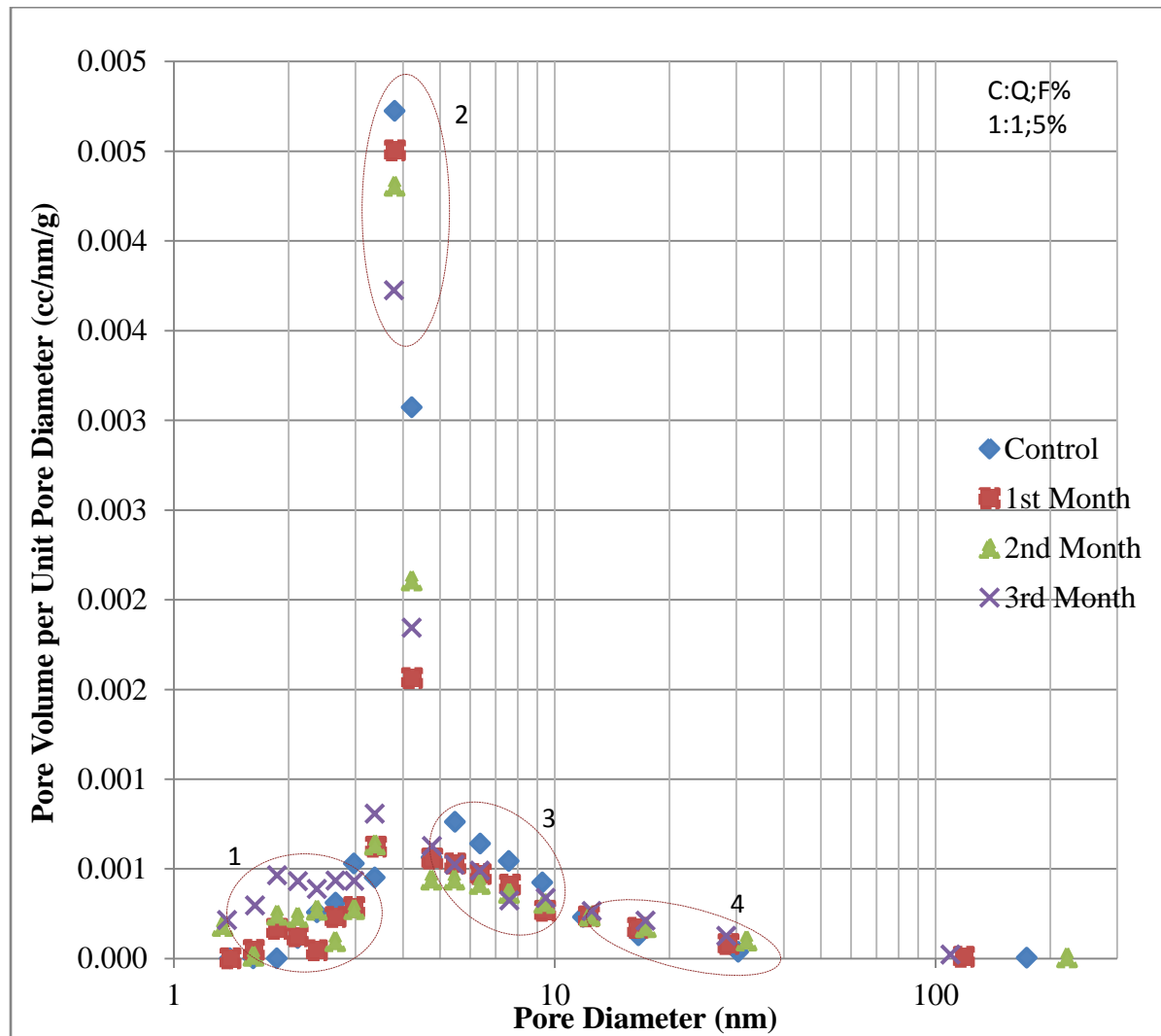


Figure 4.28: Pore size distribution for sample A over the 3 month experimental period of shale caprock/CO₂-brine flooding. It shows four regions of changes in specific pore volume with no region having a net decrease in pore volume by the end of the third month of experiment

ii) Cumulative Specific Surface Area and Pore Volume

This represents the cumulative contribution of measured pore sizes to the bulk specific surface area and pore volume of the shale rock over the 3-month experimental period. These plots were divided into two sections; less than 5.5nm and greater than 5.5nm (pore size) plots.

This afforded the opportunity to examine the cumulative impacts of CO₂ reactive flow through the rock pore spaces as observed in the bulk pore size distribution for the experimental samples.

a) Cumulative Specific Surface Area of Pore Sizes Less Than 5.5nm

1) Sample A

The cumulative specific surface area for sample A as shown in figure 4.29 reflects an elongated S-shaped changes in the cumulative specific surface area for the shale rock. The changes are prominent at the lower pore diameters of between 1.5nm to 3.5nm which later thinned out to the original value measured at approximately 5.5nm pore size.

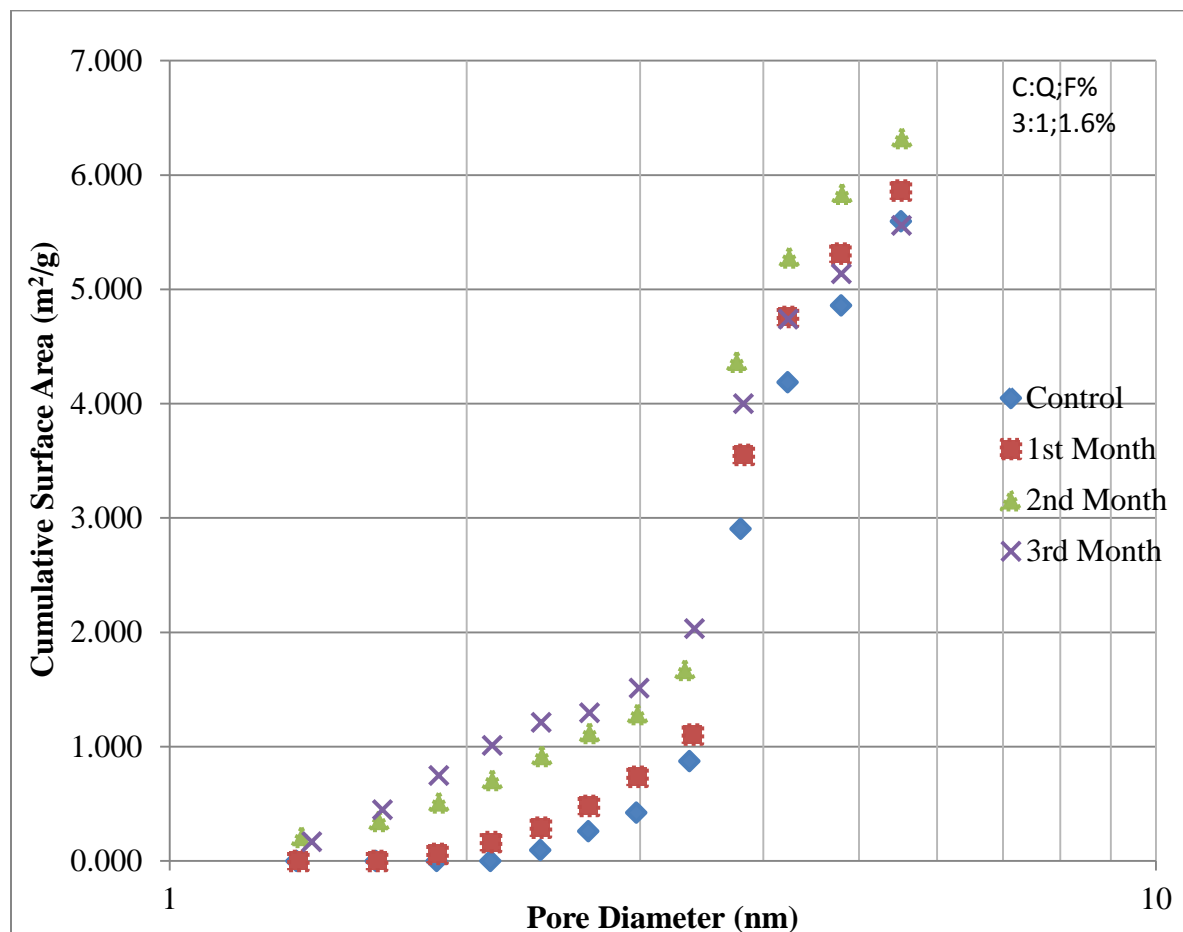


Figure 4.29: Cumulative specific surface area for sample A with less than 5.5nm pores over the 3 months of CO₂-brine flooding. It shows that significant surface area changes occur in pore sizes that are less than 3.5nm with the surface area converging back to the control sample initial value

These observations suggest a widening of available surface area for CO₂-rock interaction and can also be construed as an increase in pore space that may be available for CO₂ storage. The shape of the curve indicates a possibility of change prediction modeling for the cumulative specific surface area in CO₂-brine/shale caprock interaction.

2) Sample B

The cumulative specific surface area for sample B, shown in figure 4.30, followed the elongated S-shape of sample A albeit with an open end. The increases in this cumulative

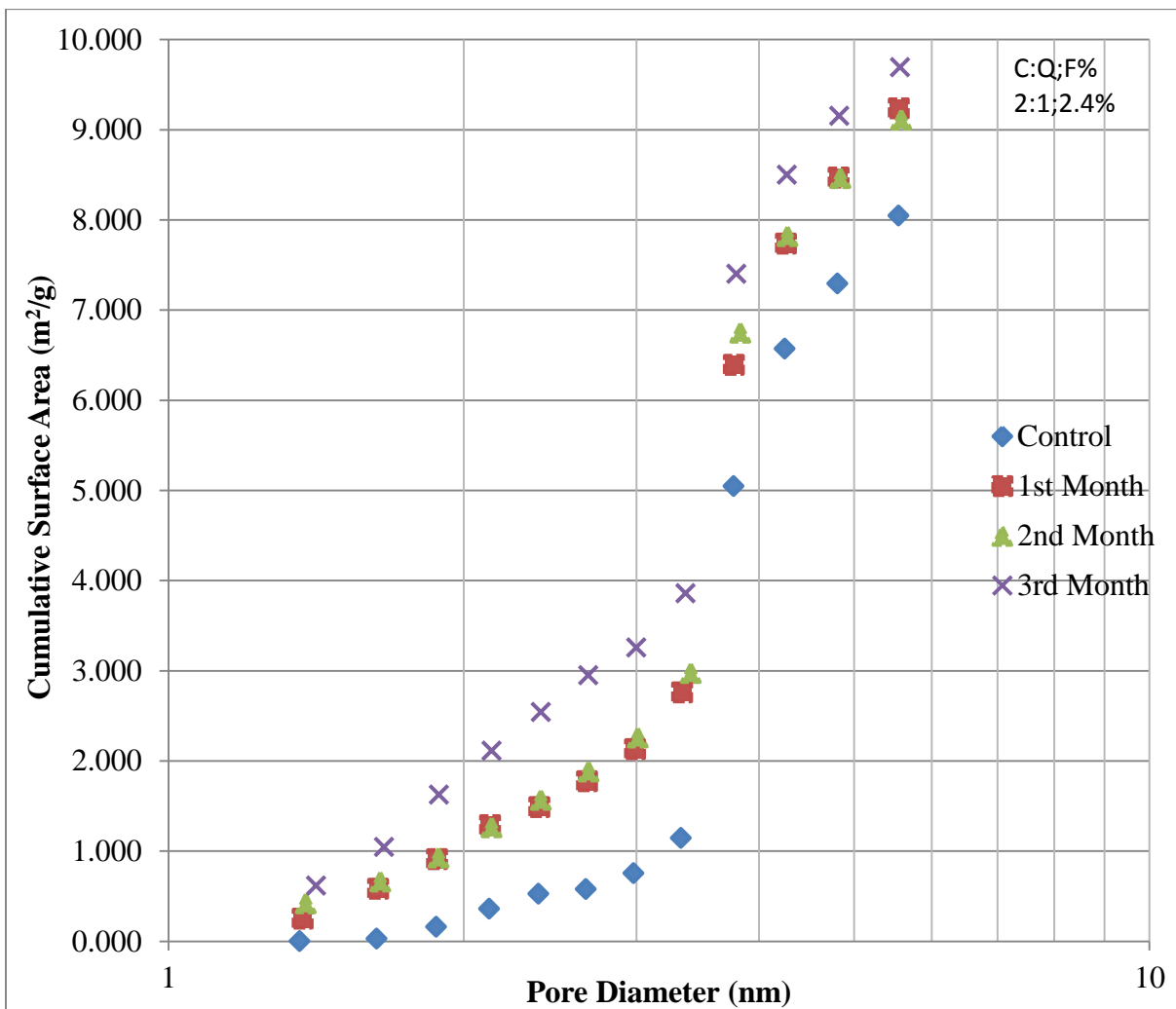


Figure 4.30: Cumulative specific surface area for sample B with less than 5.5nm pores over the 3 months of CO₂-brine flooding. It shows that significant surface area changes occur in pore sizes that are less than 3.5nm with net overall increase at the end of the third month

parameter were unchanged in the first two months but it finally increased almost by the proportion it increased in the first month. The increases for the pore sizes between 1.5nm and 3.5nm were much larger than pores sizes between 4nm and 5.5nm. The plot showed the path of surface area widening with respect to pore sizes in shale rocks when in contact with CO₂-brine.

3) Sample C

Figure 4.31 showed the changes in cumulative specific surface area for the shale caprock over the 3 month experimental period. The elongated S-shape as in samples A and B are also

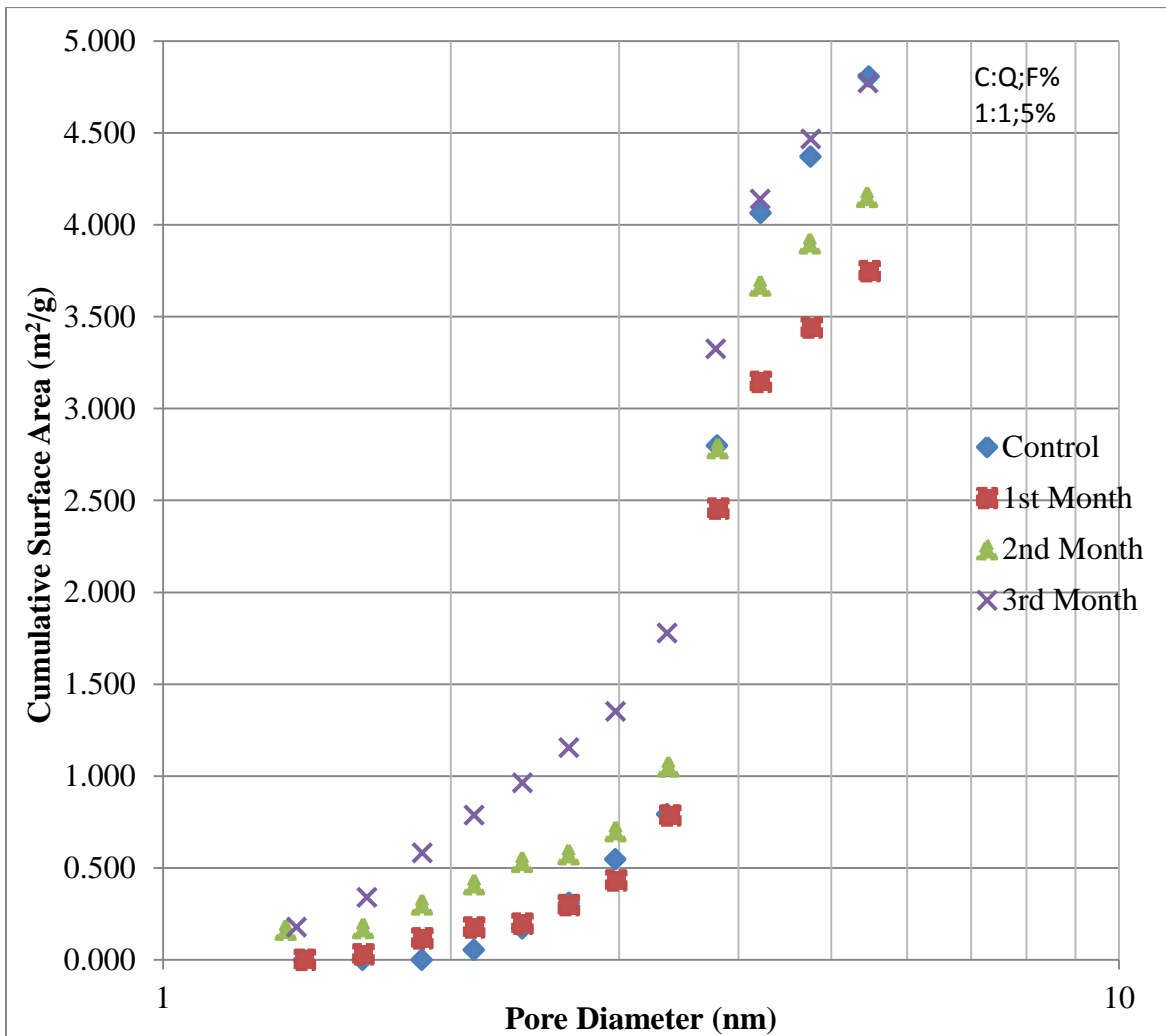


Figure 4.31: Cumulative specific surface area for sample C with less than 5.5nm pores over the 3 months of CO₂-brine flooding. It shows that significant surface area changes occur in pore sizes that are less than 3.5nm with net overall increase at the end of the third month

noticed albeit thinner in size with the upper end closing at the control and 3-month samples. The changes in cumulative specific surface area are dominated by pore sizes ranging between 1.5nm and 3.5nm. The rock recovered much of the cumulative surface area lost between the 1st and 2nd month in the range 4nm to 5.5nm. This was the only sample where there is a noticeable initial reduction in cumulative surface area between 4nm and 5.5nm pore sizes.

b) Cumulative Specific Pore Volume for Pore Sizes Less Than 5.5nm

1) Sample A

The elongated S-shape noticed in the cumulative surface area is visible in the cumulative pore volume as well albeit with a crossing over of the control sample and the 3rd month sample lines at the upper tip of the curves. Initial increases in the cumulative pore volume of sample A thinned out at the 3.5nm pore size and eventually decreased at pore sizes greater than 4nm as shown in Figure 4. 32.

The tendency of pore volumes near the middle band of 5.5nm pore size to be fairly unchanged suggests that geochemical changes might eventually cause some constriction of pore spaces depending on whether dissolution or precipitation processes are controlling. It can also be noted that the magnitude of cumulative pore volume changes is lower than the cumulative surface area for the same pore size range over the 3 months experimental period.

2) Sample B

Figure 4.33 showed the cumulative pore volume plot for sample B. The elongated S-shape revealed a larger volume change for the 1.5nm – 3.5nm range with a thin trunk at the middle. This is another confirmation that smaller pore sizes in the range 1.5nm – 3.5nm are most-likely more susceptible to changes in both their associated pore volumes and surface areas. This may be due to longer residence time for fluid flowing through these tighter pores, allowing stronger and

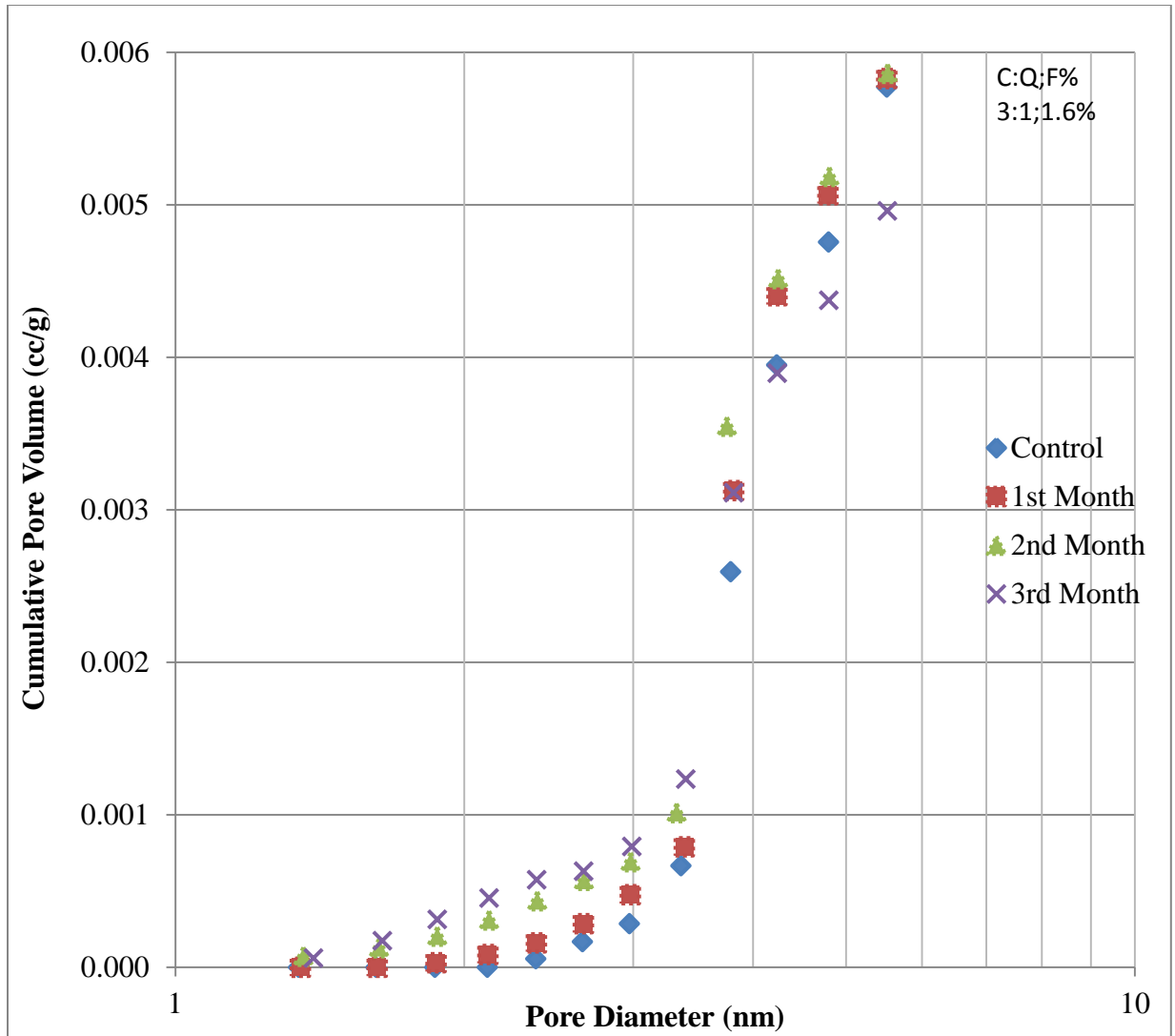


Figure 4.32: Cumulative specific pore volume for sample A with less than 5.5nm pores over the 3 months of CO₂-brine flooding. It shows that modest pore volume changes occur in pore sizes that are less than 3.5nm with net overall increase at the end of the third month

more complete reactive transport of CO₂ into the rock minerals. Subsequent and previous evidences support this proposition. For the 4.5nm to 5.5nm pores sizes in sample B, the changes in cumulative pore volume are not significant for the 3 months under which the rock samples were contacted with CO₂-brine, unlike it was in the cumulative surface area changes for the same range of pore sizes. The middle section of the S-shaped and elongated chart shows that pore geometrical properties are not changing much and this region corresponds to the modal pore

diameter range. This may suggest that equal but opposite amount of pore spaces at the lower and the upper end of the middle of the chart are changing such that the net effect is significantly reduced with respect to cumulative surface areas and pore volumes.

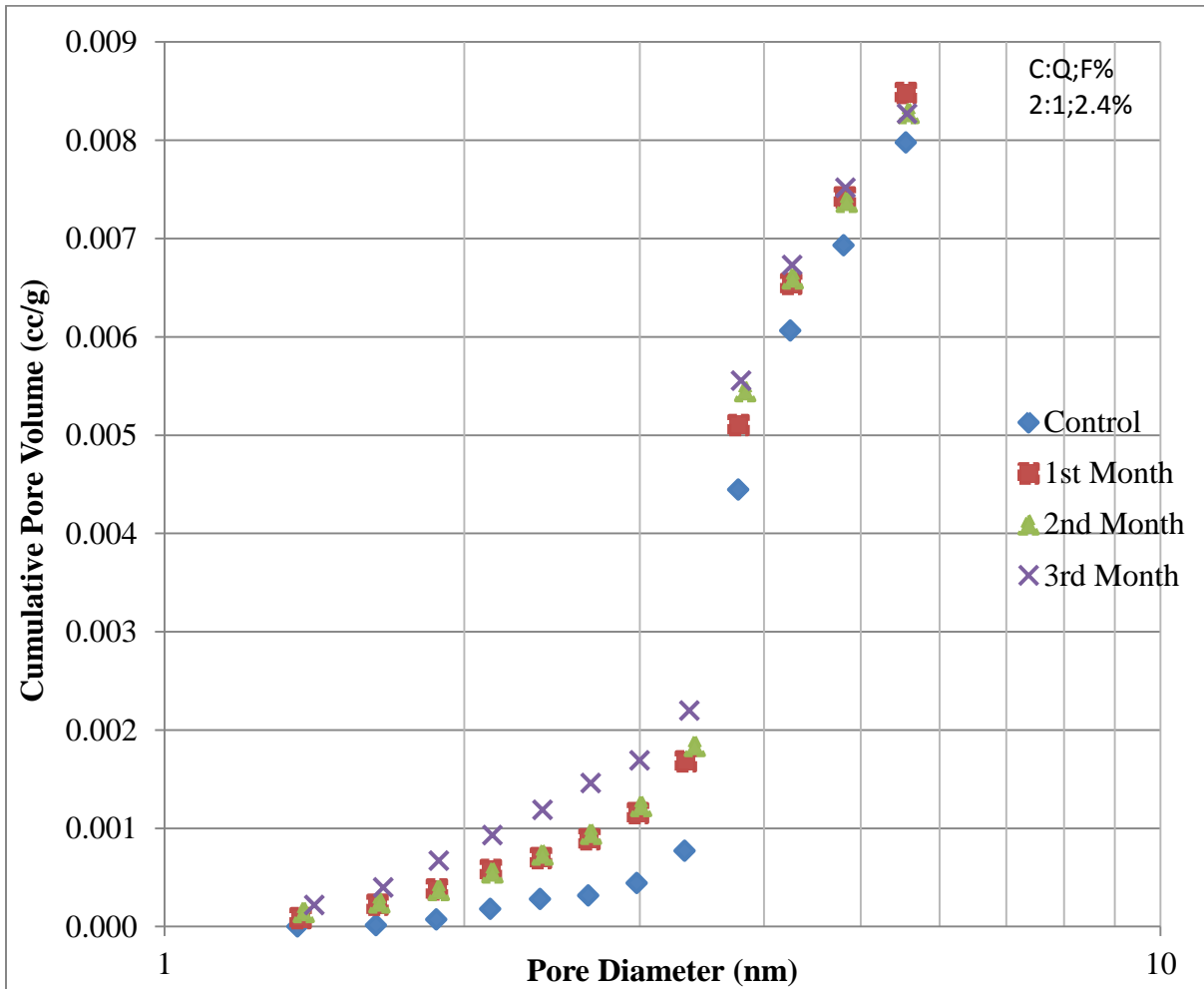


Figure 4.33: Cumulative pore volume for sample B with less than 5.5nm pores over the 3 months of CO₂-brine flooding. It shows that modest pore volume changes occur in pore sizes that are less than 3.5nm with net overall increase at the end of the third month

3) Sample C

Figure 4.34 shows the changes in the cumulative pore volume for sample C with initial overall decreases in the cumulative values in the first two months before increasing back to the initial values. Though the 4nm to 5.5nm range showed some decrease in the 3rd month. This represents a reduction in the volume that is available in the rock to hold fluids and it may be due

to a greater effect of precipitation than dissolution. In addition, the distinct S-shape of the curves like previous cumulative properties of pore volume and surface area can be observed on the graph. There is a slight difference in the behavior of cumulative pore volume and surface area for sample C alluding to the fact that changes in the pore volume and surface area of the rock nanopores do not follow exactly the same path though they have similar shape of plot lines.

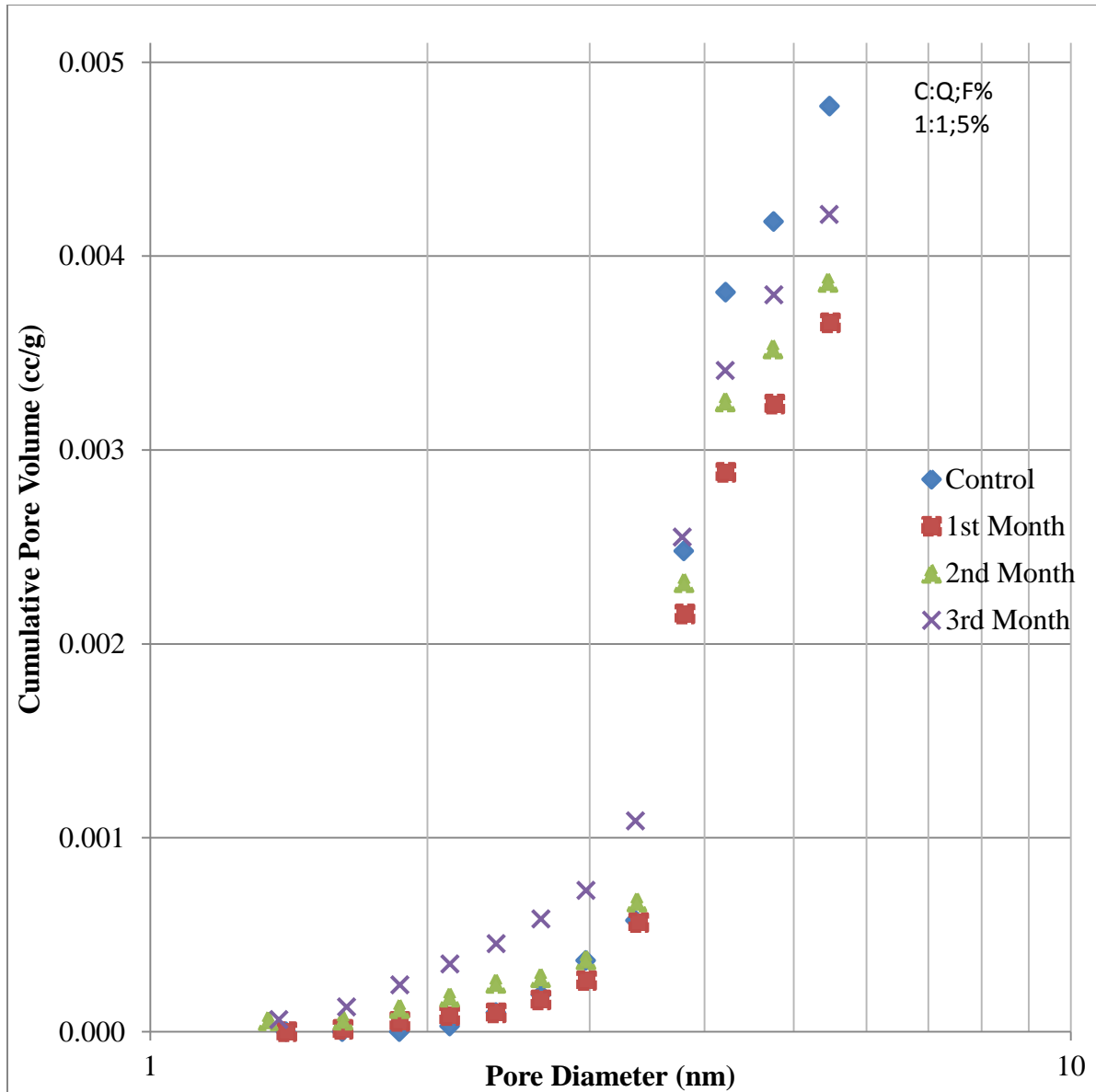


Figure 4.34: Cumulative pore volume for sample C with less than 5.5nm pores over the 3 months of CO₂-brine flooding. It shows that modest pore volume changes occur in pore sizes that are less than 3.5nm with net overall increase at the end of the third month

c) Specific Surface Area of Pore Sizes Greater Than 5.5nm

1) Sample A

The cumulative specific surface area of pores that are greater than 5nm for sample A as shown in figure 4.35 reflects an exponential curve changes in the cumulative specific surface area for the shale. These changes are concentrated at the higher pore diameters between 35nm and 300nm, plateauing out from the 25nm pore size such that their lines are eventually parallel to one another. Although the bulk of the surface area still resides in the less than 30nm pores.

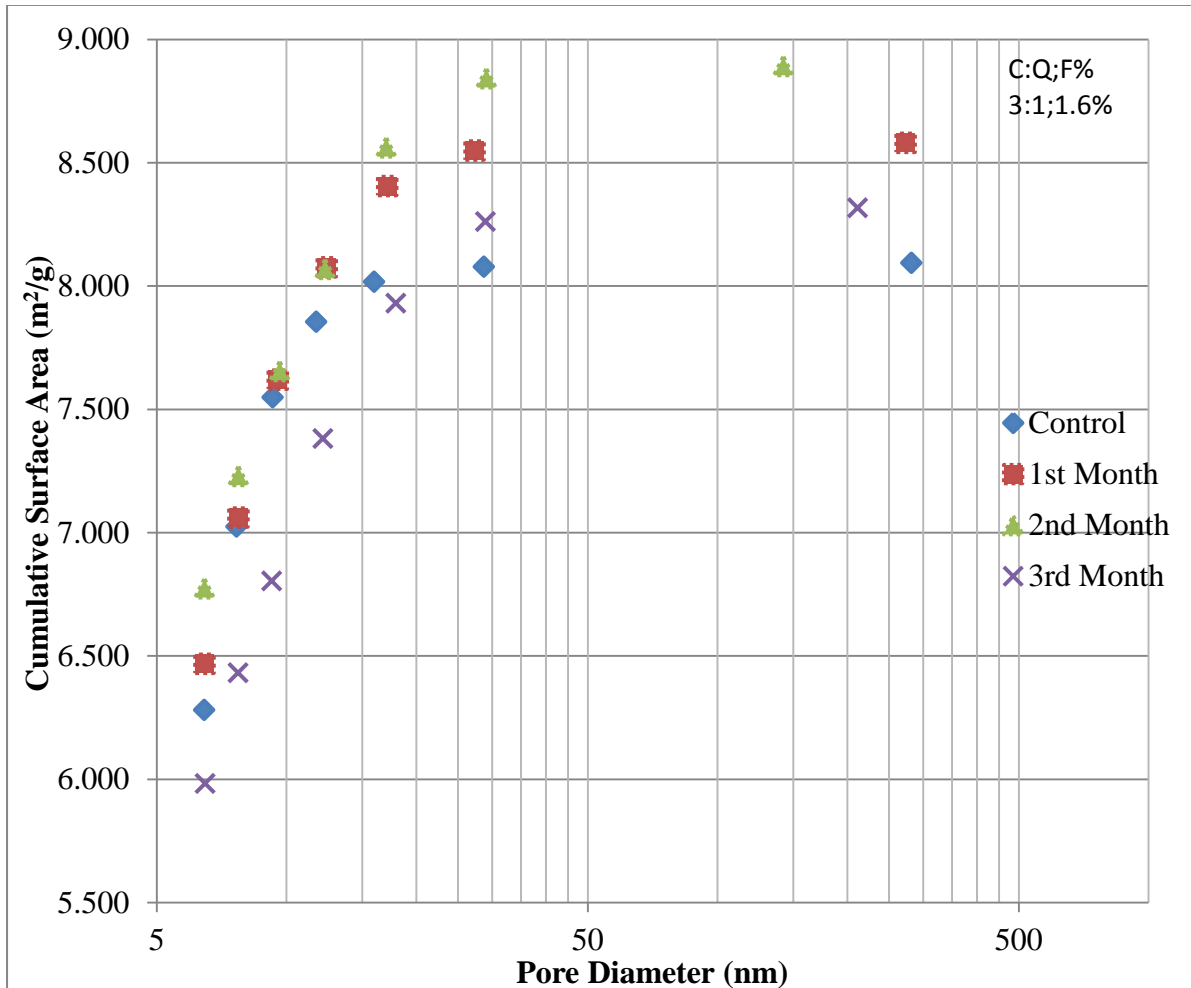


Figure 4.35: Cumulative specific surface area for sample A with greater than 5.5nm pores over the 3 months of CO₂-brine flooding. It shows a modest net increase in surface area at the end of the 3rd month

These observations suggest that the most significant changes are taking place within pores that are less than 30nm as a result of CO₂-rock interaction and can also be construed as an increase in pore volumes that may be available for CO₂ storage. The exponential shape of the curve indicates petrophysical change prediction for the cumulative specific surface area in CO₂-shale caprock interaction. While there is an overall decrease in specific surface area for the lower band of pore sizes that are less than 30nm in the figure, there is still a modest surface area increase for pore sizes that are greater than 30nm over the 3 month experimental period.

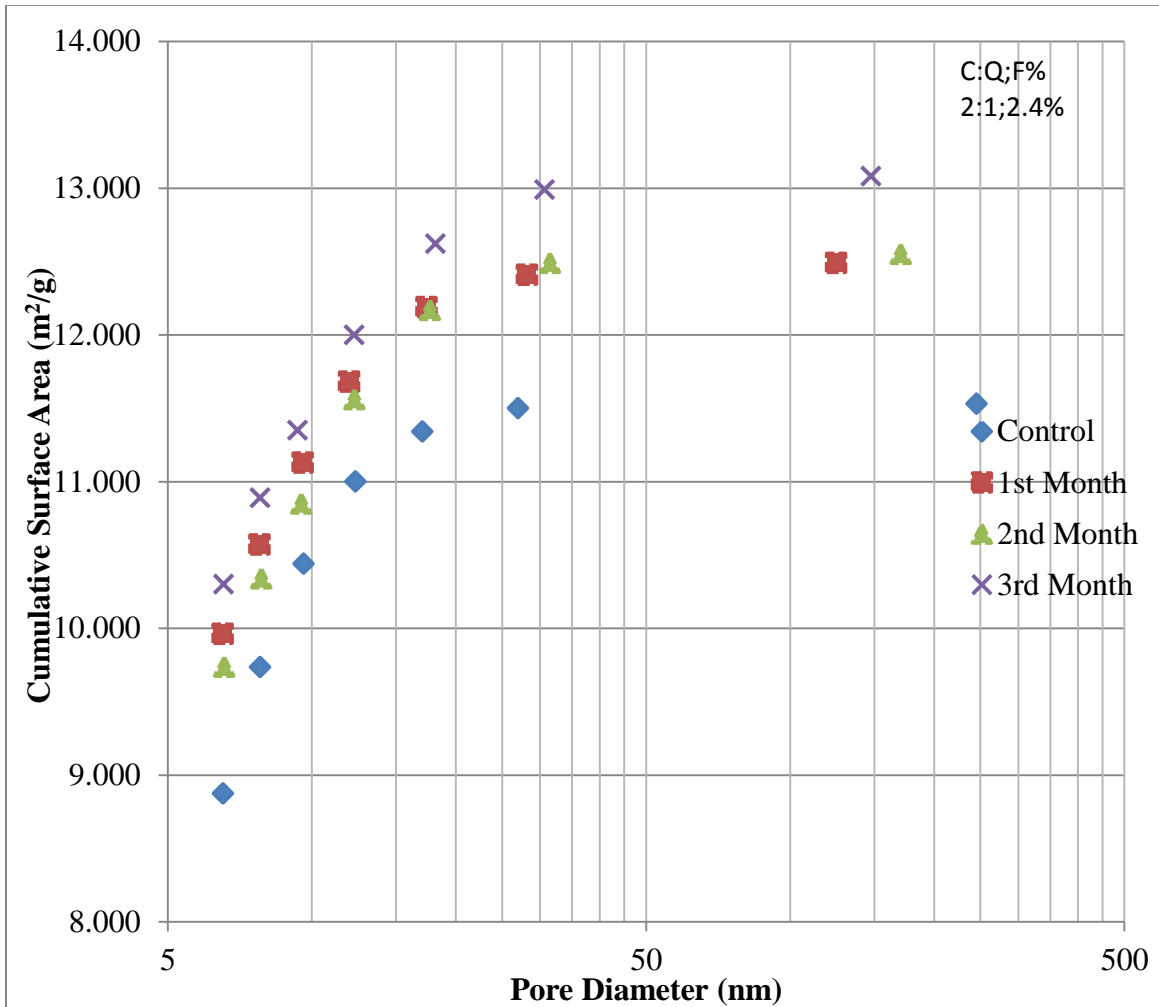


Figure 4.36: Cumulative specific surface area for sample B with greater than 5.5nm pores over the 3 months of CO₂-brine flooding. It shows a significant net increase in surface area at the end of the 3rd month

2) Sample B

In figure 4.36 above, the same exponential curve characterizes the cumulative surface area for pores that are greater than 5.5nm for sample B as it was in sample A. The change in magnitude of the cumulative surface area was more pronounced for pore sizes that are greater than 30nm compared to lesser pore sizes. There is a noticeable overall increase in surface area for this sample suggesting an increase in reactive flow effects. The near overlapping trend line for the 1st and 2nd month showed that the greatest change in the magnitude of the cumulative property occurred within the first two months of the experiment. The cumulative values for pores that are greater than 30nm also plateaued out over the course of the experiment lying parallel to one another as observed in sample A.

3) Sample C

Figure 4.37 presents the cumulative surface area for sample C. The critical feature of the exponential curves is the significant initial reduction in cumulative surface area which tended to increase substantially again in the 2nd and 3rd months. These variations suggest a uniform change in petrophysical properties taking place within the rock pore spaces. The overall effect as suggested by the graph is such that there is no significant net change in the cumulative surface area for this sample in pore spaces that are greater than 5.5nm.

The evolution of the specific surface area for each of the samples examined indicate that pore space properties can be shifted uniformly at the nano-scale level with possible aggregated consequences for fluid flow and mineralogical changes at least at the part per million scale observed in the ICP-OES results.

The concentration of cumulative surface area in the narrow range of about 1.5nm to 30nm of pore sizes in all the samples is perhaps their singular homogeneous petrophysical property.

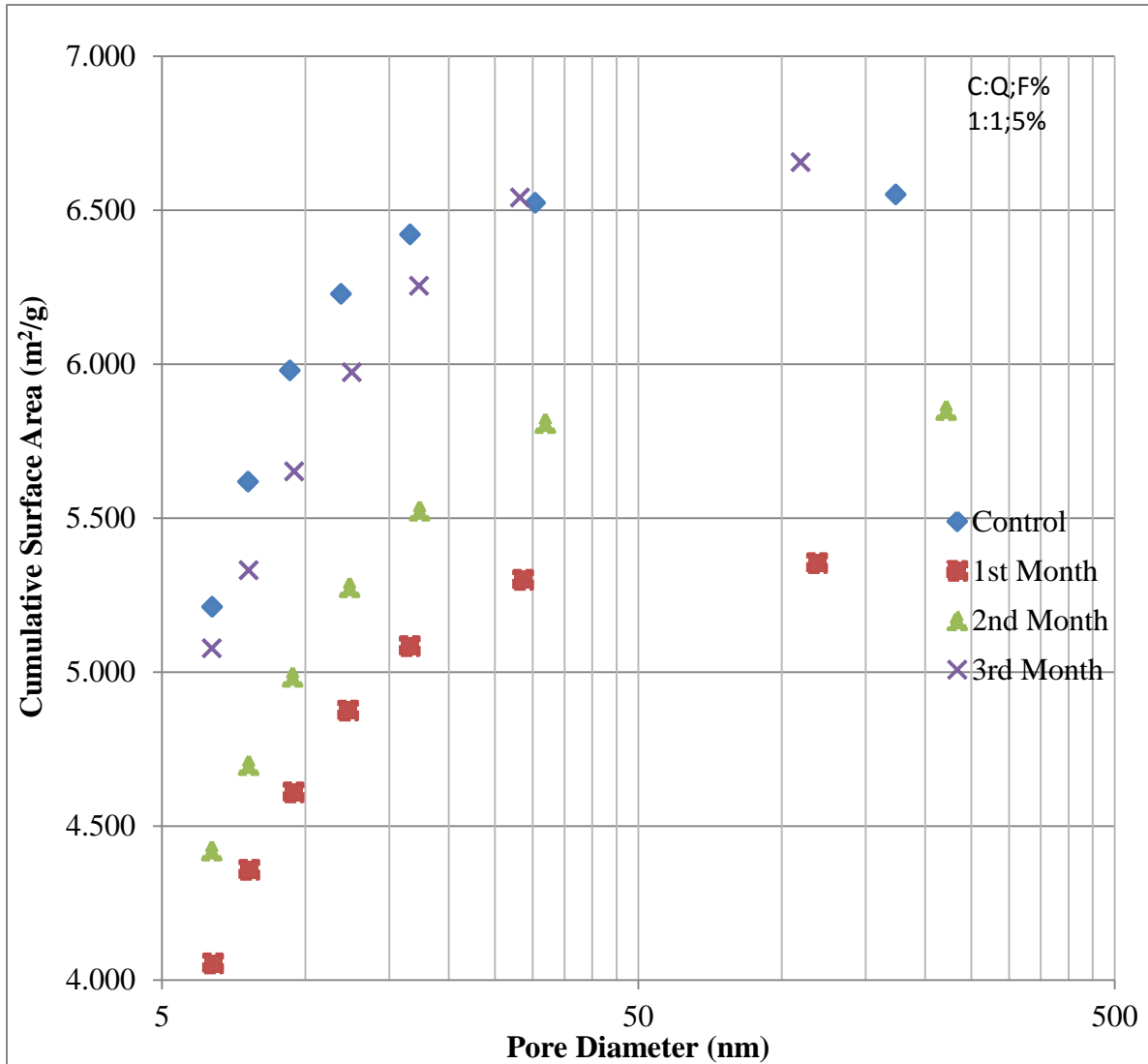


Figure 4.37: Cumulative specific surface area for sample C with greater than 5.5nm pores over the 3 months of CO₂-brine flooding. It shows an insignificant net increase in surface area at the end of the 3rd month

d) Specific Pore Volume of Pore Sizes Greater Than 5.5nm

1) Sample A

The cumulative pore volume curves for pore sizes that are greater than 5nm for sample A are shown in figure 4.38. The curves are partially exponential with the cumulative values associated with pore sizes greater than 30nm not associated with a plateau-like form as observed in the cumulative surface area plot discussed earlier. The changes in the cumulative pore volume

for this sample is more significant for pore sizes that ranges between 20nm and 300nm compared to the 5.5nm to 20nm range of pore sizes. The effect of reactive dissolution/precipitation processes appears to be more pronounced in volumetric quantity than in surface area for this sample.

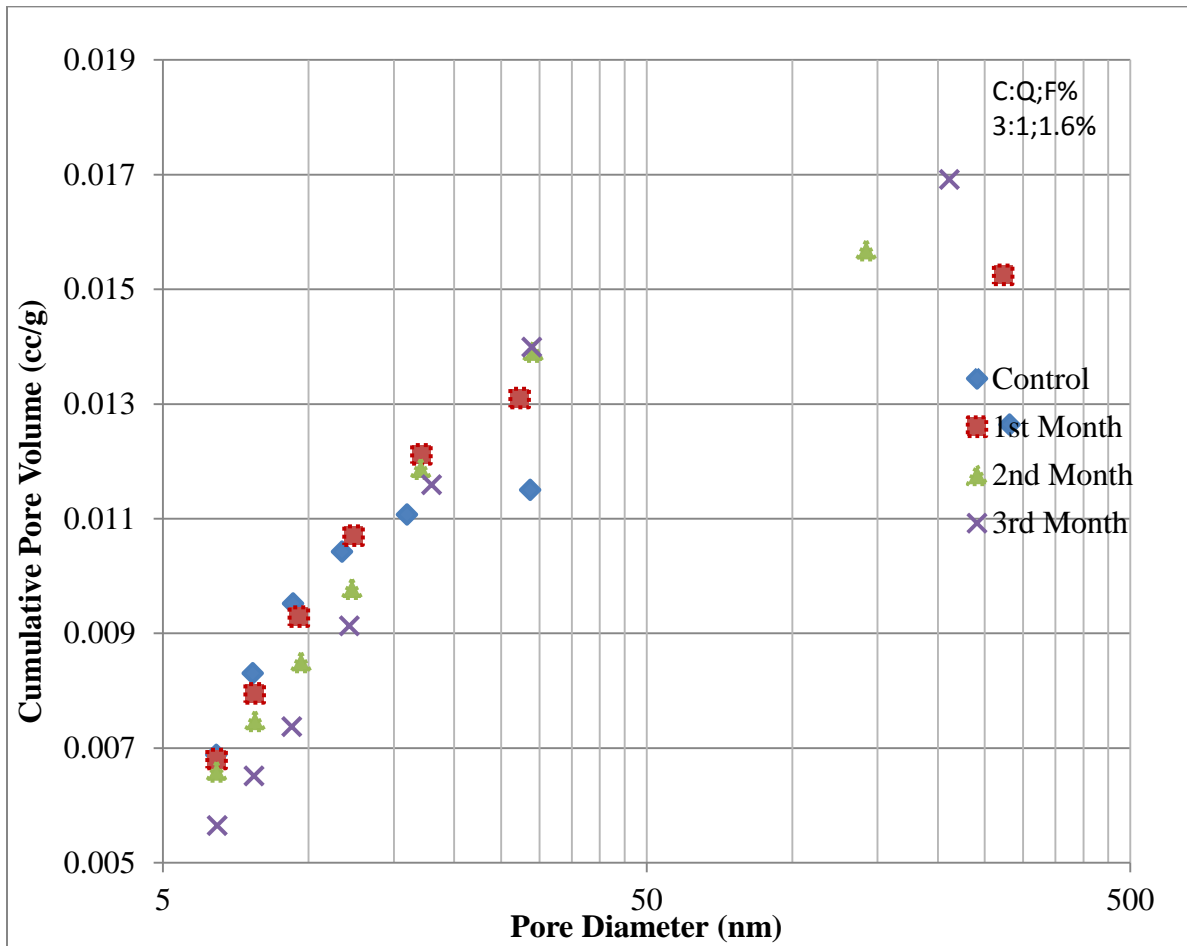


Figure 4.38: Cumulative pore volume for sample A with greater than 5.5nm pores over the 3 months of CO₂-brine flooding. It shows a significant net increase in pore volume for pore sizes greater than 30nm

The overall effect is such that there is a small decrease in volume for pores that are less than 20nm and large increase for pores that are larger than 20nm with the rate of the increase more pronounced in the 1st and 2nd months. Although the bulk of the pore volume still resides in the less than 30nm pore size range.

2) Sample B

Sample B shows a different change rate in the cumulative pore volume plots (Figure 4.39). Though the curve is partially exponential, the curve has a narrower and less significant volumetric change occurring at pore sizes that are less than 20nm compared to sample A.

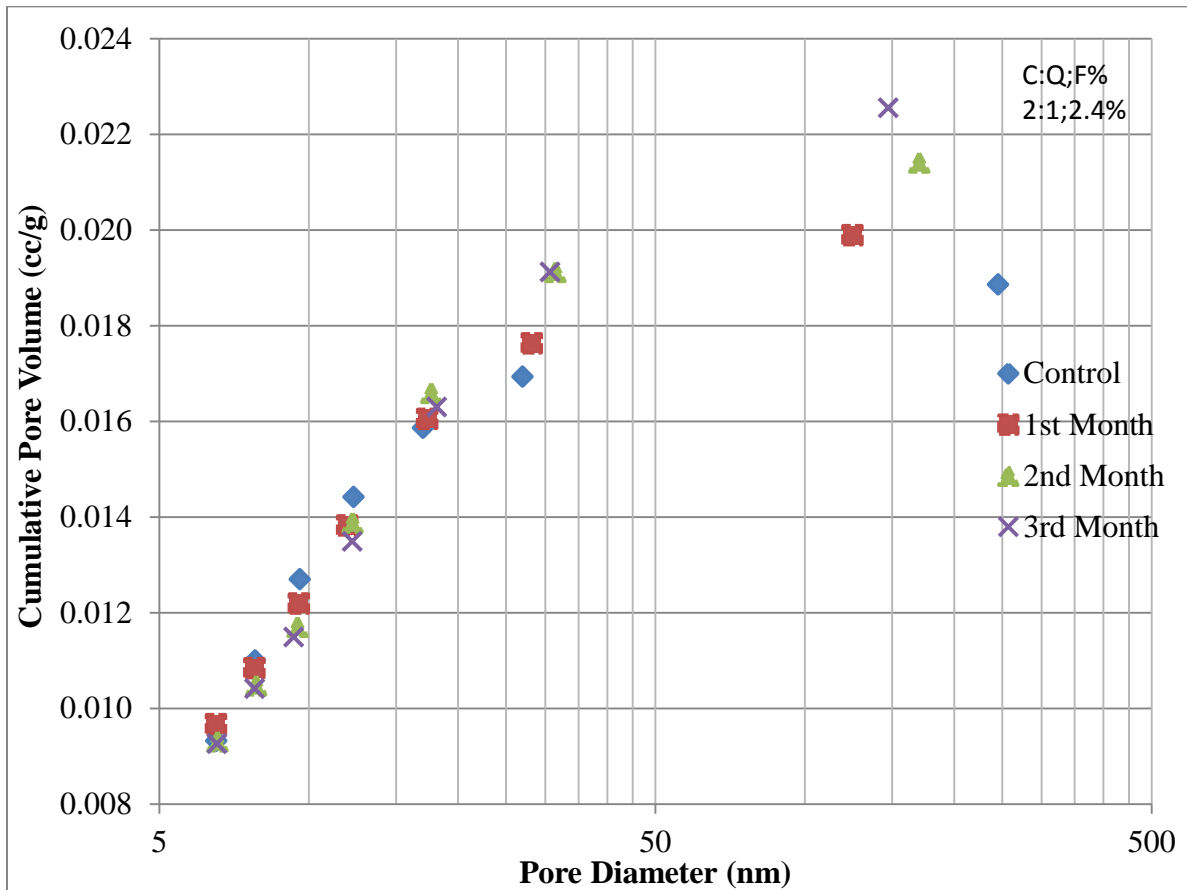


Figure 4.39: Cumulative pore volume for sample B with greater than 5.5nm pores over the 3 months of CO₂-brine flooding. . It shows a significant net increase in pore volume for pore sizes greater than 30nm

The cumulative volume change in pore sizes that are less than 20nm is a reduction which occurs till the 3rd month of the experiment; though the band is much narrower. The significant increases for pore sizes that are greater than 20nm appear to be uniform over the 3-month experimental period. The bulk of the pore volume resides in the less than 30nm pores and this trend is noticeable in all the samples that have been discussed.

3) Sample C

Figure 4.40 depicts the cumulative pore volume variations in sample C over the course of the experiment. The shape of the curve is also partially exponential and overly stretched out. The starting points of the cumulative volume for individual plots are much lower than samples A and B with a large volumetric change for pore sizes larger than 30nm.

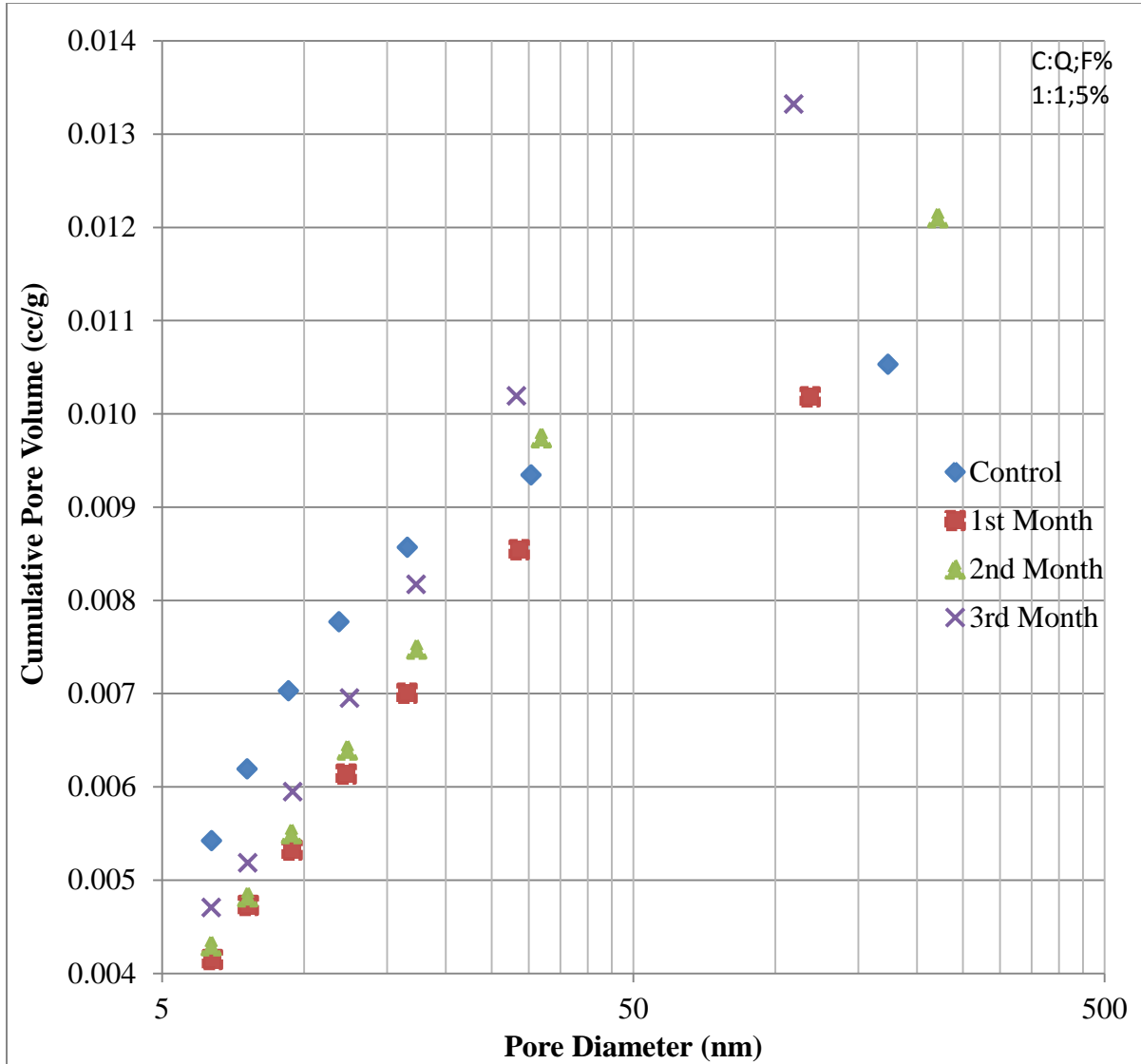


Figure 4.40: Cumulative pore volume for sample C with greater than 5.5nm pores over the 3 months of CO₂-brine flooding. It shows a significant net increase in pore volume for pore sizes greater than 30nm

The net reduction in cumulative pore volume for pores that are lower than 20nm on the curves suggests that dissolution-precipitation reaction processes counter each other effectively in tighter pores than in larger pores where the effect of dissolution may be dominant. Volumetric capacity in the shale caprock is shown to reside predominantly in pore spaces that are less than 30nm as reflected in all the figures associated with specific surface area and pore volume. It can be inferred that pores that hold the larger volume of spaces in the shale rocks might experience the net effect of geochemical activities as a result of rock-fluid interaction during diffusive loss of CO₂ into the caprock and subsequent dissolution.

4.5 Permeability Implication

Using the Karman-Cozeny Equation which estimates permeability from rock properties such as porosity, specific surface area and tortuosity, the impact of the nano-scale changes observed during the shale caprock/CO₂-brine flooding experiment were quantified. Applying the following assumptions to the size-reduced units of the experimental shale caprocks:

- i. Tortuosity is unchanged
- ii. Bulk rock volume is much larger than pore spaces
- iii. Only inter-connected pores are involved

Mathematical transformations were made to obtain permeability ratios for the three samples over the 3-month experimental period. This resulted in a ratio that involved only the pore volumes and the specific surface of the rock samples. It should be noted that as an approximation the ratio of the pore volumes were taken to be equivalent to the ratio of the porosity. Equations (23), (24), (25) and (26) below capture these mathematical transformations applying previously stated assumptions;

$$k_i = \frac{\phi_i^3}{2\tau_i(1 - \phi_i)^2 a_{vi}^2} \dots\dots\dots (23)$$

$$\frac{k_2}{k_1} = \frac{\left[\frac{\tau_1}{\tau_2} \right] \left[\frac{\phi_2^3}{\phi_1^3} \right] \left[\frac{(1 - \phi_1)^2}{(1 - \phi_2)^2} \right] \left[\frac{a_{v1}^2}{a_{v2}^2} \right]}{\dots\dots\dots} \dots\dots\dots (24)$$

$$\frac{k_2}{k_1} = \left[\frac{\phi_2^3}{\phi_1^3} \right] \left[\frac{a_{v1}^2}{a_{v2}^2} \right] \dots\dots\dots (25)$$

Therefore,

$$\frac{k_{i+1}}{k_i} = \left[\frac{\phi_{i+1}^3}{\phi_i^3} \right] \left[\frac{a_{vi}^2}{a_{vi+1}^2} \right] \dots\dots\dots (26)$$

k = de-consolidated rock permeability

ϕ = porosity

a_v = specific surface area

τ = tortuosity

Figure 4.41 showed the plot of the permeability ratio with the control sample as the starting point and having a ratio of unity. The control sample is the base permeability for all the ratio data points on the graph i.e k_i = permeability of control sample for each month. Appendix E documents the calculation procedures for these ratios. It is interesting to note that the most significant permeability ratio change is in the shale rock sample with the smallest clay content (sample C) while the lowest permeability ratio change is observed in the sample with clay to

quartz ratio of 2:1 (sample B). Sample A with clay to quartz ratio of 3:1 appeared stable in permeability ratio over the three months of flooding with CO₂- rich brine.

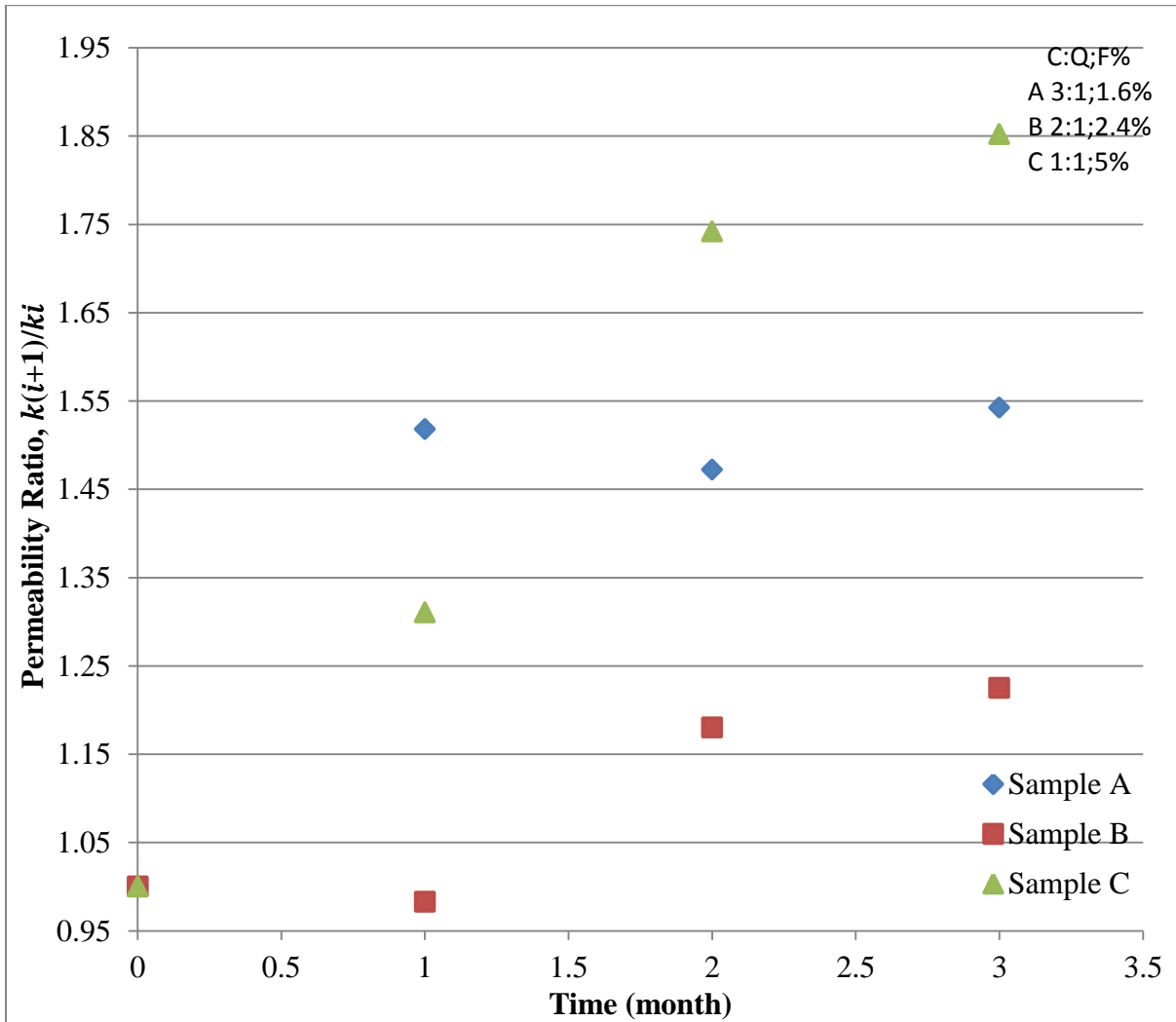


Figure 4.41: Plot of permeability ratio of the shale caprock samples over the 3- month experimental period. Sample B consistently had the lowest ratio indicating a strong resistance to flow within connected rock matrix pores

All the three samples can be observed plateauing out with respect to their permeability ratio by the third month of CO₂ flooding. The worst case change in permeability for this sample is by a factor of 2. The impact of these factors on diffusive transport and carbon accounting could be significant for a typical CO₂ sequestration site over the long term.

4.6 Dimensionless Numbers

The dimensionless numbers considered in this research work relates to the concepts of diffusion, convection and reaction kinetics. Assumptions were made with respect to these parameters which are not normally constant. Relevant experimentally measured values from the literature were used in computing these dimensionless quantities. Below are the discussions on Peclet and Peclet-Damkohler Numbers. Detailed calculations are presented in Appendix F.

4.6.1 Peclet Number

As mentioned under the literature review in chapter 2, Peclet Number (Pe) describes the effect of advection relative to that of molecular diffusion on solute transport and it is the ratio between convective and diffusive fluxes. The plot shown in Figure 4.42 depicts the Pe values for the shale caprock samples and their interaction with CO₂-brine. The graph shows that there is the Peclet number for sample is the highest in the Pe values over the first month of the experiment with the latter two months showing a more stable Pe value. This implies rapid initial diffusion of aqueous CO₂ into the shale rock samples aided only slightly in the first month of the experiment by convection. The 10⁻¹⁰ magnitude on the Pe plot ascribes dominance to diffusion over convection. It suggests that molecular diffusion plays an important role in reactive transport of aqueous CO₂ into the pore spaces of the shale caprock.

4.6.2 Peclet-Damkohler Number

Peclet-Damkohler Number (PeDa) describes the effect of reactive fluxes relative to diffusion and it is used frequently because convective effects diminish at the interface. Figure 4.43 shows the plot of the predicted PeDa number. It suggests that the changes in average and modal pore diameters are heavily dependent on reaction. The significantly low value of the

diffusion coefficient for CO₂-brine/shale caprock interaction suggest that the largest impact on PeDa number comes from the pore size parameter which is part of the variables that define the PeDa number. Hence the results are approximate dimensionless values.

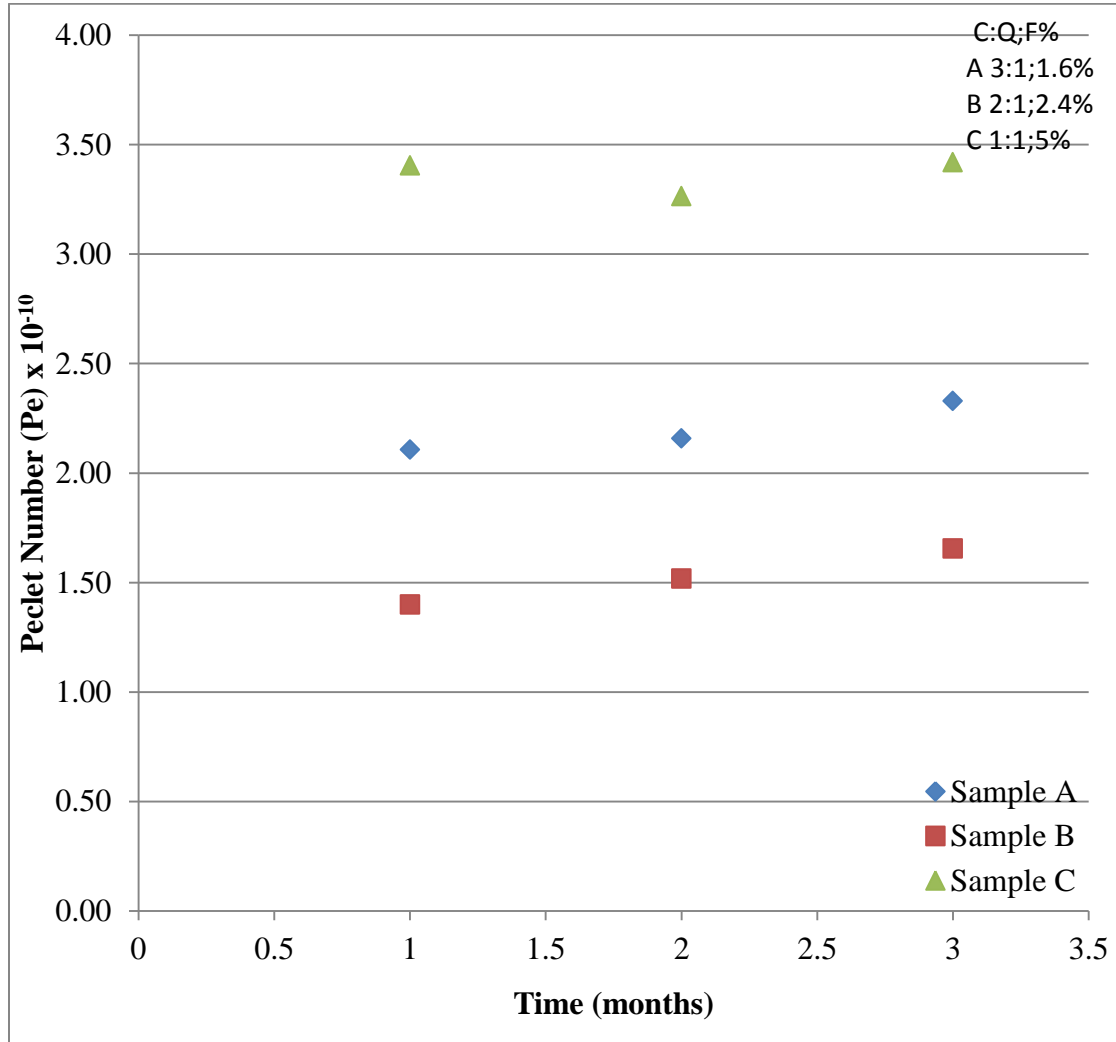


Figure 4.42: Peclet Number variation over the 3-month experimental period. It indicates a uniform diffusion process into the shale caprocks with sample B having the lowest Peclet values

It should be re-emphasized that the intrinsic kinetic rate k_r of mineral precipitation and dissolution for this experiment is assumed to be constant. This invariably makes PeDa number to be directly proportional to the pore diameter. While the reaction rate is not expected to be

constant, the approximation suffices for estimating the range of the dimensionless number which in this case is in the order of 10^{-2} . This range is associated with low mineral dissolution rate.

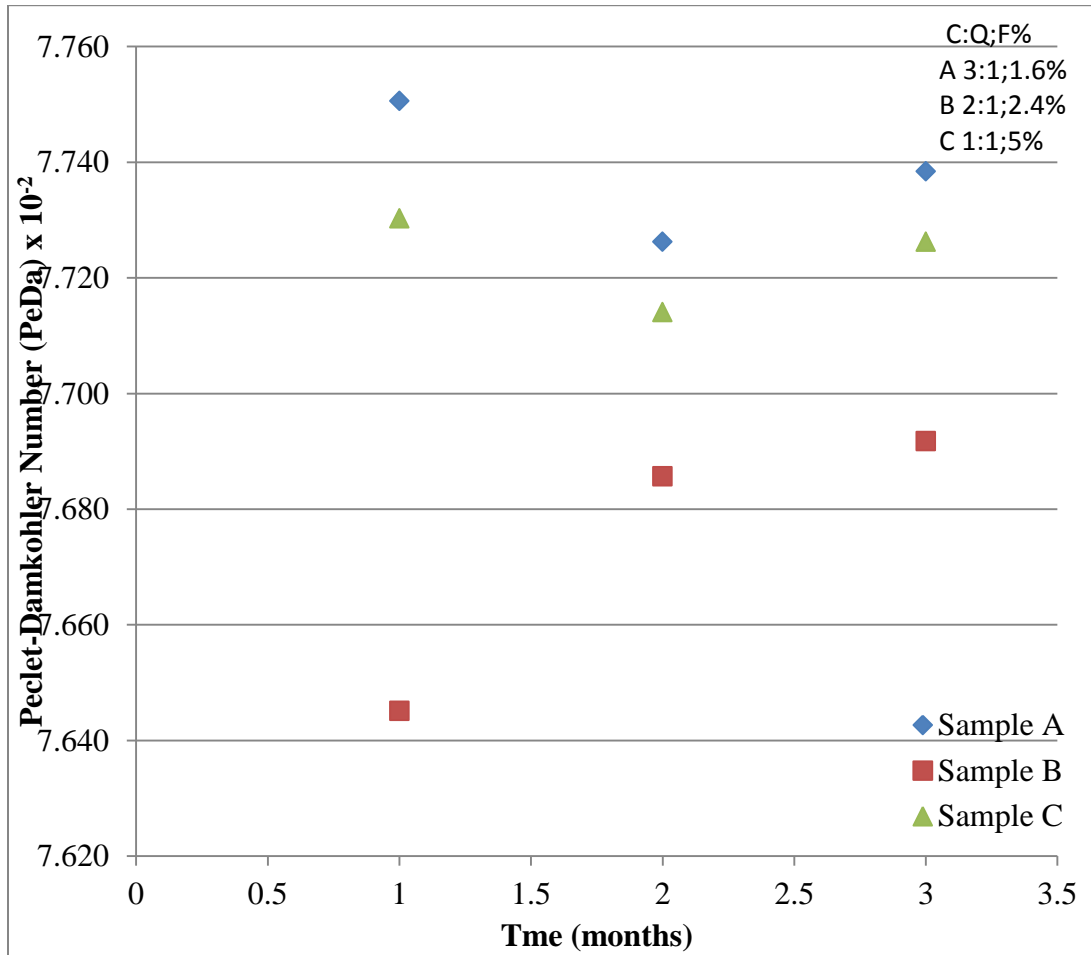


Figure 4.43: Peclet-Damkohler Number variation over the three month experimental period. The reactive components of PeDa indicate a direct relationship between geochemical interactions and pore size distribution

4.7 General Discussion of Results

- a) The geochemical observations from the combined use of pH measurement, ICP-OES, XRD and EDS performed on the crushed shale caprock, the effluent fluid collected over the three months of CO₂-brine flooding and the brown-like precipitates formed after

exposure to the atmosphere indicated an active geochemical interaction between the shale caprock and the CO₂-brine experimental fluid. The pH measurements (figure 4.3) of effluent fluid showed the (alkaline) reactive strength of the shale caprock in the first month of the experiment, with the pH value stabilizing in the second month before taking a gradual dip by the middle of the third month. This suggests a form of buffering strength for the shale caprock in case CO₂ diffuses into the connate pore waters of the caprock during CO₂ plume development as can be expected during CO₂ sequestration.

The ICP-OES (figure 4.4) results further confirmed the geochemical interaction noticed in the pH measurements. High concentration of Ca²⁺, Mg²⁺ and other alkaline earth metals (Na⁺ and K⁺ could have reflected a significant increase in concentration but for their already high amounts in the experimental CO₂-brine fluid used) indicated mineral dissolution from the pore spaces of the caprock that were penetrated at the 970psi back pressure imposed. The minerals that are suspected of releasing these cations as identified by X-Ray Diffraction (XRD) analysis include magnesium-rich Muscovite [(K,Na)(Al,Mg,Fe)₂(Si₃Al)O₁₀(OH)₂], Iron-rich Chlorite [(Mg,Fe)₆(Si,Al)₄O₁₀(OH)₈], Kaolinite [Al₂Si₂O₅(OH)₄], Orthoclase [(KAlSi₃O₈)] and Albite [(NaAlSi₃O₈)]. These mineral are capable of exchanging alkaline earth metals in acidic medium as relatively slow kinetic rates. The formation of ionic complexes such as [Fe(H₂O)₆]²⁺, [Fe(H₂O)₆]³⁺ and Al(OH)₄]⁻ may yield free radicals that are capable of driving reactions toward the right leading to precipitation of secondary minerals in the rock.

The bulk XRD analysis carried out on the experimental crushed shale caprock reflected considerable changes in mineral composition of the rock as shown by the

altered undulations of mineral peaks (heights) and the reduced noise levels in the X-ray diffractogram (figures 4.4 to 4.7) for the three caprock samples. Tables 4.2, 4.3 and 4.4 which captured the quantitative changes of the minerals indicated significant changes in Kaolinite, Muscovite, Chlorite and Felsdpar when compared with the control samples. Muscovite to chlorite ratio also changed by a maximum factor of 0.5 when only the CO₂-brine flooded samples are considered. The tables showed values that indicated varying reduction and increment over the three months experimental period. This suggested that the geochemical reactivities noticed in the effluent fluid affected the bulk caprock on a scale that XRD analysis can detect particularly with respect to the clay minerals. EDS analysis showed a varying amount of elemental species on the surface of the rock. Iron (Fe) is highest in the effluent precipitate, suggesting a conversion of leached soluble Fe²⁺ compounds to amorphous Fe³⁺ compound through atmospheric oxidation (hematite, Fe₃O₄ suspected). Aluminum and Silicon were also present in appreciable percentage with a possibility of Aluminum Oxide and Silica as the other constituents of the effluent precipitate (Silica was identified by the XRD analysis performed on the precipitate as shown by figure 4.29).

The physical appearance of the shale caprock at high resolution and magnification from SEM imaging micrograph (figures 4.8, 4.10, 4.12, 4.14, 4.15 and 4.16) showed special features that can be associated with mineralogical changes and natural rock heterogeneity. These changes defer extensively for the three samples that were analyzed. For sample A closing of pores were noticed while sample B showed secondary precipitation feature. Sample C indicated a wider pore features after the last month of flooding with CO₂-brine. The presence of connected pore spaces in the rock as observed

through optical microscopy imaging of thin-section samples (figure D.19 in the appendix) suggested that only limited feature changes can be observed particularly along the length of these connected nano-pores. The three types of pores present in the rock were identified as through, blind and closed pores indicating that not all the pore spaces present in the caprock can actually be reached by inducing flow through the caprock, artificially or naturally.

- b) The BET technique used in the estimation of internal pore geometrical properties such as specific surface area and pore volume indicated that the geochemical changes observed can affect petrophysical properties of the rock at nano-scale level. The bulk specific surface area and pore volume increased progressively for each sample over the three month experimental period with similar graphical trend (figures 4.22 and 4.23). The exception was the graphical trend for Sample C over the first month of the experiment as depicted by figures 4.22 and 4.23. These part of the plots showed that shale caprock-aqueous CO₂ interaction can cause a decrease in specific surface area and pore volume. This in part, supports simulation results from Lawrence Livermore National Laboratory that geochemical changes can counter geomechanical alterations by continuously constricting geomechanical apertures through precipitation, though in this case petrophysical properties were measured.

The average pore diameter as well as the modal pore size (figures 4.24 and 4.25) followed different trends from the bulk specific surface area and pore volume, indicating haphazard dissolution/precipitation of rock minerals at the pore throat. This is highly influenced by diffusion and kinetic rate of shale caprock/CO₂-brine interaction at the nano-scale level. The bulk pore size distribution for the samples over the three month

experimental period showed that for specific pore diameter ranges, an increase in pore volume is more likely than a decrease. Figures 4.26, 4.27 and 4.28 all showed increases in pore volumes for points 1, 2 and 4 as indicated on the graphs while only point 3 reflected a net decrease in pore volume at the end of the three months of CO₂-brine flooding for all the three experimental samples. This suggests a 25% possibility of shale caprock appreciation and a 75% possibility of shale caprock depreciation under the worst case scenario of pervasive CO₂ ingress by diffusion into the caprock.

Analyzing further, the distribution of pore sizes with respect to cumulative specific surface area and pore volume (figures 4.29 to 4.40) revealed a consistent but slightly different trend for each of the caprock samples. The changes in cumulative specific surface area have wider bands than the cumulative specific pore volume for all the three samples. This indicates that changes in specific surface area are more pronounced than changes in specific pore volume. For all the three samples, the lower end (< 3.5nm) of the cumulative curves were most significantly affected by geochemical interaction between the shale caprock and the CO₂-brine fluid. Changes in specific surface area for the upper end of the cumulative curves were more significant for >5.5nm pore sizes while the changes in specific pore volume were more significant for the >20nm pore sizes. This showed that though the trend in specific surface area and pore volume may be similar, there still exist some subtle differences in the impact of geochemical alterations on these two pore space parameters.

Permeability ratio estimates (figure 4.41) , computed using the Carman-Kozeny equation which incorporated bulk specific surface area and pore volume showed that in the worst case scenario, intrinsic permeability cannot increase more than a factor of 2.

This might impact carbon accounting in the long term due to increased storage space in the lower part of the caprock. Sample B had the lowest permeability ratio of all the samples throughout the three months of CO₂-brine flooding. This was despite having the most visible changes in specific pore volume and surface area. Pore throat size appears to correlate well with the permeability ratio values for all the three samples.

- c) Estimation of Peclet (Pe) and Peclet-Damkohler (PeDa) Numbers (figures 4.42 and 4.43) from pore geometric parameters indicated that the diffusion of CO₂ saturated brine into the caprock would be uniform and dominates over reaction kinetics and convection. Pe number is in the order of 10^{-10} which implies that diffusion dominates strongly over convection in the tight shale rock with respect to aqueous CO₂ transport. The PeDa number is in the order of 10^{-2} which implies that diffusion weakly dominates over reaction kinetics (reaction front movement) making the reaction rate a significant factor in caprock evaluation as part of reservoir characterization in CO₂ sequestration. Diffusion into the shale caprock is expected to be the primary transport mechanism for CO₂ stored in the sub-surface to invade intact caprock as convective fluid movement is strongly constrained by the tightness of the interconnected pores that may exist in the rock. This further implies that reaction rate will be highly dependent on diffusion coefficient for shale/ aqueous CO₂ interaction. Reactive flow in the long term can cause significant changes in pore throat sizes albeit with progressively lower kinetic rates. Geochemical interaction is expected to uniformly slow down over time as mineral substrates availability from the caprock decreases.

CHAPTER 5 CONCLUSIONS AND RECOMMENDATIONS

5.1 Conclusions

The geochemical interaction of shale caprock with aqueous CO₂ and its impact on the petrophysical properties of the rock have been investigated. The results presented showed that geophysical and petrophysical properties of shale rocks can be significantly altered by minute geochemical changes that are hard to detect particularly at the submicron level. Effluent analysis which showed a high percentage of Ca²⁺ indicated the tendency of calcium based minerals and other alkaline earth metal compounds to dissolve easily in mildly acidic brine with relatively stable pH. These geochemical changes affect the pore volumes, surface area and pore diameters of shale caprock such that in all the samples examined their values tended to increase with time though at reduced rates in the later months of the experiment. These nano-scale changes varied significantly depending on the range of pore diameters that are being considered. The following major conclusions can be reached from this experimental investigation;

1. The pH of effluent from shale caprock/CO₂-brine interaction under continuous contact mode tends to increase initially and decrease almost linearly over time indicating geochemical activity.
2. Alkaline earth minerals in the form of Ca²⁺, Mg²⁺, Fe²⁺, Mn²⁺ and Al³⁺ compounds are susceptible to dissolution due to continuous flow of mildly acidic CO₂-brine solution. This does not exclude the alkali metals ions of Na⁺ and K⁺ as their percentage change is significantly masked by the brine composition used in this experimental research.
3. Re-precipitation of dissolved minerals in amorphous forms is possible, particularly under oxygen rich conditions.
4. Pore space geometric parameters such as specific pore volume, specific surface area and

pore diameter in tight shale caprock can increase at the nano-scale level under continuous contact with CO₂-brine.

5. The impact of reactive transport of aqueous CO₂ through shale caprock is such that the intrinsic permeability under the worst case scenario can increase by up to a factor of 2.
6. Carbon accounting and caprock integrity with respect to permeability can be impacted by shale caprock/CO₂-brine interaction under continuous flow conditions.
7. Dimensionless numbers that account for the impacts of diffusion, convection and reaction kinetics can reveal the uniformity or non-uniformity of reactive transport parameters in shale caprock/CO₂-brine interaction.

5.2 Recommendations

It is recommended that the volumetric significance of fractional permeability changes as a result of geochemical interactions and petrophysical properties alterations in shale seals overlaying potential CO₂ repositories should be extensively investigated. Also their potential to serve as pressure perturbation dampers and provide increased storage space which may help limit the impacts of pressure-induced geomechanical changes particularly at the caprock/reservoir rock interface should be researched through experimental and simulation tools.

The conditions that best favor geochemical re-precipitation need to be investigated, particularly under oxygen deprived conditions similar to what is obtainable in the subsurface. This will provide clues into the possibility of fine-grained precipitates plugging the type of nanopores identified in the shale caprock as observed and measured quantitatively in the samples used for this experiment.

REFERENCES

1. “Carbon Sequestration Atlas of the United States and Canada”. National Energy Technology Laboratory, Department of Energy 2010. Vol. 3: p. 162.
2. Li, Z., Dong, M., Li, S., Huang, S.: “CO₂ sequestration in depleted oil and gas reservoirs--caprock characterization and storage capacity”. *Energy Conversion and Management*, 2006. 47(11-12): p. 1372-1382.
3. Lima, V.D., Einloft, S., Ketzer, J.M., Jullien, M., Bildstein, O., Petronin, J.C.: “CO₂ Geological storage in saline aquifers: Paraná Basin caprock and reservoir chemical reactivity”. *Energy Procedia*, 2011. 4: p. 5377-5384.
4. Shukla, R., Ranjith, P., Haque, A., Choi, X.: “A review of studies on CO₂ sequestration and caprock integrity”. *Fuel*, 2010. 89(10): p. 2651-2664.
5. Randolph, J.B. and Saar M.O.: “Coupling carbon dioxide sequestration with geothermal energy capture in naturally permeable, porous geologic formations: Implications for CO₂ sequestration”. *Energy Procedia*, 2011. 4: p. 2206-2213.
6. Farokhpoor, R., Torsater, O., Baghbanbashi, T., Mork, A. and Lindeberg, E.G.B.: “Experimental and Numerical Simulation of CO₂ Injection Into Upper-Triassic Sandstones in Svalbard”, Norway, in SPE International Conference on CO₂ Capture, Storage, and Utilization. 2010: New Orleans, Louisiana, USA.
7. Rosenbauer, R.J., Koksalan T., and Palandri, J.L.: “Experimental investigation of CO₂-brine-rock interactions at elevated temperature and pressure: Implications for CO₂ sequestration in deep-saline aquifers”. *Fuel Processing Technology*, 2005. 86(14-15): p. 1581-1597.
8. Eke, P.E., Curtis, A., and Haszeldine, S.: “CO₂-Brine Surface Dissolution and Injection: CO₂ Storage Enhancement, in Offshore Europe”. 2009: Aberdeen, UK.
9. Melien, T., “Economic and Cost Analysis for CO₂ Capture Costs in The CO₂ Capture Project Scenarios, in Carbon Dioxide Capture for Storage in Deep Geologic Formations”. 2005, Elsevier Science: Amsterdam. p. 47-87.
10. Arts, R., Chadwick, A., Eiken, O., Thibeau, S., Nooner, S.: “Ten years' experience of monitoring CO₂ injection in the Utsira Sand at Sleipner, offshore Norway”. *First Break*, 2008. 26: p. 65-72.
11. Johnson, J.W., Nitao, J.J., and Steefel, C.I.: “Fundamental Elements of Geologic CO₂ Sequestration in Saline Aquifers”, Geosciences and Environmental Tech. Div., Lawrence Livermore National Laboratory. 2006: Livermore, CA 94550.
12. Rutqvist, J., Birkholzer, J., Cappa, F. and Tsang, C.F.: “Estimating maximum sustainable injection pressure during geological sequestration of CO₂ using coupled fluid flow and

- geomechanical fault-slip analysis”. *Energy Conversion and Management*, 2007. 48(6): p. 1798-1807.
13. Chalbaud, C., Robin, M., Lombard, J.M., Martin, F., Egermann, P. and Bertin, H.: “Interfacial tension measurements and wettability evaluation for geological CO₂ storage. *Advances in Water Resources*, 2009. 32(1): p. 98-109.
 14. Aggelopoulos, C.A., Robin, M. and Vizika, O.: “Interfacial tension between CO₂ and brine (NaCl + CaCl₂) at elevated pressures and temperatures: The additive effect of different salts”. *Advances in Water Resources*, 2011. 34(4): p. 505-511.
 15. Espinoza, D.N. and Santamarina, J.C.: “Water-CO₂-mineral systems: Interfacial tension, contact angle, and diffusion, Implications to CO₂ geological storage”. *Water Resour. Res.*, 2010. 46(7): p. W07537.
 16. Wang, J., Ryan, D., Anthony, E.J., Wildgust, N. and Ailen, T.: “Effects of impurities on CO₂ transport, injection and storage”. *Energy Procedia*, 2011. 4: p. 3071-3078.
 17. Busch, A., Alles, S., Krooss, B.M., Stanjek, H and Dewhurst, D.: “Effects of physical sorption and chemical reactions of CO₂ in shaly caprocks”. *Energy Procedia*, 2009. 1(1): p. 3229-3235.
 18. Gaus, I.: “Role and impact of CO₂-rock interactions during CO₂ storage in sedimentary rocks”. *International Journal of Greenhouse Gas Control*, 2010. 4(1): p. 73-89.
 19. Allen, P.A. and Allen, J.R.: “Basin Analysis - Principles and Applications” (2nd Edition): John Wiley & Sons. 2005.
 20. Eiken, O., Ringrose, P., Hermanrud, C., Nazarian, B., Torp, T.A. and Hoier, L.: “Lessons learned from 14 years of CCS operations: Sleipner, In Salah and Snøhvit”. *Energy Procedia*, 2011. 4: p. 5541-5548.
 21. McPherson, B.: “Modeling Caprock Integrity: Assessment Objectives”. IEA-GHG CO₂ Geological Storage Modelling Workshop Orleans, France, 2009.
 22. Kohler, E., Parra, T. and Vidal, o.: “Clayey Cap-Rock Behavior in H₂O-CO₂ Media at Low Pressure and Temperature Conditions: An Experimental Approach”. *Clays and Clay Minerals*, 2009. 57(5): p. 616-637.
 23. Alemu, B.L.,Aagaard, P., Munz, I.A., and Skurtveit, E.: “Caprock interaction with CO₂: a laboratory study of reactivity of shale with supercritical CO₂ and brine”. *Applied Geochemistry*. In Press, Accepted Manuscript.
 24. Ellis, B.R., Bromhal, G.S., McIntyre, D.L. and Peters, C.A.: “Changes in caprock integrity due to vertical migration of CO₂ -enriched brine”. *Energy Procedia*, 2011. 4: p. 5327-5334.

25. Daniel, R.F., Kaldi, J.G.: “Evaluating Seal Capacity of Cap Rocks and Intraformational Barriers for CO₂ Containment”. AAPG Studies in Geology, 2009. Special Volume 59: p. Pages 335 - 345
26. Busch, A., Alles, S., Gensterblum, Y., Prinz, D., Dewhurst, D.N., Raven, M.D., Stanjek, H. and Krooss, B.M.: “Carbon dioxide storage potential of shales”. International Journal of Greenhouse Gas Control, 2008. 2(3): p. 297-308.
27. David, C. and Le Ravalec-Dupin, M.: “Rock physics and geomechanics in the study of reservoirs and repositories”. Geological Society, London, Special Publications, 2007. 284(1): p. 1-14.
28. Al-Bazali, T.M., Zhang, J., Chenevert, M.E., Sharma, M.M.: “Measurement of the Sealing Capacity of Shale Caprocks”, in SPE Annual Technical Conference and Exhibition. 2005: Dallas, Texas.
29. Johnson, J.W., Nitao, J.J and Morris, J.P.: “Reactive Transport Modeling of Cap-Rock Integrity during Natural and Engineered CO₂ Storage. Carbon Dioxide Capture for Storage in Deep Geologic Formations”, 2005. 2. Environmental Sciences Division, Lawrence Livermore National Laboratory, Livermore, CA, USA.
30. Khan, S., Han, H., Ansari, S.A. and Khosravi, N.: “An Integrated Geomechanics Workflow for Caprock-Integrity Analysis of a Potential Carbon Storage”, in SPE International Conference on CO₂ Capture, Storage, and Utilization. 2010: New Orleans, Louisiana, USA.
31. Gherardi, F., Xu, T. and Pruess, K.: “Numerical modeling of self-limiting and self-enhancing caprock alteration induced by CO₂ storage in a depleted gas reservoir”. Chemical Geology, 2007. 244(1-2): p. 103-129.
32. Streit, J.E., Siggins, A.F. and Evans, B.J.: “Predicting and Monitoring Geomechanical Effects of CO₂ Injection, in Carbon Dioxide Capture for Storage in Deep Geologic Formations”. 2005, Elsevier Science: Amsterdam. p. 751-766.
33. Oldenburg, C.M., Pruess, K. and Benson, S.M.: “Process Modeling of CO₂ Injection into Natural Gas Reservoirs for Carbon Sequestration and Enhanced Gas Recovery”. Energy & Fuels, 2001. 15(2): p. 293-298.
34. Heath, J., McPherson, B., Phillips, F., Cooper, S. and Dewersd, T.: “Natural helium as a screening tool for assessing caprock imperfections at geologic CO₂ storage sites”. Energy Procedia, 2009. 1(1): p. 2903-2910.
35. Stevens, S.H.: “Natural CO₂ Fields as Analogs for Geologic CO₂ Storage”. 2005. Volume 2(Carbon Dioxide Capture for Storage in Deep Geologic Formations – Results from the CO₂ Capture Project Geologic Storage of Carbon Dioxide with Monitoring and Verification, Sally M. Benson, Lawrence Berkeley Laboratory, Berkeley, CA, USA): p. Pages 687-697.

36. Wollenweber, J., Alles, S.A., Kronimus, A., Busch, A., Stanjek, H. and Krooss, B.M.: "Caprock and overburden processes in geological CO₂ storage: An experimental study on sealing efficiency and mineral alterations". *Energy Procedia*, 2009. 1(1): p. 3469-3476.
37. Blencoe, J.G., Cole, D.R., Horita, J. and Moline, G.R.: "Experimental geochemical studies relevant to carbon sequestration". *The First National Conference on Carbon Sequestration*, U.S. National Energy Technology Laboratory, Washington, DC 2001: p. p. 14.
38. Armitage, P.J., Worden, R.H., Faulkner, D.R., Aplin, A.C., Butcher, A.R. and Liffe, J.: "Diagenetic and sedimentary controls on porosity in Lower Carboniferous fine-grained lithologies, Krechba field, Algeria: A petrological study of a caprock to a carbon capture site". *Marine and Petroleum Geology*, 2010. 27(7): p. 1395-1410.
39. Murphy, R., Lammers, K., Smirnov, A.A., Schoonen, M.A.A. and Strongin, D.R.: "Ferrihydrite phase transformation in the presence of aqueous sulfide and supercritical CO₂". *Chemical Geology*, 2010. 271(1-2): p. 26-30.
40. Sam, H., etal: "Best Practice Manual from SACS - Saline Aquifer CO₂ Storage Project". *IEA Greenhouse Gas R&D Programme*, 2007: p. 58.
41. Xu, T., Apps, J.A. and Pruess, K.: "Mineral sequestration of carbon dioxide in a sandstone-shale system". *Chemical Geology*, 2005. 217(3-4): p. 295-318.
42. Wigand, M., Kaszuba, J.P., Carey, J.W. and Hollis, W.K.: "Geochemical effects of CO₂ sequestration on fractured wellbore cement at the cement/caprock interface". *Chemical Geology*, 2009. 265(1-2): p. 122-133.
43. Tosaya, C.A.: "Acoustic Properties of Clay-Bearing Rock", PhD Dissertation in the Department of Geophysics. 1982, Stanford University: Stanford.
44. Bergaya, F. and Lagaly, G.: "Clays, Clay Minerals, and Clay Science", Chapter 1 General Introduction in *Developments in Clay Science*. 2006, Elsevier. p. 1-18.
45. Yoshioka, H. and Ishiwatari, R.: "Characterization of organic matter generated from Green River shale by infrared laser pyrolysis". *Geochemical Journal*, 2002. 36: p. 73-82.
46. Jordan, P.D., Oldenburg, C.M. and Nicot, J-P.: "Characterizing fault-plume intersection probability for geologic carbon sequestration risk assessment". 2008.
47. Morris, J., Johnson, S. and Friedmann, S.J.: "Geomechanical Simulations of Caprock Integrity Using the Livermore Distinct Element Method". 2008. p.1-10
48. Busch, A., Amann-Hildenbrand, A., Bertier, P., Waschbuesch, M. and Krooss, B.M.: "The Significance of Caprock Sealing Integrity for CO₂ Storage", in *SPE International Conference on CO₂ Capture, Storage, and Utilization*. 2010: New Orleans, Louisiana, USA.

49. Oldenburg, C.M., Jordan, P.D., Nicot, J-P., Mazzoldi, A., Gupta, A.K., and Bryant, S.L.: "Leakage risk assessment of the In Salah CO₂ storage project: Applying the certification framework in a dynamic context". *Energy Procedia*, 2011. 4: p. 4154-4161.
50. Zhou, X., Zeng, Z. and Liu, H. "Laboratory Testing On Pierre Shale For CO₂ Sequestration Under Clayey Caprock", in 44th U.S. Rock Mechanics Symposium and 5th U.S.-Canada Rock Mechanics Symposium. 2010, Salt Lake City, Utah.
51. Wo, S. and Liang, J.-T.: "CO₂ Storage in Coalbeds: CO₂/N₂ Injection and Outcrop Seepage Modeling, in Carbon Dioxide Capture for Storage in Deep Geologic Formations". 2005, Elsevier Science: Amsterdam. p. 897-924.
52. Zhang, G., Wei, Z. and Ferrell, R.E.: "Elastic modulus and hardness of muscovite and rectorite determined by nanoindentation". *Applied Clay Science*, 2009. 43(2): p. 271-281.
53. Pusch, R. "Chapter 6 Mechanical Properties of Clays and Clay Minerals, in Developments in Clay Science". 2006, Elsevier. p. 247-260.
54. Shipton, Z.K., Evans, J.P., Dockrill, B., Heath, J., Williams, A., Kirchner, D. and Kolesar, P.T.: "Natural Leaking CO₂-Charged Systems as Analogs for Failed Geologic Storage Reservoirs, in Carbon Dioxide Capture for Storage in Deep Geologic Formations". 2005, Elsevier Science: Amsterdam. p. 699-712.
55. Ferronato, M., Gambolati, G, Janna C. and Teatini, P.: "Geomechanical issues of anthropogenic CO₂ sequestration in exploited gas fields". *Energy Conversion and Management*, 2010. 51(10): p. 1918-1928.
56. Vilarrasa, V., Olivella, S., and Carrera, J.: "Geomechanical stability of the caprock during CO₂ sequestration in deep saline aquifers". *Energy Procedia*, 2011. 4: p. 5306-5313.
57. Khan, S., Han, H., Ansari S, and Khosravi, N.: "Geomechanical Modeling to Assess Caprock Integrity in Oil Sands". *Recovery CSPG CSEG CWLS Convention*, 2011: p. pgs 4.
58. Dahaghi, A.K.: "Numerical Simulation and Modeling of Enhanced Gas Recovery and CO₂ Sequestration in Shale Gas Reservoirs: A Feasibility Study", in SPE International Conference on CO₂ Capture, Storage, and Utilization. 2010: New Orleans, Louisiana, USA.
59. Bildstein, O., Jullien, M., Credo, A. and Garnier, J.: "Integrated modeling and experimental approach for caprock integrity, risk analysis, and long term safety assessment". *Energy Procedia*, 2009. 1(1): p. 3237-3244.
60. Al-Dliwe, A. and Asghari, K.: "Optimization of carbon dioxide sequestration and improved oil recovery in oil reservoirs". *GHGT7 Proceedings*, Vancouver, BC, Canada, September (2004).
61. Kvamme, B. and Liu, S.: "Reactive transport of CO₂ in saline aquifers with implicit geomechanical analysis". *Energy Procedia*, 2009. 1(1): p. 3267-3274.

62. Mutschler, T., Triantafyllidis, T. and Balthasar, K.: "Geotechnical investigations of cap rocks above CO₂ –resevoirs". *Energy Procedia*, 2009. 1(1): p. 3375-3382.
63. Hangx, S., Spiers, C. and Peach, C.: "The mechanical behavior of anhydrite and the effect of CO₂ injection". *Energy Procedia*, 2009. 1(1): p. 3485-3492.
64. Stone, M., Martinez, M.J. and Burns, A.: "Coupled Multi-Physics Modeling to Support Energy R&D". *Science Matters!*, Sandia National Laboratories, 2010: p. 1-2.
65. Busch, A., Gensterblum, Y., Krooss, B.M., and Siemons, N.: "Investigation of high-pressure selective adsorption/desorption behaviour of CO₂ and CH₄ on coals: An experimental study". *International Journal of Coal Geology*, 2006. 66(1-2): p. 53-68.
66. Ghajari, A.: "Investigating Cap Rock Efficiency of Laffan Shale Formation in Sirri Oil Fields, Offshore Iran". *CSCanada Advances in Petroleum Exploration and Developments*, 2011. 1(1): p. 8.
67. MacQuarrie, K.T.B. and Mayer, K.U.: "Reactive transport modeling in fractured rock: A state-of-the-science review". *Earth-Science Reviews*, 2005. 72(3-4): p. 189-227.
68. Xu, T., Kharaka, Y.K., Doughty, C., Freifeld, B.M. and Daley, T.M.: "Reactive transport modeling to study changes in water chemistry induced by CO₂ injection at the Frio-I Brine Pilot". *Chemical Geology*, 2010. 271(3-4): p. 153-164.
69. Algive, L., Bekri, S. and Vizika, O.: "Pore-Network Modeling Dedicated to the Determination of the Petrophysical-Property Changes in the Presence of Reactive Fluid". *SPE Journal*, 2010. 15(3): p. pp. 618-633.
70. Kang, Q., Zhang, D. and Chen, S.: "Simulation of dissolution and precipitation in porous media". *J. Geophys. Res.*, 2003. 108(B10): p. 2505.
71. Javadpour, F.: "CO₂ Injection in Geological Formations: Determining Macroscale Coefficients from Pore Scale Processes". *Trans Porous Med*, 2009. 79(1): p. 87-105.
72. Pitman, J.K., Pashin, J.C., Hatch, J.R, Goldhaber, M.B.: "Origin of minerals in joint and cleat systems of the Pottsville Formation, Black Warrior basin, Alabama: Implications for coalbed methane generation and production". *AAPG Bulletin*, 2003. 87(5): p. 713-731.
73. University of Alabama: "Site Characterization for CO₂ Storage from Cola-fired Power Facilities in the Black Warrior Basin of Alabama". *Recovery Act Proposal*. 2009: p. 41.
74. Yalcinkaya, T.: "Experimental Study on Single Cement Fracture Exposed to CO₂ Saturated Brine under Dynamic Conditions", *Master's Thesis in Petroleum Engineering*. 2010, Louisiana State University: Baton Rouge. p. 105.

75. Hildenbrand, A., Schlömer, S., Krooss, B.M. and Littke, R.: "Gas breakthrough experiments on pelitic rocks: comparative study with N₂, CO₂ and CH₄". *Geofluids*, 2004. 4(1): p. 61-80.
76. Hildenbrand, A., Schlömer, S. and Krooss, B.M.: Gas breakthrough experiments on fine-grained sedimentary rocks. *Geofluids*, 2002. 2(1): p. 3-23.
77. Thomas, J.J., Jennings, H.M. and Allen, A.J.: "The Surface Area of Hardened Cement Paste as Measured by Various Techniques". 2010; Available from: www.civil.northwestern.edu Thomas_SAreview CSE 1999.
78. Quantachrome Instrument: "Autosorb-1 Gas Sorption Manual. Analysis of Microporous Particles". 2006: p. 144.
79. Thibodeaux, L.J.: "Environmental Chemodynamics: Movement of Chemicals in Air, Water, and Soil". 1996: J. Wiley & Sons.

APPENDIX A
EXPERIMENTAL SETUP AND SAMPLE PREPARATION

A.1 Physical Experimental Setup and Materials

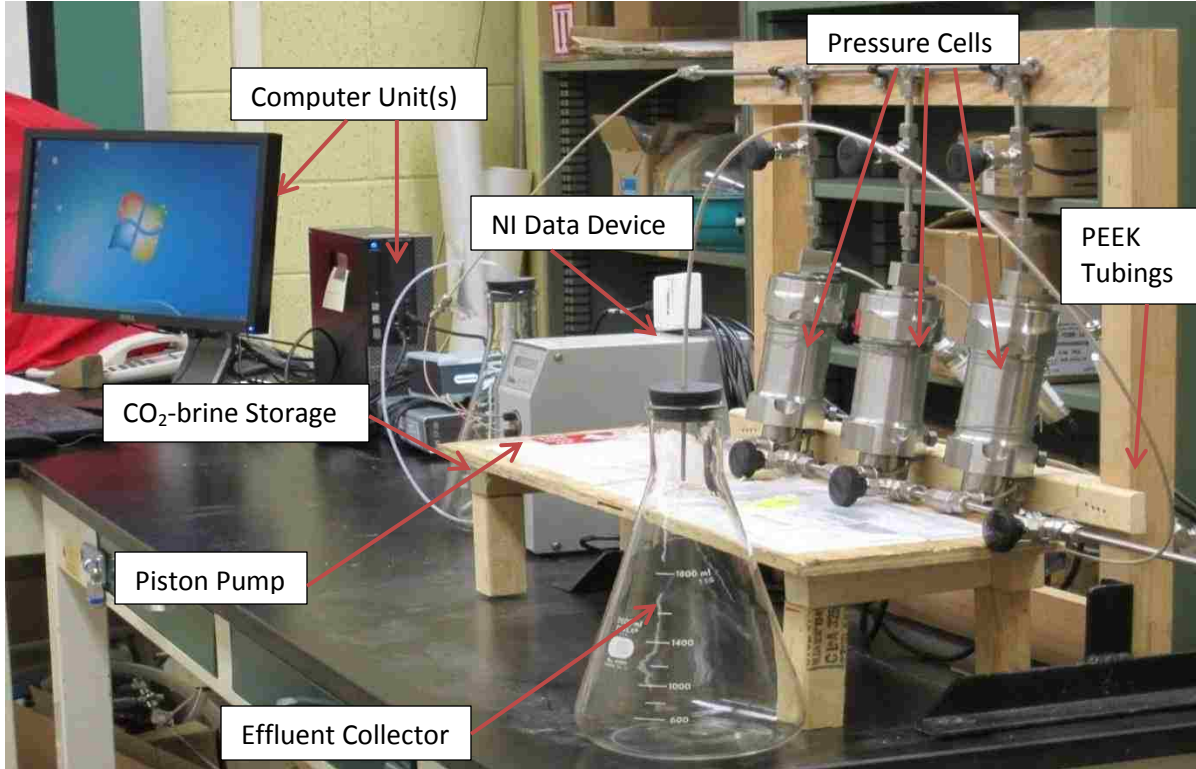


Figure A.1: Physical arrangement of experimental apparatus in shale caprock/CO₂-brine flooding



Figure A.2: Crushed shale caprock samples showing particle dimension



Figure A.3: Crushed shale caprock sample packed into a pressure cell



Figure A.4: Syringe pump used as backup pump in shale caprock/CO₂-brine flooding



Figure A.5: Crushed shale caprock control sample re-saturation under vacuum condition



Figure A.6: CO₂-brine preparation setup showing CO₂ cylinder and mixing tank



Figure A.7: Nitrogen cylinders used in operating back-pressure regulator

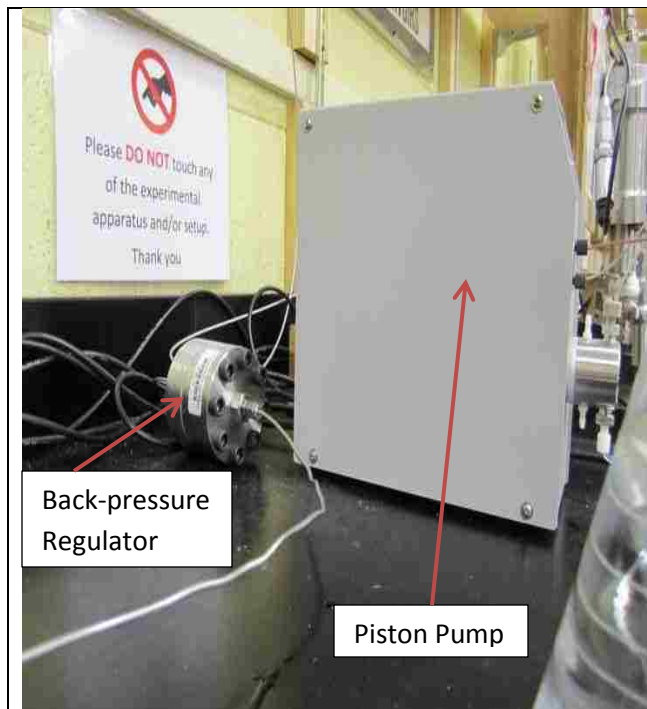


Figure A.8: Back pressure regulator and piston pump connected during experiment



Figure A.9: XRD instrument at the LSU Geology department

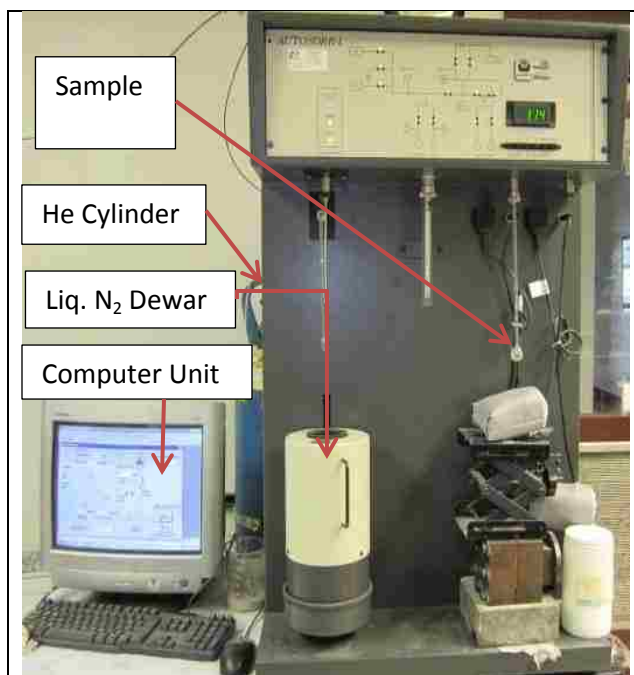


Figure A.10: BET instrument showing liquid nitrogen dewar and sample holder bulbs



Figure A.11: CO₂-brine flooded crushed shale samples after three months

A.2 Preparation of Shale Caprock Samples

The preparation of shale rock samples from the 4-in cores for rock-fluid interaction is outlined below:

1. Carefully selected portions of the cores are cut out using laboratory hammer to break the rock portion out by impact. Three inches thick sections were enough for each sample.
2. The hammer impact process is repeated three to four times. This breaks the rock to four to five chunks.
3. The rock chunks are size reduced/crushed repeatedly with pestles and mortars to sizes ranging between 3mm to 5mm. See figures A.2 and A.3.
4. Samples of similar mineralogy are then mixed together to form the desired ratio of bulk clay to quartz. Samples A, B and C are mixed samples of CEBC5 and CEML5, 2EPR1 and 2EPR4, and 2EBC1 respectively. CEBC5, CEML5, 2EPR1, 2EPR4 and 2EBC1 refers to the original 4-in core samples shown in figure 3.4.
5. The newly mixed experimental samples are charged into the pressure cells and packed tightly with the two ends sealed with the cells' air tight stainless steel covers.
6. 265g each of samples A, B and C are charged into each of the pressure cells.

A.3 Preparation of CO₂-brine Injection Fluid

The preparation of CO₂-brine liquid injected during shale/CO₂-brine flooding is outlined below:

1. 20.196g of Sodium Chloride (NaCl) and 0.345g of Potassium Chloride (KCl) are dissolved in 1liter of distilled/de-ionized water and the mixture stirred for 50mins using magnetic stirrers. This mixture is referred to as brine.
2. The brine is funneled into a stainless steel accumulator and the accumulator is capped afterwards. The head of the cap is connected to a pressurized cylinder containing CO₂.

See figure A.6

3. CO₂ is released from the cylinder into the brine accumulator at a pressure of 25psi for 80mins to ensure equilibrium is reached in the dissolution of CO₂ in brine.
4. The brine accumulator is de-pressurized and the CO₂-brine is collected into a capped glassware for storage and subsequent usage in shale/CO₂-brine flooding experiment.

A.5 Justification of Back-Pressure Value of 970psi

Preliminary information about the capillary entry data was obtained from the analysis of the initial pressure evolution as recorded for each packed cell by National Instruments' Labview data acquisition device shown in figure A.12.

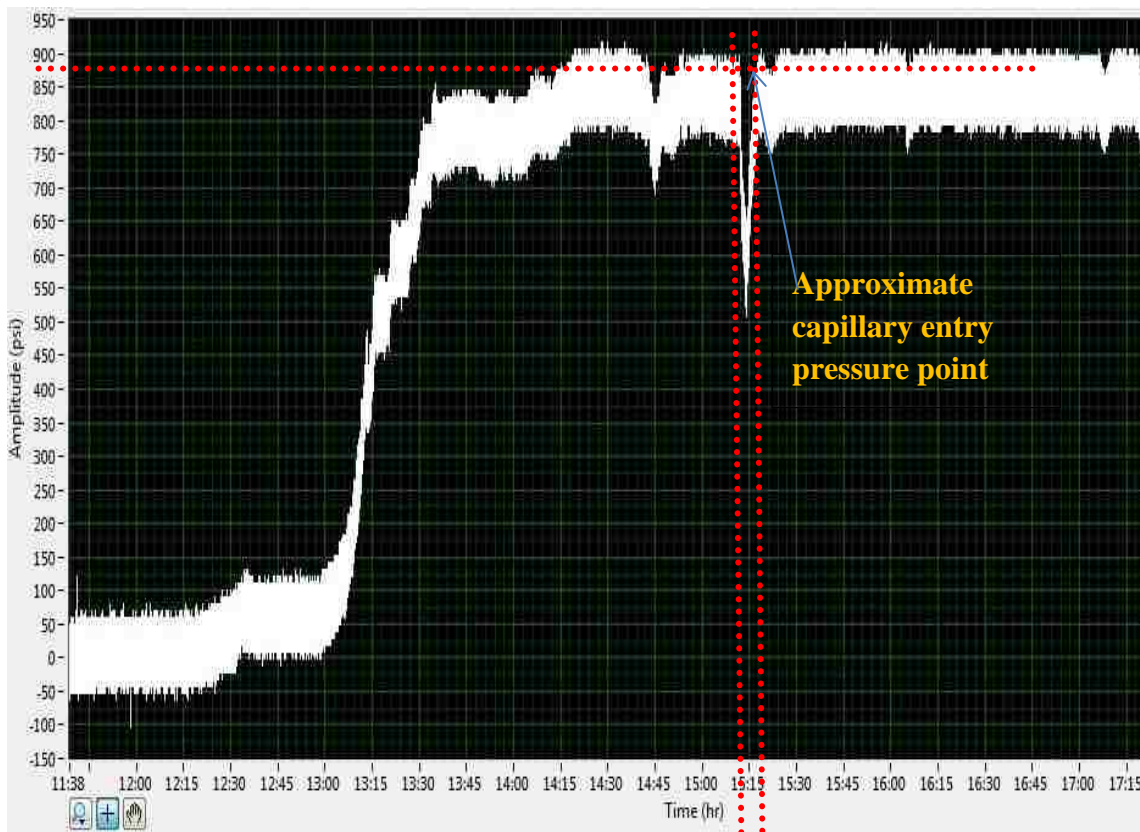


Figure A.12: Pressure evolution plot as captured by National Instrument Labview data acquisition device showing the approximate capillary entry pressure for the shale caprock (sample A)

All the six pressure transducers that were used (two pressure transducers per cell; one in the inlet and one at the outlet) captured the critical points on the graph. The horizontal red line on figure A.12 indicated the approximate capillary entry pressure for the shale caprock while the vertical red lines showed the time at which it was overcome as well as the differential pore space filling time. The value of the back-pressure used during the experiment was set at approximately 70psi above the approximate capillary entry pressure recorded by the logging device (back pressure value of 970psi was used). This was to provide enough driving force for the CO₂-brine to move through the pore spaces of the samples in the cells. The approximate value of capillary entry pressure for the shale rock samples is in agreement with the values reported by Al-Bazali et al., in 2005 using three different mineralogical samples of shale rock (see table 2.1 in Chapter 2) and four capillary-probing fluid (Oil-Based Mud, Decane, Crude-Oil and Nitrogen Gas). The Al-Bazali et al., capillary entry pressure values for shale which are presented in table A.1 ranged between 150 psi and 950 psi.

Table A.1: Measured capillary entry pressure of Pierre, C1 and Arco-China shales using Oil-Based Mud, Decane, Crude Oil and Nitrogen Gas as reported by Al-Bazali et al., 2005 [28]

	Oil-Based Mud	Decane	Crude Oil	Nitrogen Gas
Pierre Shale	150 psi	270 psi	470 psi	630 psi
C1-Shale	250 psi	365 psi	600 psi	700 psi
Arco-China Shale	300 psi	450 psi	750 psi	950 psi

Table A.2 records the approximate values of the capillary entry pressure, pore sizes and pore volume of the samples when considered as a bulk caprock. Literature values of interfacial tension and contact angles were used to arrive at these estimates. Table A.2 also gives

approximate values of pore space properties (such as pore volume and pore size) that could be expected from the application of the BET technique to CO₂-brine flooded shale caprock samples over the three months experimental period. These approximate properties are for individual samples A, B and C. It could be noted that pore sizes are estimated to be in the nanometer range which are typical values for shale caprocks.

Table A.2: Estimated nano-porous shale capillary data using available values of IFT and contact angle for shale/CO₂-brine interaction reported by Daniel and Kaldi, 2009

Samples	Capillary entry pressure (psi)	Capillary fillage time (mins)	Pore volume/gram (ml/g)	Pore Diameter (nm)	Interfacial* Tension (mN/m)	Contact* Angle °	Ratio C:Q:F%
A	880	4.50	0.0051	16.1	24.80	9.0	3:1;1.6
B	900	4.60	0.0052	13.5	21.10	5.0	2:1;2.4
C	875	4.50	0.0051	16.6	25.20	7.0	1:1;5.0
Average	885	4.53	0.0051	15.4	23.7	7.0	

The Washburn expression, equation (27), was used as the correlation expression for the wettability parameters.

$$P_c D_A = 4 \sigma \cos \theta \dots\dots\dots (27)$$

where P_c = capillary entry pressure, D_A = pore throat diameter, σ = interfacial tension, θ = contact angle.

Contact angle and interfacial tension values starred (*) above were obtained from wettability parameters reported by Daniel and Kaldi [25]. In table A.2, C : Q refers to the ratio of bulk clay to quart and F% is the percentage of feldspar in samples A, B and C.

A.5 Detailed Description of Experimental Procedure in Shale Caprock/CO₂-Brine Interaction

Crushed samples of shale caprock are packed tightly and neatly into three 4000psi rated flow cells. There are 3 samples of different mineralogy (samples A, B and C) with each packed into flow cells A, B and C respectively. An inlet header carrying CO₂-brine leads into the 3 cells as well as an outlet header. See figures 3.2 and A.1. After all the experimental set-up parts have been assembled, a back pressure of 970psi is imposed to induce flow through the porous spaces of the rock materials during injection. The pressure inside the cells begins to build up after it is totally filled with CO₂-brine. A flow rate of approximately 0.9ml/min is channeled to the cells from a syringe pump. This floods the external and internal surface area of the shale rock. The injection is continued for 30days after which the cells are depressurized gradually over 4hrs by stopping the pump and bleeding off the dome pressure of the back-pressure regulator. During these 30 days, effluent samples from the bottom outlet of the pressure cells are collected for pH and ICP-OES analysis at room conditions every day. CO₂-brine reacted shale caprock samples are removed once, all together, from the bottom part of the cells for XRD, SEM, EDS and BET analysis. This process is repeated over the next 60 days at interval of 30 days.

APPENDIX B
COLLECTION OF POST-EXPERIMENTAL EFFLUENT AND SELECTION OF CO₂-BRINE REACTED SHALE ROCK FOR ANALYSIS

B.1 Collection of Effluent Liquid for Analysis

1. Effluent samples are collected every day from the singular outlet of the connected flow cells using 1800ml sealed conical beakers. 50ml of the effluent is collected and stored separately in environmental bottles for ICP-OES analysis.
2. The remaining bulk of effluent is tested for pH using digital meters. Remainder of effluent is disposed of according to LSU policy.
3. The effluent liquid is agitated using magnetic mixers before pH measurements and ICP-OES liquid samples are obtained.
4. Precipitate which formed after pH and ICP-OES analyses are filtered out of the solution for XRD, SEM and EDS analyses.

B.2 Sample Selection of CO₂-Brine Reacted Shale Rocks

1. After each month (1st month, 2nd month and 3rd month) of the continuous CO₂-brine contact experiment on the crushed shale rocks, the cells are depressurized and allowed to drain completely over several hours (3hours to 5hours).
2. The inlet and outlet CO₂-brine headers of the cells are removed. The cells are then positioned such that the bottom parts are accessible.
3. The lid of the bottom section of the cells (see figure G.1) are removed and approximately 40g of the CO₂-brine contacted shale rock samples from cells A, B and C are taken out for SEM, EDS, XRD and BET analysis.

B.3 Sample Selection and Preparation for SEM and EDS Analysis

Three to four pebbles of each of the CO₂-brine contacted samples, after each month, are put out separately and air dried.

1. The preferred samples are flat platelet-like specimen
2. They are later kept in environmental bottles for SEM analysis at the earliest chance
3. The same samples are used for EDS analysis

B.4 Sample selection and Preparation for XRD analysis

1. 10g of each of the CO₂-brine reacted samples, after each month, are put out separately and later crushed into powder.
2. The samples are micronized using glycol and micro-agitator.
3. The fine samples are filtered using centrifuge and vacuum suction.
4. The samples are placed in oven over night to dry completely and XRD analysis is run

B.5 Sample selection and Preparation for BET Analysis

1. A total of 26g of each of the CO₂-brine reacted samples are taken apart for BET analysis
2. The samples are loaded into the BET equipment specimen holding bulb for vacuum drying at 100 degrees Celsius.
3. After the samples have been bone dried, they are blanketed with helium to prevent the re-entry of air into the samples.
4. The samples are transferred to the liquid nitrogen port for 40 points adsorption-desorption process

**APPENDIX C
pH DATASHEET**

Table C.1: pH datasheet (A)

Day	Initial pH	Final pH
1	4.09	7.73
2	4.11	8.28
3	4.03	7.09
4	3.98	7.1
5	3.86	7.05
6	3.86	6.45
7	3.81	6.36
8	3.88	6.19
9	3.81	6.21
10	3.81	6.36
11	3.84	6.98
12	3.84	6.42
13	3.82	6.39
14	3.89	6.36
15	3.91	6.12
16	3.85	6.09
17	3.95	5.85
18	3.93	5.65
19	3.95	5.67
20	3.89	5.82
21	3.91	5.9
22	3.91	6.13
23	3.91	6.05
24	3.92	6.21
25	3.91	6.42
26	3.9	6.37
27	3.9	6.08
28	3.91	6.42
29	3.89	6.51
30	3.89	6.56
31	3.9	6.55
32	3.91	6.55
33	3.92	6.56
34	4.01	6.48
35	3.99	6.49

Table C.2: pH datasheet (B)

Day	Initial pH	Final pH
36	3.9	6.47
37	3.89	6.53
38	3.95	6.54
39	3.96	6.55
40	3.95	6.51
41	3.92	6.52
42	3.91	6.71
43	3.93	6.44
44	3.91	6.49
45	3.81	6.19
46	3.81	6.46
47	3.96	6.46
48	3.91	6.49
49	3.91	6.57
50	3.92	6.53
51	3.94	6.12
52	3.93	6.31
53	3.91	6.5
54	3.89	6.44
55	3.81	6.49
56	3.9	5.99
57	3.94	6.39
58	3.92	6.49
59	3.92	6.52
60	3.91	6.48
61	3.93	6.39
62	3.88	6.35
63	3.88	6.11
64	3.89	6.31
65	3.91	6.11
66	3.9	6.23
67	3.99	6.18
68	3.89	6.1
69	3.92	5.99
70	3.92	5.91

Table C.3: pH datasheet (C)

Day	Initial pH	Final pH
71	3.91	5.79
72	3.92	5.77
73	3.93	5.69
74	3.82	5.64
75	3.82	5.36
76	3.81	5.55
77	3.88	5.49
78	3.89	5.43
79	3.89	5.41
80	3.91	5.32
81	3.92	5.34
82	3.91	5.26
83	3.9	5.28
84	3.89	5.1
85	3.88	5.31
86	3.88	5.08
87	3.88	5.02
88	3.92	5.03
89	3.94	5.01
90	3.93	5.22
91	3.85	5.03
92	3.85	5.06
AVR	3.91	6.12

Effluent sample and pH measurements were collected 9am every morning. 25 ml of effluent sample were stored each day.

APPENDIX D
ICP-OES DATASHEET

Table D: ICP-OES datasheet for cations present in effluent solution

Sample Number	Ca²⁺	Fe^{2+/3+}	K⁺	Mg²⁺	Mn²⁺	Al³⁺	Na⁺	Si²⁺
0	0.32	0.20	145.5	0.10	0.00	0.61	1851.0	1.50
1	21.5	0.00	238.5	5.70	0.40	0.69	4341.0	1.50
2	58.3	0.20	186.0	18.80	0.30	0.67	4167.0	2.70
3	34.6	0.00	247.2	14.70	1.20	0.63	4422.0	1.60
4	37.1	0.00	252.9	16.20	1.40	0.70	4683.0	1.70
5	30.7	0.10	240.6	13.60	1.30	0.56	4395.0	1.50
6	30.0	0.00	246.3	13.70	1.40	0.63	4383.0	1.20
7	22.6	2.60	247.5	10.50	1.30	0.65	4374.0	1.60
8	23.7	0.00	238.8	10.80	1.30	0.64	4404.0	1.80
9	17.0	0.10	193.8	8.00	1.00	0.61	3327.0	3.10
10	16.6	0.20	148.2	8.00	1.10	0.65	2235.0	5.30
11	10.00	0.05	224.0	5.48	1.05	0.60	3536.0	1.73
12	8.10	0.11	226.0	4.89	0.78	0.50	3572.0	1.67
13	6.73	0.30	217.0	4.32	0.66	0.55	3472.0	1.78
14	5.88	0.00	222.0	3.91	0.60	0.56	3528.0	1.72
15	5.93	0.00	230.0	3.94	0.60	0.50	3444.0	1.62
16	5.18	0.00	227.0	3.64	0.55	0.59	3492.0	1.57
17	5.04	0.00	223.0	3.61	0.57	0.55	3508.0	1.50
18	4.92	0.00	223.0	3.58	0.59	0.46	3468.0	1.31
19	4.73	0.00	218.0	3.53	0.59	0.59	3412.0	1.31
20	3.60	0.00	217.0	3.04	0.54	0.59	3372.0	1.23
21	0.00	0.00	224.0	0.82	0.26	0.46	3440.0	0.75
22	2.95	0.00	234.0	0.80	0.23	0.44	3404.0	0.82
23	2.35	0.00	227.0	2.18	0.36	0.55	3416.0	0.82
24	2.12	0.00	224.0	2.03	0.33	0.50	3412.0	0.84
25	2.27	0.00	242.0	2.02	0.32	0.51	3504.0	0.82
26	3.05	0.00	240.0	1.96	0.31	0.50	3448.0	0.83
27	1.48	0.00	236.0	1.83	0.29	0.55	3504.0	1.08
28	3.14	0.00	228.0	1.86	0.29	0.59	3468.0	0.82
29	1.04	0.00	226.0	1.61	0.26	0.57	3444.0	0.75
30	1.00	0.07	228.0	1.49	0.25	0.50	3536.0	0.72

APPENDIX E
SCANNING ELECTRON MICROSCOPY IMAGE OF SHALE CAPROCK SAMPLE

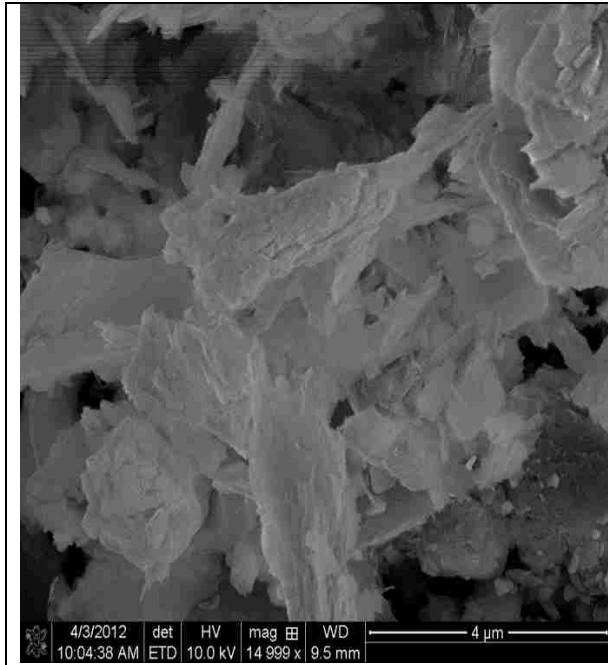


Figure E.1: SEM image for sample A after 1 month of CO₂-brine flooding

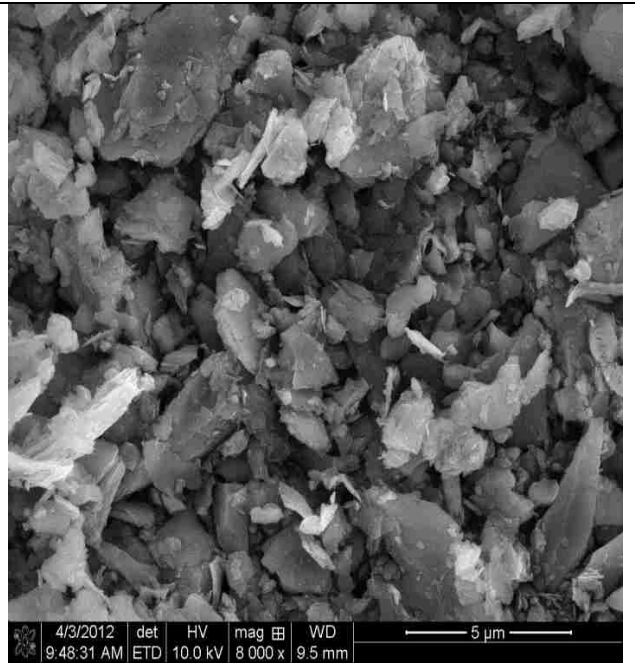


Figure E.2: SEM image for sample B after 1 month of CO₂-brine flooding

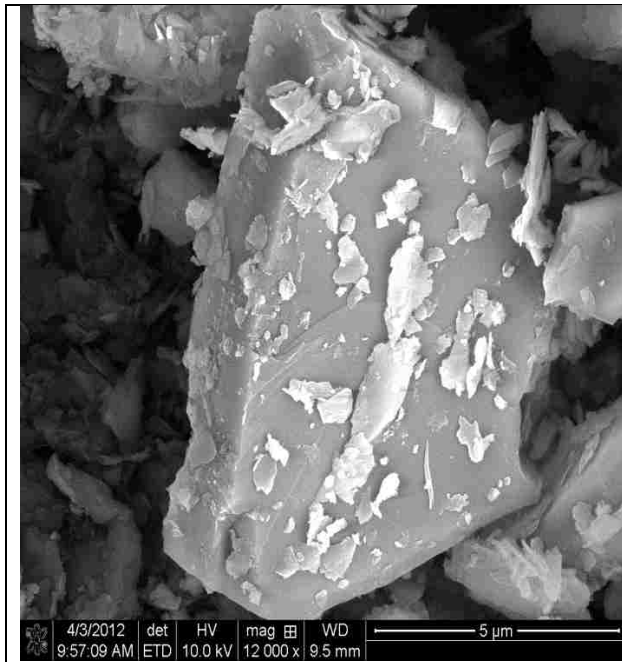


Figure E.3: SEM image for sample C after 1 month of CO₂-brine flooding

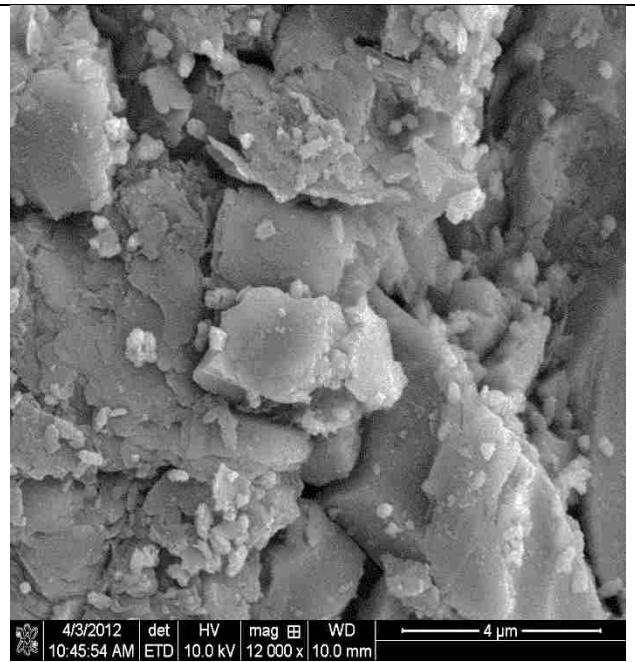


Figure E.4: SEM image for sample A after 3 months of CO₂-brine flooding

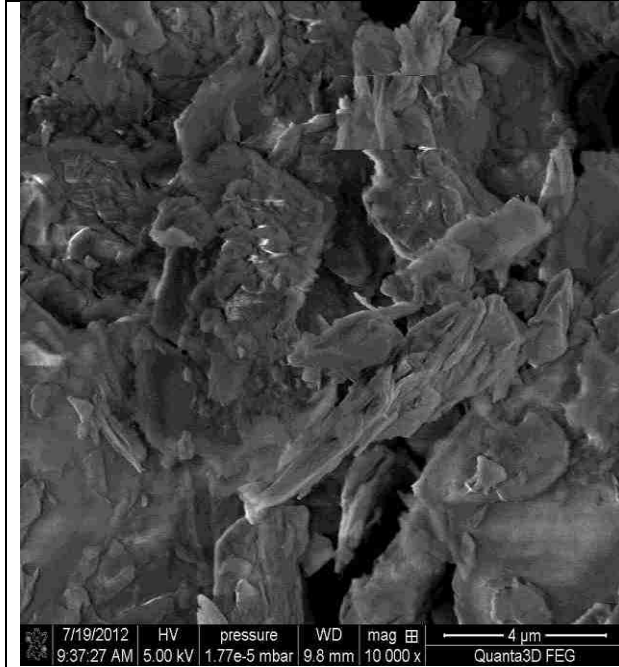


Figure E.5: SEM image for sample B after 2 month of CO₂-brine flooding

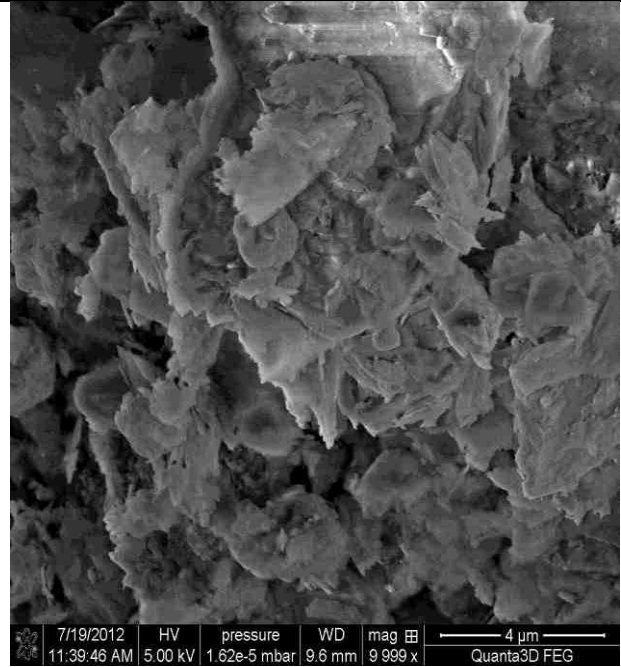


Figure E.6: SEM image for sample B after 2 month of CO₂-brine flooding

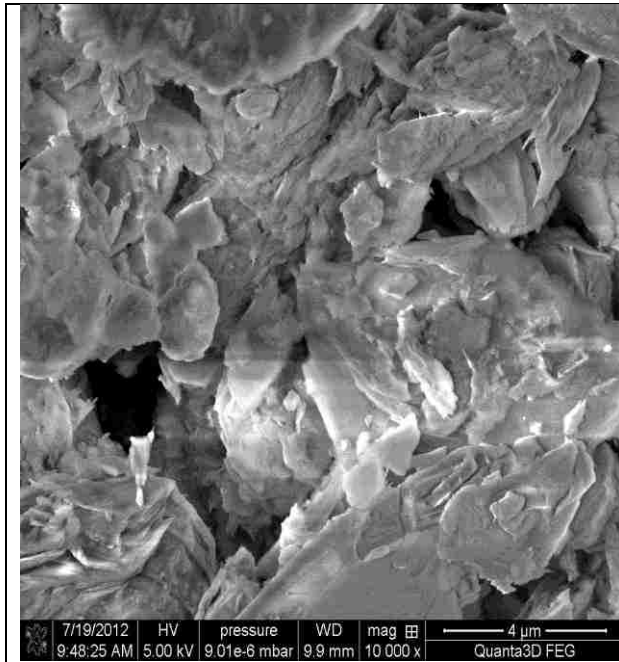


Figure E.7: SEM image for sample C after 2 month of CO₂-brine flooding



Figure E. 8: Optical Microscopy image of thin section cut for control sample A showing pore networks

**APPENDIX F
BET NITROGEN ADSORPTION DATASHEET**

F.1 SAMPLE A; CONTROL

Date: 04/21/2012

Quantachrome Corporation
Quantachrome Autosorb Automated Gas Sorption System Report
Autosorb for Windows® Version 1.19

Sample ID Abiola1
Description ShaleCon1
Comments
Sample Weight 0.8010 g
Adsorbate NITROGEN Operator Abiola Cross-Sec Area 16.2 Å²/molec Outgas
Time 0.5 hrs Analysis Time 238.1 min NonIdeality 6.580E-05 P/Po Toler 5 End
of Run 04/09/2012 22:06 Molecular Wt 28.0134 g/mol Equil Time 2 File Name
EABI1CLRAW Station # 1 Bath Temp. 77.35 °C

AREA-VOLUME-PORE SIZE SUMMARY

SURFACE AREA DATA

Multipoint BET..... 6.442E+00 m²/g
BJH Method Cumulative Desorption Surface Area..... 8.093E+00 m²/g
DH Method Cumulative Desorption Surface Area..... 8.231E+00 m²/g
DR Method Micro Pore Area..... 9.202E+00 m²/g

PORE VOLUME DATA

Total Pore Volume for pores with Diameter
less than 5248.2 Å at P/Po = 0.99634..... 1.260E-02 cc/g
BJH Method Cumulative Desorption Pore Volume..... 1.264E-02 cc/g
DH Method Cumulative Desorption Pore Volume..... 1.239E-02 cc/g
DR Method Micro Pore Volume..... 3.270E-03 cc/g
HK Method Cumulative Pore Volume..... 2.635E-03 cc/g
SF Method Cumulative Pore Volume..... 2.691E-03 cc/g

PORE SIZE DATA

Average Pore Diameter..... 7.822E+01 Å
BJH Method Desorption Pore Diameter (Mode)..... 3.793E+01 Å
DH Method Desorption Pore Diameter (Mode)..... 3.793E+01 Å
DR Method Micro Pore Width 1.156E+02 Å
DA Method Pore Diameter (Mode)..... 1.780E+01 Å

HK Method Pore Width (Mode)..... 1.552E+01 Å
 SF Method Pore Diameter (Mode)..... 2.934E+01 Å

Table F.1: BET desorption pore size distribution for control specimen of sample A

Diameter	Pore Vol	Pore Surf Area	Dv(d)	Ds(d)	Dv(logd)	Ds(logd)
Å	[cc/g]	[m ² /g]	cc/ Å /g	[m ² /Å/g]	[cc/g]	[m ² /g]
13.45	0.00E+00	0.00E+00	0.00E+00	0.00E+00	0.00E+00	0.00E+00
16.19	0.00E+00	0.00E+00	0.00E+00	0.00E+00	0.00E+00	0.00E+00
18.65	0.00E+00	0.00E+00	0.00E+00	0.00E+00	0.00E+00	0.00E+00
21.15	0.00E+00	0.00E+00	0.00E+00	0.00E+00	0.00E+00	0.00E+00
23.77	5.55E-05	9.34E-02	2.06E-05	3.47E-02	1.13E-03	1.90E+00
26.58	1.66E-04	2.60E-01	3.78E-05	5.68E-02	2.31E-03	3.48E+00
29.74	2.86E-04	4.21E-01	3.53E-05	4.75E-02	2.41E-03	3.25E+00
33.67	6.65E-04	8.71E-01	8.48E-05	1.01E-01	6.56E-03	7.79E+00
37.93	2.59E-03	2.91E+00	4.76E-04	5.01E-01	4.15E-02	4.38E+01
42.36	3.95E-03	4.19E+00	2.83E-04	2.67E-01	2.76E-02	2.60E+01
47.96	4.76E-03	4.86E+00	1.26E-04	1.05E-01	1.39E-02	1.16E+01
55.15	5.77E-03	5.59E+00	1.27E-04	9.24E-02	1.61E-02	1.17E+01
64.53	6.88E-03	6.28E+00	1.03E-04	6.37E-02	1.52E-02	9.44E+00
76.68	8.30E-03	7.02E+00	1.05E-04	5.50E-02	1.86E-02	9.68E+00
92.97	9.52E-03	7.55E+00	6.39E-05	2.75E-02	1.36E-02	5.87E+00
117.29	1.04E-02	7.85E+00	3.03E-05	1.03E-02	8.15E-03	2.78E+00
159.96	1.11E-02	8.02E+00	1.18E-05	2.94E-03	4.28E-03	1.07E+00
287.48	1.15E-02	8.08E+00	2.14E-06	2.97E-04	1.36E-03	1.89E-01
2817.66	1.26E-02	8.09E+00	2.34E-07	3.32E-06	1.01E-03	1.43E-02

F.2 SAMPLE A; MONTH 1

Date: 04/26/2012

Quantachrome Corporation
Quantachrome Autosorb Automated Gas Sorption System Report
Autosorb for Windows® Version 1.19

Sample ID Abiola1a
Description ShaleSamp3
Comments
Sample Weight 0.9130 g
Adsorbate NITROGEN Operator Abiola Cross-Sec Area 16.2 Å²/molec Outgas
Time 0.5 hrs Analysis Time 262.2 min NonIdeality 6.580E-05 P/Po Toler 5 End
of Run 04/13/2012 09:11 Molecular Wt 28.0134 g/mol Equil Time 2 File Name
EABI1AIRAW Station # 1 Bath Temp. 77.35 °C

AREA-VOLUME-PORE SIZE SUMMARY

SURFACE AREA DATA

Multipoint BET..... 7.233E+00 m²/g
BJH Method Cumulative Desorption Surface Area..... 8.580E+00 m²/g
DH Method Cumulative Desorption Surface Area..... 8.682E+00 m²/g
DR Method Micro Pore Area..... 1.019E+01 m²/g

PORE VOLUME DATA

Total Pore Volume for pores with Diameter
less than 5120.2 Å at P/Po = 0.99625..... 1.529E-02 cc/g
BJH Method Cumulative Desorption Pore Volume..... 1.525E-02 cc/g
DH Method Cumulative Desorption Pore Volume..... 1.491E-02 cc/g
DR Method Micro Pore Volume..... 3.621E-03 cc/g
HK Method Cumulative Pore Volume..... 2.953E-03 cc/g
SF Method Cumulative Pore Volume..... 3.020E-03 cc/g

PORE SIZE DATA

Average Pore Diameter..... 8.455E+01 Å
BJH Method Desorption Pore Diameter (Mode)..... 3.822E+01 Å
DH Method Desorption Pore Diameter (Mode)..... 3.822E+01 Å
DR Method Micro Pore Width 1.104E+02 Å
DA Method Pore Diameter (Mode)..... 1.780E+01 Å
HK Method Pore Width (Mode)..... 1.502E+01 Å
SF Method Pore Diameter (Mode)..... 2.824E+01 Å

Table F.2: BET desorption pore size distribution for 1 month CO₂-brine flooded specimen of sample A

Diameter	Pore Vol	Pore Surf Area	Dv(d)	Ds(d)	Dv(logd)	Ds(logd)
Å	[cc/g]	[m²/g]	cc/Å/g	[m²/Å/g]	[cc/g]	[m²/g]
13.51	0.00E+00	0.00E+00	0.00E+00	0.00E+00	0.00E+00	0.00E+00
16.24	0.00E+00	0.00E+00	0.00E+00	0.00E+00	0.00E+00	0.00E+00
18.7	2.83E-05	6.04E-02	1.15E-05	2.46E-02	4.94E-04	1.06E+00
21.19	8.36E-05	1.65E-01	2.20E-05	4.15E-02	1.07E-03	2.02E+00
23.8	1.59E-04	2.91E-01	2.79E-05	4.69E-02	1.53E-03	2.57E+00
26.63	2.86E-04	4.82E-01	4.29E-05	6.44E-02	2.63E-03	3.95E+00
29.82	4.75E-04	7.36E-01	5.51E-05	7.39E-02	3.78E-03	5.07E+00
33.94	7.89E-04	1.11E+00	6.54E-05	7.71E-02	5.10E-03	6.02E+00
38.22	3.13E-03	3.55E+00	6.23E-04	6.52E-01	5.48E-02	5.73E+01
42.39	4.40E-03	4.76E+00	2.78E-04	2.62E-01	2.71E-02	2.56E+01
47.9	5.07E-03	5.31E+00	1.03E-04	8.64E-02	1.14E-02	9.51E+00
55.18	5.83E-03	5.86E+00	9.33E-05	6.77E-02	1.18E-02	8.58E+00
64.61	6.80E-03	6.47E+00	9.13E-05	5.65E-02	1.36E-02	8.39E+00
77.4	7.95E-03	7.06E+00	7.72E-05	3.99E-02	1.37E-02	7.09E+00
95.58	9.29E-03	7.62E+00	6.21E-05	2.60E-02	1.36E-02	5.69E+00
124.04	1.07E-02	8.08E+00	4.00E-05	1.29E-02	1.13E-02	3.66E+00
171.38	1.21E-02	8.41E+00	2.38E-05	5.56E-03	9.31E-03	2.17E+00
273.56	1.31E-02	8.55E+00	6.77E-06	9.90E-04	4.16E-03	6.08E-01
2733.16	1.53E-02	8.58E+00	4.50E-07	6.59E-06	1.84E-03	2.69E-02

F.3 SAMPLE A; MONTH 2

Date: 05/20/2012

Quantachrome Corporation
Quantachrome Autosorb Automated Gas Sorption System Report
Autosorb for Windows® Version 1.19

Sample ID Abiola1B
Description AbiolaShale3B
Comments
Sample Weight 1.2000 g
Adsorbate NITROGEN Operator Abiola Cross-Sec Area 16.2 Å²/molec Outgas
Time 0.5 hrs Analysis Time 262.2 min NonIdeality 6.580E-05 P/Po Toler 5
End of Run 05/18/2012 07:58 Molecular Wt 28.0134 g/mol Equil Time 2 File Name
EABI1B1.RAW Station # 1 Bath Temp. 77.35 °C

AREA-VOLUME-PORE SIZE SUMMARY

SURFACE AREA DATA

Multipoint BET..... 7.966E+00 m²/g
BJH Method Cumulative Desorption Surface Area..... 8.891E+00 m²/g
DH Method Cumulative Desorption Surface Area..... 8.965E+00 m²/g
DR Method Micro Pore Area..... 1.156E+01 m²/g

PORE VOLUME DATA

Total Pore Volume for pores with Diameter
less than 2466.6 Å at P/Po = 0.99217..... 1.591E-02 cc/g
BJH Method Cumulative Desorption Pore Volume..... 1.568E-02 cc/g
DH Method Cumulative Desorption Pore Volume..... 1.534E-02 cc/g
DR Method Micro Pore Volume..... 4.110E-03 cc/g
HK Method Cumulative Pore Volume..... 3.331E-03 cc/g
SF Method Cumulative Pore Volume..... 3.400E-03 cc/g

PORE SIZE DATA

Average Pore Diameter..... 7.990E+01 Å
BJH Method Desorption Pore Diameter (Mode)..... 3.760E+01 Å
DH Method Desorption Pore Diameter (Mode)..... 3.760E+01 Å
DR Method Micro Pore Width 1.141E+02 Å
DA Method Pore Diameter (Mode)..... 1.780E+01 Å
HK Method Pore Width (Mode)..... 1.538E+01 Å
SF Method Pore Diameter (Mode)..... 2.888E+01 Å

Table F.3: BET desorption pore size distribution for 2-month CO₂-brine flooded specimen of sample A

Diameter	Pore Vol	Pore Surf Area	Dv(d)	Ds(d)	Dv(logd)	Ds(logd)
Å	[cc/g]	[m²/g]	cc/ Å /g	[m²/Å/g]	[cc/g]	[m²/g]
13.61	7.15E-05	2.10E-01	2.41E-05	7.09E-02	7.54E-04	2.21E+00
16.31	1.28E-04	3.48E-01	2.32E-05	5.69E-02	8.69E-04	2.13E+00
18.76	2.04E-04	5.10E-01	3.09E-05	6.59E-02	1.33E-03	2.84E+00
21.25	3.08E-04	7.07E-01	4.15E-05	7.81E-02	2.03E-03	3.82E+00
23.85	4.34E-04	9.18E-01	4.69E-05	7.86E-02	2.57E-03	4.31E+00
26.67	5.68E-04	1.12E+00	4.56E-05	6.83E-02	2.80E-03	4.19E+00
29.83	6.91E-04	1.28E+00	3.62E-05	4.86E-02	2.49E-03	3.33E+00
33.32	1.01E-03	1.67E+00	8.97E-05	1.08E-01	6.87E-03	8.25E+00
37.6	3.55E-03	4.37E+00	5.09E-04	5.42E-01	4.40E-02	4.69E+01
42.5	4.52E-03	5.28E+00	2.01E-04	1.89E-01	1.96E-02	1.85E+01
48.08	5.19E-03	5.83E+00	1.06E-04	8.80E-02	1.17E-02	9.72E+00
55.27	5.86E-03	6.32E+00	8.39E-05	6.08E-02	1.07E-02	7.72E+00
64.64	6.59E-03	6.77E+00	6.82E-05	4.22E-02	1.01E-02	6.26E+00
77.51	7.47E-03	7.23E+00	5.86E-05	3.02E-02	1.04E-02	5.38E+00
96.62	8.50E-03	7.66E+00	4.44E-05	1.84E-02	9.83E-03	4.07E+00
123.06	9.78E-03	8.07E+00	4.29E-05	1.40E-02	1.21E-02	3.93E+00
170.63	1.19E-02	8.56E+00	3.21E-05	7.53E-03	1.25E-02	2.92E+00
291.35	1.39E-02	8.84E+00	1.16E-05	1.59E-03	7.53E-03	1.03E+00
1423	1.57E-02	8.89E+00	8.46E-07	2.38E-05	2.17E-03	6.11E-02

F.4 SAMPLE A; MONTH 3

Date: 06/19/2012

Quantachrome Corporation
Quantachrome Autosorb Automated Gas Sorption System Report
Autosorb for Windows® Version 1.19

Sample ID Shale1D
Description ReactedShale 1D
Comments
Sample Weight 1.4000 g
Adsorbate NITROGEN Operator Abiola Cross-Sec Area 16.2 Å²/molec Outgas
Time 0.5 hrs Analysis Time 301.7 min NonIdeality 6.580E-05 P/Po Toler 5 End
of Run 06/19/2012 18:56 Molecular Wt 28.0134 g/mol Equil Time 2 File Name
SHALE1D.RAW Station # 1 Bath Temp. 77.35 °C

AREA-VOLUME-PORE SIZE SUMMARY

SURFACE AREA DATA

Multipoint BET.....	8.731E+00	m ² /g
BJH Method Cumulative Desorption Surface Area.....	8.316E+00	m ² /g
DH Method Cumulative Desorption Surface Area.....	8.393E+00	m ² /g
DR Method Micro Pore Area.....	1.177E+01	m ² /g

PORE VOLUME DATA

Total Pore Volume for pores with Diameter
less than 3866.8 Å at P/Po = 0.99502..... 1.968E-02 cc/g

BJH Method Cumulative Desorption Pore Volume.....	1.691E-02	cc/g
DH Method Cumulative Desorption Pore Volume.....	1.652E-02	cc/g
DR Method Micro Pore Volume.....	4.182E-03	cc/g
HK Method Cumulative Pore Volume.....	3.198E-03	cc/g
SF Method Cumulative Pore Volume.....	3.302E-03	cc/g

PORE SIZE DATA

Average Pore Diameter.....	9.015E+01	Å
BJH Method Desorption Pore Diameter (Mode).....	3.820E+01	Å
DH Method Desorption Pore Diameter (Mode).....	3.820E+01	Å
DR Method Micro Pore Width	1.264E+02	Å
DA Method Pore Diameter (Mode).....	1.840E+01	Å
HK Method Pore Width (Mode).....	1.533E+01	Å
SF Method Pore Diameter (Mode).....	2.888E+01	Å

Table F.4: BET desorption pore size distribution for 3 month CO₂-brine flooded specimen of sample A

Diameter	Pore Vol	Pore Surf Area	Dv(d)	Ds(d)	Dv(logd)	Ds(logd)
Å	[cc/g]	[m²/g]	cc/ Å /g	[m²/Å/g]	[cc/g]	[m²/g]
13.94	5.82E-05	1.67E-01	2.06E-05	5.92E-02	6.60E-04	1.89E+00
16.44	1.73E-04	4.46E-01	5.26E-05	1.28E-01	1.99E-03	4.84E+00
18.76	3.14E-04	7.47E-01	5.75E-05	1.23E-01	2.48E-03	5.29E+00
21.24	4.54E-04	1.01E+00	5.59E-05	1.05E-01	2.73E-03	5.14E+00
23.82	5.73E-04	1.21E+00	4.47E-05	7.50E-02	2.45E-03	4.11E+00
26.66	6.29E-04	1.30E+00	1.87E-05	2.81E-02	1.15E-03	1.72E+00
29.93	7.91E-04	1.51E+00	4.58E-05	6.12E-02	3.16E-03	4.22E+00
34.06	1.23E-03	2.03E+00	9.35E-05	1.10E-01	7.32E-03	8.60E+00
38.2	3.11E-03	4.00E+00	5.32E-04	5.57E-01	4.68E-02	4.90E+01
42.41	3.90E-03	4.74E+00	1.60E-04	1.51E-01	1.56E-02	1.47E+01
48.02	4.37E-03	5.14E+00	7.57E-05	6.31E-02	8.36E-03	6.96E+00
55.25	4.96E-03	5.56E+00	7.18E-05	5.20E-02	9.12E-03	6.60E+00
64.79	5.65E-03	5.98E+00	6.29E-05	3.88E-02	9.35E-03	5.78E+00
77.26	6.51E-03	6.43E+00	6.18E-05	3.20E-02	1.10E-02	5.68E+00
92.46	7.37E-03	6.80E+00	5.26E-05	2.28E-02	1.12E-02	4.83E+00
121.6	9.13E-03	7.38E+00	4.19E-05	1.38E-02	1.16E-02	3.82E+00
179.68	1.16E-02	7.93E+00	3.32E-05	7.39E-03	1.35E-02	3.01E+00
289.61	1.40E-02	8.26E+00	1.64E-05	2.27E-03	1.07E-02	1.48E+00
2114.62	1.69E-02	8.32E+00	8.34E-07	1.58E-05	2.84E-03	5.37E-02

F.5 SAMPLE B; CONTROL

Date: 04/25/2012

Quantachrome Corporation
Quantachrome Autosorb Automated Gas Sorption System Report
Autosorb for Windows® Version 1.19

Sample ID Abiola2c
Description ShaleCon2
Comments
Sample Weight 0.8320 g
Adsorbate NITROGEN Operator Abiola Cross-Sec Area 16.2 Å²/molec Outgas
Time 0.5 hrs Analysis Time 235.8 min NonIdeality 6.580E-05 P/Po Toler 5 End
of Run 04/12/2012 08:13 Molecular Wt 28.0134 g/mol Equil Time 2 File Name
EABI2CI.RAW Station # 1 Bath Temp. 77.35 °C

AREA-VOLUME-PORE SIZE SUMMARY

SURFACE AREA DATA

Multipoint BET..... 9.576E+00 m²/g
BJH Method Cumulative Desorption Surface Area..... 1.153E+01 m²/g
DH Method Cumulative Desorption Surface Area..... 1.165E+01 m²/g
DR Method Micro Pore Area..... 1.347E+01 m²/g

PORE VOLUME DATA

Total Pore Volume for pores with Diameter
less than 4571.6 Å at P/Po = 0.99580..... 1.883E-02 cc/g
BJH Method Cumulative Desorption Pore Volume..... 1.886E-02 cc/g
DH Method Cumulative Desorption Pore Volume..... 1.846E-02 cc/g
DR Method Micro Pore Volume..... 4.786E-03 cc/g
HK Method Cumulative Pore Volume..... 3.882E-03 cc/g
SF Method Cumulative Pore Volume..... 3.971E-03 cc/g

PORE SIZE DATA

Average Pore Diameter..... 7.864E+01 Å
BJH Method Desorption Pore Diameter (Mode)..... 3.767E+01 Å
DH Method Desorption Pore Diameter (Mode)..... 3.767E+01 Å
DR Method Micro Pore Width 1.119E+02 Å
DA Method Pore Diameter (Mode)..... 1.780E+01 Å
HK Method Pore Width (Mode)..... 1.542E+01 Å
SF Method Pore Diameter (Mode)..... 2.907E+01 Å

Table F.5: BET desorption pore size distribution for control specimen of sample B

Diameter	Pore Vol	Pore Surf Area	Dv(d)	Ds(d)	Dv(logd)	Ds(logd)
Å	[cc/g]	[m²/g]	cc/ Å /g	[m²/Å/g]	[cc/g]	[m²/g]
13.6	0.00E+00	0.00E+00	0.00E+00	0.00E+00	0.00E+00	0.00E+00
16.3	1.18E-05	2.89E-02	4.88E-06	1.20E-02	1.83E-04	4.48E-01
18.74	7.25E-05	1.59E-01	2.48E-05	5.29E-02	1.07E-03	2.28E+00
21.23	1.79E-04	3.59E-01	4.19E-05	7.90E-02	2.05E-03	3.86E+00
23.82	2.79E-04	5.26E-01	3.77E-05	6.32E-02	2.06E-03	3.46E+00
26.63	3.14E-04	5.79E-01	1.18E-05	1.77E-02	7.23E-04	1.09E+00
29.79	4.43E-04	7.53E-01	3.86E-05	5.19E-02	2.65E-03	3.55E+00
33.29	7.70E-04	1.15E+00	8.96E-05	1.08E-01	6.87E-03	8.25E+00
37.67	4.44E-03	5.05E+00	7.21E-04	7.66E-01	6.24E-02	6.63E+01
42.49	6.06E-03	6.57E+00	3.56E-04	3.35E-01	3.48E-02	3.28E+01
48.07	6.93E-03	7.29E+00	1.31E-04	1.09E-01	1.45E-02	1.21E+01
55.5	7.98E-03	8.05E+00	1.27E-04	9.12E-02	1.61E-02	1.16E+01
65.18	9.32E-03	8.87E+00	1.22E-04	7.46E-02	1.82E-02	1.12E+01
77.99	1.10E-02	9.74E+00	1.16E-04	5.94E-02	2.07E-02	1.06E+01
96.13	1.27E-02	1.04E+01	7.77E-05	3.23E-02	1.71E-02	7.13E+00
123.32	1.44E-02	1.10E+01	5.29E-05	1.72E-02	1.49E-02	4.85E+00
170.22	1.59E-02	1.13E+01	2.36E-05	5.54E-03	9.13E-03	2.15E+00
269.92	1.69E-02	1.15E+01	7.75E-06	1.15E-03	4.71E-03	6.98E-01
2455.32	1.89E-02	1.15E+01	4.54E-07	7.40E-06	1.70E-03	2.77E-02

F.6 SAMPLE B; MONTH 1

Date: 04/26/2012

Quantachrome Corporation
Quantachrome Autosorb Automated Gas Sorption System Report
Autosorb for Windows® Version 1.19

Sample ID Abiola2a
Description ShaleSamp2a
Comments
Sample Weight 0.9090 g
Adsorbate NITROGEN Operator Abiola Cross-Sec Area 16.2 Å²/molec Outgas
Time 0.5 hrs Analysis Time 293.0 min NonIdeality 6.580E-05 P/Po Toler 5 End
of Run 04/13/2012 15:38 Molecular Wt 28.0134 g/mol Equil Time 2 File Name
EABI2AIRAW Station # 1 Bath Temp. 77.35 °C

AREA-VOLUME-PORE SIZE SUMMARY

SURFACE AREA DATA

Multipoint BET..... 1.082E+01 m²/g
BJH Method Cumulative Desorption Surface Area..... 1.249E+01 m²/g
DH Method Cumulative Desorption Surface Area..... 1.260E+01 m²/g
DR Method Micro Pore Area..... 1.562E+01 m²/g

PORE VOLUME DATA

Total Pore Volume for pores with Diameter
less than 2146.5 Å at P/Po = 0.99098..... 2.016E-02 cc/g
BJH Method Cumulative Desorption Pore Volume..... 1.989E-02 cc/g
DH Method Cumulative Desorption Pore Volume..... 1.946E-02 cc/g
DR Method Micro Pore Volume..... 5.552E-03 cc/g
HK Method Cumulative Pore Volume..... 4.486E-03 cc/g
SF Method Cumulative Pore Volume..... 4.581E-03 cc/g

PORE SIZE DATA

Average Pore Diameter..... 7.451E+01 Å
BJH Method Desorption Pore Diameter (Mode)..... 3.770E+01 Å
DH Method Desorption Pore Diameter (Mode)..... 3.770E+01 Å
DR Method Micro Pore Width 1.150E+02 Å
DA Method Pore Diameter (Mode)..... 1.780E+01 Å
HK Method Pore Width (Mode)..... 1.533E+01 Å
SF Method Pore Diameter (Mode)..... 2.888E+01 Å

Table F.6: BET desorption pore size distribution for 1-month CO₂-brine flooded specimen of sample B

Diameter	Pore Vol	Pore Surf Area	Dv(d)	Ds(d)	Dv(logd)	Ds(logd)
Å	[cc/g]	[m²/g]	cc/ Å /g	[m²/Å/g]	[cc/g]	[m²/g]
13.7	8.51E-05	2.49E-01	2.90E-05	8.46E-02	9.10E-04	2.66E+00
16.36	2.21E-04	5.80E-01	5.66E-05	1.38E-01	2.13E-03	5.21E+00
18.78	3.76E-04	9.10E-01	6.32E-05	1.35E-01	2.73E-03	5.82E+00
21.27	5.75E-04	1.29E+00	7.91E-05	1.49E-01	3.87E-03	7.27E+00
23.88	6.94E-04	1.49E+00	4.41E-05	7.39E-02	2.42E-03	4.06E+00
26.71	8.86E-04	1.77E+00	6.50E-05	9.74E-02	4.00E-03	5.98E+00
29.89	1.15E-03	2.13E+00	7.84E-05	1.05E-01	5.39E-03	7.21E+00
33.39	1.68E-03	2.76E+00	1.46E-04	1.75E-01	1.12E-02	1.35E+01
37.7	5.10E-03	6.39E+00	6.81E-04	7.23E-01	5.91E-02	6.27E+01
42.6	6.54E-03	7.74E+00	3.01E-04	2.83E-01	2.95E-02	2.77E+01
48.21	7.42E-03	8.47E+00	1.36E-04	1.13E-01	1.51E-02	1.25E+01
55.53	8.48E-03	9.23E+00	1.30E-04	9.38E-02	1.66E-02	1.20E+01
65.13	9.67E-03	9.96E+00	1.07E-04	6.59E-02	1.60E-02	9.85E+00
77.76	1.08E-02	1.06E+01	8.27E-05	4.25E-02	1.48E-02	7.60E+00
95.64	1.22E-02	1.11E+01	6.28E-05	2.63E-02	1.38E-02	5.76E+00
119.65	1.38E-02	1.17E+01	6.16E-05	2.06E-02	1.69E-02	5.65E+00
173.61	1.61E-02	1.22E+01	2.73E-05	6.30E-03	1.07E-02	2.47E+00
281.86	1.76E-02	1.24E+01	1.17E-05	1.66E-03	7.44E-03	1.06E+00
1247.97	1.99E-02	1.25E+01	1.26E-06	4.02E-05	2.86E-03	9.17E-02

F.7 SAMPLE B; MONTH 2

Date: 05/20/2012

Quantachrome Corporation
Quantachrome Autosorb Automated Gas Sorption System Report
Autosorb for Windows® Version 1.19

Sample ID Abiola2B
Description AbiolaShale2B
Comments
Sample Weight 1.2000 g
Adsorbate NITROGEN Operator Abiola Cross-Sec Area 16.2 Å²/molec Outgas
Time 0.5 hrs Analysis Time 265.6 min NonIdeality 6.580E-05 P/Po Toler 5 End
of Run 05/18/2012 16:01 Molecular Wt 28.0134 g/mol Equil Time 2 File Name
EABI2B1.RAW Station # 1 Bath Temp. 77.35 °C

AREA-VOLUME-PORE SIZE SUMMARY

SURFACE AREA DATA

Multipoint BET..... 1.152E+01 m²/g
BJH Method Cumulative Desorption Surface Area..... 1.255E+01 m²/g
DH Method Cumulative Desorption Surface Area..... 1.267E+01 m²/g
DR Method Micro Pore Area..... 1.639E+01 m²/g

PORE VOLUME DATA

Total Pore Volume for pores with Diameter
less than 2988.2 Å at P/Po = 0.99355..... 2.187E-02 cc/g
BJH Method Cumulative Desorption Pore Volume..... 2.141E-02 cc/g
DH Method Cumulative Desorption Pore Volume..... 2.094E-02 cc/g
DR Method Micro Pore Volume..... 5.824E-03 cc/g
HK Method Cumulative Pore Volume..... 4.823E-03 cc/g
SF Method Cumulative Pore Volume..... 4.924E-03 cc/g

PORE SIZE DATA

Average Pore Diameter..... 7.597E+01 Å
BJH Method Desorption Pore Diameter (Mode)..... 3.829E+01 Å
DH Method Desorption Pore Diameter (Mode)..... 3.829E+01 Å
DR Method Micro Pore Width 1.065E+02 Å
DA Method Pore Diameter (Mode)..... 1.780E+01 Å
HK Method Pore Width (Mode)..... 1.502E+01 Å
SF Method Pore Diameter (Mode)..... 2.814E+01 Å

Table F.7: BET desorption pore size distribution for 2 month CO₂-brine flooded specimen of sample B

Diameter	Pore Vol	Pore Surf Area	Dv(d)	Ds(d)	Dv(logd)	Ds(logd)
Å	[cc/g]	[m²/g]	cc/ Å /g	[m²/Å/g]	[cc/g]	[m²/g]
13.8	1.45E-04	4.19E-01	5.00E-05	1.45E-01	1.58E-03	4.58E+00
16.44	2.44E-04	6.60E-01	4.17E-05	1.02E-01	1.58E-03	3.84E+00
18.85	3.70E-04	9.28E-01	5.14E-05	1.09E-01	2.23E-03	4.72E+00
21.35	5.48E-04	1.26E+00	7.03E-05	1.32E-01	3.45E-03	6.47E+00
23.97	7.31E-04	1.57E+00	6.78E-05	1.13E-01	3.74E-03	6.24E+00
26.81	9.42E-04	1.88E+00	7.05E-05	1.05E-01	4.35E-03	6.49E+00
30.1	1.23E-03	2.26E+00	7.91E-05	1.05E-01	5.47E-03	7.27E+00
34.07	1.84E-03	2.97E+00	1.40E-04	1.64E-01	1.10E-02	1.29E+01
38.29	5.45E-03	6.75E+00	8.87E-04	9.27E-01	7.82E-02	8.17E+01
42.76	6.59E-03	7.82E+00	2.36E-04	2.20E-01	2.32E-02	2.17E+01
48.43	7.37E-03	8.46E+00	1.20E-04	9.95E-02	1.34E-02	1.11E+01
55.86	8.28E-03	9.11E+00	1.08E-04	7.72E-02	1.38E-02	9.91E+00
65.57	9.30E-03	9.74E+00	9.31E-05	5.68E-02	1.40E-02	8.56E+00
78.47	1.05E-02	1.03E+01	7.99E-05	4.07E-02	1.44E-02	7.34E+00
95.04	1.17E-02	1.09E+01	6.60E-05	2.78E-02	1.44E-02	6.06E+00
122.82	1.39E-02	1.16E+01	5.87E-05	1.91E-02	1.65E-02	5.36E+00
176.77	1.66E-02	1.22E+01	3.83E-05	8.67E-03	1.54E-02	3.48E+00
314.91	1.91E-02	1.25E+01	1.23E-05	1.57E-03	8.62E-03	1.10E+00
1702.96	2.14E-02	1.26E+01	8.89E-07	2.09E-05	2.67E-03	6.28E-02

F.8 SAMPLE B; MONTH 3

Date: 06/20/2012

Quantachrome Corporation
Quantachrome Autosorb Automated Gas Sorption System Report
Autosorb for Windows® Version 1.19

Sample ID Shale2D
Description ReactedShale 2D
Comments
Sample Weight 1.3000 g
Adsorbate NITROGEN Operator Abiola Cross-Sec Area 16.2 Å²/molec Outgas
Time 0.5 hrs Analysis Time 321.2 min NonIdeality 6.580E-05 P/Po Toler 5 End
of Run 06/20/2012 07:14 Molecular Wt 28.0134 g/mol Equil Time 2 File Name
SHALETD.RAW Station # 1 Bath Temp. 77.35 °C

AREA-VOLUME-PORE SIZE SUMMARY

SURFACE AREA DATA

Multipoint BET..... 1.447E+01 m²/g
BJH Method Cumulative Desorption Surface Area..... 1.308E+01 m²/g
DH Method Cumulative Desorption Surface Area..... 1.327E+01 m²/g
DR Method Micro Pore Area..... 2.009E+01 m²/g

PORE VOLUME DATA

Total Pore Volume for pores with Diameter
less than 2557.4 Å at P/Po = 0.99245..... 2.741E-02 cc/g
BJH Method Cumulative Desorption Pore Volume..... 2.255E-02 cc/g
DH Method Cumulative Desorption Pore Volume..... 2.207E-02 cc/g
DR Method Micro Pore Volume..... 7.140E-03 cc/g
HK Method Cumulative Pore Volume..... 5.726E-03 cc/g
SF Method Cumulative Pore Volume..... 5.876E-03 cc/g

PORE SIZE DATA

Average Pore Diameter..... 7.576E+01 Å
BJH Method Desorption Pore Diameter (Mode)..... 3.793E+01 Å
DH Method Desorption Pore Diameter (Mode)..... 3.793E+01 Å
DR Method Micro Pore Width 1.151E+02 Å
DA Method Pore Diameter (Mode)..... 1.800E+01 Å
HK Method Pore Width (Mode)..... 1.548E+01 Å
SF Method Pore Diameter (Mode)..... 2.907E+01 Å

Table F.8: BET desorption pore size distribution for 3-month CO₂-brine flooded specimen of sample B

Diameter	Pore Vol	Pore Surf Area	Dv(d)	Ds(d)	Dv(logd)	Ds(logd)
Å	[cc/g]	[m²/g]	cc/ Å /g	[m²/Å/g]	[cc/g]	[m²/g]
14.14	2.17E-04	6.14E-01	7.89E-05	2.23E-01	2.56E-03	7.24E+00
16.58	3.96E-04	1.05E+00	8.41E-05	2.03E-01	3.21E-03	7.73E+00
18.86	6.69E-04	1.63E+00	1.12E-04	2.39E-01	4.88E-03	1.03E+01
21.35	9.30E-04	2.11E+00	1.03E-04	1.92E-01	5.03E-03	9.43E+00
23.96	1.19E-03	2.54E+00	9.54E-05	1.59E-01	5.26E-03	8.78E+00
26.79	1.46E-03	2.95E+00	9.25E-05	1.38E-01	5.70E-03	8.51E+00
29.99	1.69E-03	3.26E+00	6.66E-05	8.88E-02	4.59E-03	6.13E+00
33.66	2.20E-03	3.86E+00	1.31E-04	1.56E-01	1.02E-02	1.21E+01
37.93	5.55E-03	7.40E+00	7.16E-04	7.56E-01	6.25E-02	6.59E+01
42.7	6.73E-03	8.50E+00	2.42E-04	2.27E-01	2.38E-02	2.23E+01
48.29	7.52E-03	9.15E+00	1.24E-04	1.03E-01	1.38E-02	1.14E+01
55.68	8.27E-03	9.69E+00	8.91E-05	6.40E-02	1.14E-02	8.19E+00
65.43	9.26E-03	1.03E+01	9.02E-05	5.52E-02	1.36E-02	8.29E+00
77.96	1.04E-02	1.09E+01	8.15E-05	4.18E-02	1.46E-02	7.48E+00
93.38	1.15E-02	1.14E+01	6.45E-05	2.76E-02	1.38E-02	5.93E+00
122.56	1.35E-02	1.20E+01	4.80E-05	1.57E-02	1.34E-02	4.38E+00
181.36	1.63E-02	1.26E+01	3.70E-05	8.17E-03	1.52E-02	3.36E+00
306.66	1.91E-02	1.30E+01	1.61E-05	2.10E-03	1.11E-02	1.44E+00
1475.66	2.26E-02	1.31E+01	1.59E-06	4.30E-05	4.22E-03	1.15E-01

F.9 SAMPLE C; CONTROL

Date: 04/26/2012

Quantachrome Corporation
Quantachrome Autosorb Automated Gas Sorption System Report
Autosorb for Windows® Version 1.19

Sample ID Abiola3c
Description ShaleCon3
Comments
Sample Weight 0.9050 g
Adsorbate NITROGEN Operator Abiola Cross-Sec Area 16.2 Å²/molec Outgas
Time 0.5 hrs Analysis Time 244.2 min NonIdeality 6.580E-05 P/Po Toler 5 End
of Run 04/12/2012 14:02 Molecular Wt 28.0134 g/mol Equil Time 2 File Name
EABI3CI.RAW Station # 1 Bath Temp. 77.35

AREA-VOLUME-PORE SIZE SUMMARY

SURFACE AREA DATA

Multipoint BET..... 5.057E+00 m²/g
BJH Method Cumulative Desorption Surface Area..... 6.550E+00 m²/g
DH Method Cumulative Desorption Surface Area..... 6.648E+00 m²/g
DR Method Micro Pore Area..... 7.246E+00 m²/g

PORE VOLUME DATA

Total Pore Volume for pores with Diameter
less than 3064.9 Å at P/Po = 0.99371..... 1.043E-02 cc/g
BJH Method Cumulative Desorption Pore Volume..... 1.053E-02 cc/g
DH Method Cumulative Desorption Pore Volume..... 1.031E-02 cc/g
DR Method Micro Pore Volume..... 2.575E-03 cc/g
HK Method Cumulative Pore Volume..... 2.064E-03 cc/g
SF Method Cumulative Pore Volume..... 2.108E-03 cc/g

PORE SIZE DATA

Average Pore Diameter..... 8.247E+01 Å
BJH Method Desorption Pore Diameter (Mode)..... 3.799E+01 Å
DH Method Desorption Pore Diameter (Mode)..... 3.799E+01 Å
DR Method Micro Pore Width 1.181E+02 Å
DA Method Pore Diameter (Mode)..... 1.780E+01 Å
HK Method Pore Width (Mode)..... 1.523E+01 Å
SF Method Pore Diameter (Mode)..... 2.870E+01 Å

Table F.9: BET desorption pore size distribution for control specimen of sample C

Diameter	Pore Vol	Pore Surf Area	Dv(d)	Ds(d)	Dv(logd)	Ds(logd)
Å	[cc/g]	[m²/g]	cc/ Å /g	[m²/Å/g]	[cc/g]	[m²/g]
14.05	0.00E+00	0.00E+00	0.00E+00	0.00E+00	0.00E+00	0.00E+00
16.17	0.00E+00	0.00E+00	0.00E+00	0.00E+00	0.00E+00	0.00E+00
18.65	0.00E+00	0.00E+00	0.00E+00	0.00E+00	0.00E+00	0.00E+00
21.15	2.86E-05	5.42E-02	1.13E-05	2.14E-02	5.50E-04	1.04E+00
23.76	9.81E-05	1.71E-01	2.57E-05	4.33E-02	1.40E-03	2.36E+00
26.59	1.90E-04	3.09E-01	3.10E-05	4.67E-02	1.90E-03	2.86E+00
29.73	3.67E-04	5.47E-01	5.29E-05	7.12E-02	3.62E-03	4.87E+00
33.69	5.73E-04	7.92E-01	4.51E-05	5.36E-02	3.50E-03	4.15E+00
37.99	2.48E-03	2.80E+00	4.73E-04	4.98E-01	4.13E-02	4.35E+01
42.18	3.81E-03	4.06E+00	3.07E-04	2.91E-01	2.98E-02	2.83E+01
47.58	4.18E-03	4.37E+00	5.65E-05	4.75E-02	6.18E-03	5.19E+00
54.72	4.77E-03	4.81E+00	7.61E-05	5.56E-02	9.57E-03	7.00E+00
63.7	5.42E-03	5.21E+00	6.40E-05	4.02E-02	9.36E-03	5.88E+00
75.86	6.19E-03	5.62E+00	5.43E-05	2.86E-02	9.46E-03	4.99E+00
92.83	7.03E-03	5.98E+00	4.24E-05	1.83E-02	9.02E-03	3.89E+00
118.78	7.77E-03	6.23E+00	2.31E-05	7.76E-03	6.27E-03	2.11E+00
165.98	8.57E-03	6.42E+00	1.28E-05	3.09E-03	4.84E-03	1.17E+00
303.76	9.34E-03	6.52E+00	3.64E-06	4.79E-04	2.43E-03	3.21E-01
1737.67	1.05E-02	6.55E+00	4.46E-07	1.03E-05	1.36E-03	3.12E-02

F.10 SAMPLE C; MONTH 1

Date: 05/19/2012

Quantachrome Corporation
Quantachrome Autosorb Automated Gas Sorption System Report
Autosorb for Windows® Version 1.19

Sample ID Abiola3A
Description AbiolaShale3A
Comments
Sample Weight 1.4000 g
Adsorbate NITROGEN Operator Abiola Cross-Sec Area 16.2 Å²/molec Outgas
Time 0.5 hrs Analysis Time 243.2 min NonIdeality 6.580E-05 P/Po Toler 5 End
of Run 05/17/2012 21:03 Molecular Wt 28.0134 g/mol Equil Time 2 File Name
ABIOLATA.RAW Station # 1 Bath Temp. 77.35 °C

AREA-VOLUME-PORE SIZE SUMMARY

SURFACE AREA DATA

Multipoint BET..... 4.422E+00 m²/g
BJH Method Cumulative Desorption Surface Area..... 5.354E+00 m²/g
DH Method Cumulative Desorption Surface Area..... 5.401E+00 m²/g
DR Method Micro Pore Area..... 6.239E+00 m²/g

PORE VOLUME DATA

Total Pore Volume for pores with Diameter
less than 1993.6 Å at P/Po = 0.99028..... 1.016E-02 cc/g
BJH Method Cumulative Desorption Pore Volume..... 1.018E-02 cc/g
DH Method Cumulative Desorption Pore Volume..... 9.947E-03 cc/g
DR Method Micro Pore Volume..... 2.217E-03 cc/g
HK Method Cumulative Pore Volume..... 1.779E-03 cc/g
SF Method Cumulative Pore Volume..... 1.821E-03 cc/g

PORE SIZE DATA

Average Pore Diameter..... 9.187E+01 Å
BJH Method Desorption Pore Diameter (Mode)..... 3.812E+01 Å
DH Method Desorption Pore Diameter (Mode)..... 3.812E+01 Å
DR Method Micro Pore Width 1.154E+02 Å
DA Method Pore Diameter (Mode)..... 1.800E+01 Å
HK Method Pore Width (Mode)..... 1.562E+01 Å
SF Method Pore Diameter (Mode)..... 2.925E+01 Å

Table F.10: BET desorption pore size distribution for 1-month CO₂-brine flooded specimen of sample C

Diameter	Pore Vol	Pore Surf Area	Dv(d)	Ds(d)	Dv(logd)	Ds(logd)
Å	[cc/g]	[m²/g]	cc/ Å /g	[m²/Å/g]	[cc/g]	[m²/g]
14.08	0.00E+00	0.00E+00	0.00E+00	0.00E+00	0.00E+00	0.00E+00
16.21	1.20E-05	2.96E-02	4.80E-06	1.19E-02	1.79E-04	4.41E-01
18.68	5.22E-05	1.16E-01	1.65E-05	3.53E-02	7.07E-04	1.51E+00
21.16	8.35E-05	1.75E-01	1.25E-05	2.35E-02	6.06E-04	1.15E+00
23.77	9.58E-05	1.96E-01	4.54E-06	7.64E-03	2.48E-04	4.18E-01
26.59	1.64E-04	2.97E-01	2.31E-05	3.47E-02	1.41E-03	2.12E+00
29.8	2.63E-04	4.32E-01	2.87E-05	3.85E-02	1.97E-03	2.64E+00
33.95	5.63E-04	7.85E-01	6.23E-05	7.34E-02	4.86E-03	5.73E+00
38.12	2.15E-03	2.45E+00	4.51E-04	4.73E-01	3.95E-02	4.15E+01
42.22	2.88E-03	3.15E+00	1.56E-04	1.48E-01	1.52E-02	1.44E+01
47.72	3.24E-03	3.44E+00	5.56E-05	4.66E-02	6.10E-03	5.12E+00
54.85	3.66E-03	3.75E+00	5.30E-05	3.86E-02	6.68E-03	4.87E+00
64.03	4.15E-03	4.05E+00	4.71E-05	2.94E-02	6.93E-03	4.33E+00
76.3	4.73E-03	4.36E+00	4.12E-05	2.16E-02	7.21E-03	3.78E+00
94.49	5.32E-03	4.61E+00	2.66E-05	1.13E-02	5.77E-03	2.44E+00
123.01	6.14E-03	4.88E+00	2.35E-05	7.63E-03	6.60E-03	2.15E+00
165.75	7.00E-03	5.08E+00	1.71E-05	4.13E-03	6.47E-03	1.56E+00
286.43	8.54E-03	5.30E+00	8.07E-06	1.13E-03	5.12E-03	7.15E-01
1187.68	1.02E-02	5.35E+00	1.02E-06	3.42E-05	2.28E-03	7.67E-02

F.11 SAMPLE C; MONTH 2

Date: 05/20/2012

Quantachrome Corporation
Quantachrome Autosorb Automated Gas Sorption System Report
Autosorb for Windows® Version 1.19

Sample ID Abiola3B
Description AbiolaShale3B
Comments
Sample Weight 1.2000 g
Adsorbate NITROGEN Operator Abiola Cross-Sec Area 16.2 Å²/molec Outgas
Time 0.5 hrs Analysis Time 250.9 min NonIdeality 6.580E-05 P/Po Toler 5 End
of Run 05/18/2012 22:43 Molecular Wt 28.0134 g/mol Equil Time 2 File Name
ABIOLA3B.RAW Station # 1 Bath Temp. 77.35 °C

AREA-VOLUME-PORE SIZE SUMMARY

SURFACE AREA DATA

Multipoint BET..... 5.297E+00 m²/g
BJH Method Cumulative Desorption Surface Area..... 5.850E+00 m²/g
DH Method Cumulative Desorption Surface Area..... 5.906E+00 m²/g
DR Method Micro Pore Area..... 7.629E+00 m²/g

PORE VOLUME DATA

Total Pore Volume for pores with Diameter
less than 4000.9 Å at P/Po = 0.99519..... 1.228E-02 cc/g
BJH Method Cumulative Desorption Pore Volume..... 1.210E-02 cc/g
DH Method Cumulative Desorption Pore Volume..... 1.182E-02 cc/g
DR Method Micro Pore Volume..... 2.711E-03 cc/g
HK Method Cumulative Pore Volume..... 2.236E-03 cc/g
SF Method Cumulative Pore Volume..... 2.283E-03 cc/g

PORE SIZE DATA

Average Pore Diameter..... 9.276E+01 Å
BJH Method Desorption Pore Diameter (Mode)..... 3.804E+01 Å
DH Method Desorption Pore Diameter (Mode)..... 3.804E+01 Å
DR Method Micro Pore Width 1.093E+02 Å
DA Method Pore Diameter (Mode)..... 1.780E+01 Å
HK Method Pore Width (Mode)..... 1.552E+01 Å
SF Method Pore Diameter (Mode)..... 2.916E+01 Å

Table F.11: BET desorption pore size distribution for 2-month CO₂-brine flooded specimen of sample C

Diameter	Pore Vol	Pore Surf Area	Dv(d)	Ds(d)	Dv(logd)	Ds(logd)
Å	[cc/g]	[m²/g]	cc/ Å /g	[m²/Å/g]	[cc/g]	[m²/g]
13.44	5.49E-05	1.63E-01	1.82E-05	5.41E-02	5.60E-04	1.67E+00
16.2	5.87E-05	1.73E-01	1.51E-06	3.72E-03	5.61E-05	1.39E-01
18.67	1.18E-04	3.01E-01	2.44E-05	5.22E-02	1.05E-03	2.24E+00
21.16	1.77E-04	4.11E-01	2.31E-05	4.38E-02	1.13E-03	2.13E+00
23.75	2.49E-04	5.32E-01	2.70E-05	4.55E-02	1.48E-03	2.49E+00
26.57	2.77E-04	5.75E-01	9.52E-06	1.43E-02	5.82E-04	8.76E-01
29.76	3.70E-04	7.00E-01	2.75E-05	3.69E-02	1.88E-03	2.53E+00
33.79	6.67E-04	1.05E+00	6.35E-05	7.52E-02	4.93E-03	5.84E+00
38.04	2.31E-03	2.78E+00	4.31E-04	4.53E-01	3.77E-02	3.96E+01
42.17	3.25E-03	3.67E+00	2.11E-04	2.00E-01	2.04E-02	1.94E+01
47.49	3.52E-03	3.90E+00	4.39E-05	3.70E-02	4.79E-03	4.04E+00
54.51	3.86E-03	4.15E+00	4.39E-05	3.22E-02	5.50E-03	4.03E+00
63.6	4.29E-03	4.42E+00	4.15E-05	2.61E-02	6.06E-03	3.81E+00
76	4.82E-03	4.70E+00	3.65E-05	1.92E-02	6.36E-03	3.35E+00
94.13	5.50E-03	4.98E+00	3.10E-05	1.32E-02	6.68E-03	2.84E+00
123.83	6.39E-03	5.28E+00	2.39E-05	7.72E-03	6.76E-03	2.18E+00
173.81	7.48E-03	5.52E+00	1.74E-05	4.00E-03	6.88E-03	1.58E+00
319.16	9.74E-03	5.81E+00	9.92E-06	1.24E-03	6.97E-03	8.73E-01
2217.13	1.21E-02	5.85E+00	6.61E-07	1.19E-05	2.44E-03	4.41E-02

F.12 SAMPLE C; MONTH 3

Date: 06/19/2012

Quantachrome Corporation
Quantachrome Autosorb Automated Gas Sorption System Report
Autosorb for Windows® Version 1.19

Sample ID Shale3D
Description ReactedShale 3D
Comments
Sample Weight 1.3000 g
Adsorbate NITROGEN Operator Abiola Cross-Sec Area 16.2 Å²/molec Outgas
Time 0.5 hrs Analysis Time 269.0 min NonIdeality 6.580E-05 P/Po Toler 5 End
of Run 06/19/2012 09:08 Molecular Wt 28.0134 g/mol Equil Time 2 File Name
SHALE2D.RAW Station # 1 Bath Temp. 77.35 °C

AREA-VOLUME-PORE SIZE SUMMARY

SURFACE AREA DATA

Multipoint BET..... 7.608E+00 m²/g
BJH Method Cumulative Desorption Surface Area..... 6.655E+00 m²/g
DH Method Cumulative Desorption Surface Area..... 6.722E+00 m²/g
DR Method Micro Pore Area..... 1.035E+01 m²/g

PORE VOLUME DATA

Total Pore Volume for pores with Diameter
less than 1830.1 Å at P/Po = 0.98940..... 1.602E-02 cc/g
BJH Method Cumulative Desorption Pore Volume..... 1.332E-02 cc/g
DH Method Cumulative Desorption Pore Volume..... 1.302E-02 cc/g
DR Method Micro Pore Volume..... 3.677E-03 cc/g
HK Method Cumulative Pore Volume..... 2.780E-03 cc/g
SF Method Cumulative Pore Volume..... 2.867E-03 cc/g

PORE SIZE DATA

Average Pore Diameter..... 8.424E+01 Å
BJH Method Desorption Pore Diameter (Mode)..... 3.786E+01 Å
DH Method Desorption Pore Diameter (Mode)..... 3.786E+01 Å
DR Method Micro Pore Width 1.300E+02 Å
DA Method Pore Diameter (Mode)..... 1.840E+01 Å
HK Method Pore Width (Mode)..... 1.667E+01 Å
SF Method Pore Diameter (Mode)..... 3.137E+01 Å

Table F.12: BET desorption pore size distribution for 3-month CO₂-brine flooded specimen of sample C

Diameter	Pore Vol	Pore Surf Area	Dv(d)	Ds(d)	Dv(logd)	Ds(logd)
Å	[cc/g]	[m²/g]	cc/ Å /g	[m²/Å/g]	[cc/g]	[m²/g]
13.8	6.10E-05	1.77E-01	2.13E-05	6.18E-02	6.75E-04	1.96E+00
16.35	1.27E-04	3.39E-01	2.95E-05	7.22E-02	1.11E-03	2.71E+00
18.68	2.40E-04	5.81E-01	4.64E-05	9.94E-02	1.99E-03	4.27E+00
21.17	3.49E-04	7.86E-01	4.30E-05	8.13E-02	2.09E-03	3.96E+00
23.77	4.53E-04	9.62E-01	3.88E-05	6.53E-02	2.12E-03	3.57E+00
26.59	5.81E-04	1.15E+00	4.34E-05	6.53E-02	2.65E-03	3.99E+00
29.76	7.28E-04	1.35E+00	4.33E-05	5.82E-02	2.96E-03	3.98E+00
33.68	1.09E-03	1.78E+00	8.06E-05	9.57E-02	6.24E-03	7.41E+00
37.86	2.55E-03	3.32E+00	3.72E-04	3.93E-01	3.24E-02	3.43E+01
42.16	3.41E-03	4.14E+00	1.84E-04	1.75E-01	1.79E-02	1.70E+01
47.6	3.80E-03	4.47E+00	6.27E-05	5.27E-02	6.86E-03	5.77E+00
54.67	4.21E-03	4.77E+00	5.23E-05	3.83E-02	6.57E-03	4.81E+00
63.63	4.70E-03	5.08E+00	4.89E-05	3.08E-02	7.15E-03	4.50E+00
76.04	5.18E-03	5.33E+00	3.24E-05	1.70E-02	5.65E-03	2.97E+00
94.76	5.95E-03	5.65E+00	3.37E-05	1.42E-02	7.32E-03	3.09E+00
125.16	6.95E-03	5.97E+00	2.64E-05	8.42E-03	7.54E-03	2.41E+00
173.24	8.17E-03	6.25E+00	2.10E-05	4.85E-03	8.29E-03	1.92E+00
282.57	1.02E-02	6.54E+00	1.26E-05	1.78E-03	7.96E-03	1.13E+00
1096.49	1.33E-02	6.66E+00	2.14E-06	7.79E-05	4.46E-03	1.63E-01

APPENDIX G

CALCULATION OF PERMEABILITY RATIO AND DIMENSIONLESS NUMBERS

G.1 Calculation of Permeability Ratio

$$\frac{k_{i+1}}{k_i} = \left[\frac{\phi_{i+1}^3}{\phi_i^3} \right] \left[\frac{a_{vi}^2}{a_{vi+1}^2} \right]$$

Table G.1: Calculations of permeability ratio for shale caprock samples over 3 months of CO₂-brine flooding

	Area(m²/g)		
Month/Sample	A	B	C
0	7.992	11.557	6.375
1	8.671	12.883	5.354
2	9.346	13.283	6.171
3	9.381	13.525	6.53375
	Volume(cc/g)		
Month/Sample	A	B	C
0	0.0126	0.01886	0.01043
1	0.01529	0.02016	0.01016
2	0.01591	0.02187	0.01228
3	0.0162	0.02241	0.01302
	Permeability Ratio, $\frac{k_{i+1}}{k_i}$		
Month/Sample	A	B	C
0	1	1	1
1	1.518040642	0.982885	1.310484
2	1.472171143	1.180373	1.741773
3	1.542574283	1.224944	1.851891

G.2 Calculation of Dimensionless Numbers

$$Pe = \frac{vl}{D} \quad Da = \frac{l}{vT_a} \quad PeDa = \frac{l^2}{T_a D} = \frac{\gamma_r l}{D} \\ \gamma_r = \frac{l}{T_a} \quad v = q / A$$

Table G.2: Calculation of Peclet (Pe) and Peclet-Damkohler (PeDa) Numbers

Sample A				
Month	l(m)	v(m/s)	D(m²/s)	γ_r(m/s)
0	3.793E-09	0	3.95E-11	0.0008
1	3.822 E-09	2.18E-12	3.95E-11	0.0008
2	3.810 E-09	2.23E-12	3.95E-11	0.0008
3	3.816 E-09	2.41E-12	3.95E-11	0.0008
Sample B				
Month	l(m)	v(m/s)	D(m²/s)	γ_r(m/s)
0	3.767 E-09	0	3.95E-11	0.0008
1	3.770 E-09	1.46E-12	3.95E-11	0.0008
2	3.790 E-09	1.58E-12	3.95E-11	0.0008
3	3.793 E-09	1.72E-12	3.95E-11	0.0008
Sample C				
Month	l(m)	v(m/s)	D(m²/s)	γ_r(m/s)
0	3.799 E-09	0	3.95E-11	0.0008
1	3.812 E-09	3.52E-12	3.95E-11	0.0008
2	3.804 E-09	3.39E-12	3.95E-11	0.0008
3	3.810 E-09	3.54E-12	3.95E-11	0.0008
Pe				
Sample/Month	0	1	2	3
A	0	2.107E-10	2.158E-10	2.328E-10
B	0	0.140E-10	1.517E-10	1.655E-10
C	0	0.341E-10	3.264E-10	3.420E-10
PeDa				
Sample/Month	0	1	2	3
A	0	7.751E-02	7.726E-02	7.738E-02
B	0	7.645E-02	7.685E-02	7.692E-02
C	0	7.730E-02	7.714E-02	7.726E-02

VITA

Abiola Olabode is the third child of a family of three children. He attended Government College Ibadan and Command Day Secondary School Odogbo for his secondary education. He later proceeded to Obafemi Awolowo University Ile Ife where in 2008 he earned a Bachelor's degree in Chemical Engineering with honors. Abiola worked with Pan Ocean Oil Corporation in Lagos, Nigeria between 2008 and 2010 as a natural gas Process Engineer helping with the design of multi-stage NGL recovery systems. He has a co-authored paper published in the conference proceedings of the American Institute of Physics and was presented at the 4th International Conference on Porous Media and Its Applications held in Germany this past summer. Three other abstracts with Green House Gas Technology (GHGT), Association of Engineering Geologist (AEG) and the American Geophysical Union (AGU) have also been accepted for poster and oral presentations. He will be conferred with a Master of Science degree in Petroleum Engineering at the 2012 Fall commencement.